Intensity Noise Correlation in a Triply Resonant Optical Parametric Oscillator

by

Joseph Teja, Jr.

B.S., Electrical Engineering, Rutgers University (1995)

Submitted to the
Department of Electrical Engineering and Computer Science
in partial fulfillment of the requirements for the degree of

Master of Science in Electrical Engineering

at the

MASSACHUSETTS INSTITUTE OF TECHNOLOGY

May 1997

© Massachusetts Institute of Technology, MCMXCVII. All rights reserved.

Author_____
Department of Electrical Engineering and Computer Science
May 6, 1997

Certified by_____
Dr. N.C. Wong
Research Scientist, Research Laboratory of Electronics
Thesis Supervisor

Accepted by_____
Arthur C. Smith
Chairman, Departmental Committee on Graduate Students

MASSACHUSETTS INSTITUTE OF TECHNOLOGY

JUL 24 1997 Eng.

LIBRARIES

Intensity Noise Correlation in a Triply Resonant Optical Parametric Oscillator

by

Joseph Teja, Jr.

Submitted to the Department of Electrical Engineering and Computer Science
on May 8, 1997, in partial fulfillment of the
requirements for the degree of
Master of Science in Electrical Engineering

Abstract

A nearly degenerate optical parametric oscillator (OPO) represents a prototypic device for generating squeezed states of light and studying quantum noise. This research investigates the phenomenon of sub-shot noise fluctuations which result from the intensity correlation between continuous wave signal and idler beam outputs of an OPO. Broadband nonclassical intensity noise correlation is observed from the difference signal between these "twin" beams. A novel experimental approach using a type-II phase-matched triply-resonant OPO with a high pump cavity finesse is employed to demonstrate noise reduction below the shot noise limit, in excellent agreement with a rigorous theoretical model.

Thesis Supervisor: Dr. N.C. Wong
Title: Research Scientist, Research Laboratory of Electronics

Dedication

To **my Dad:**

Who always suggested strongly that *I could.* He is patient enough to allow me to discover myself, and accepts and embraces whatever I find. He attentively walks by my side and has always made me feel, above all, valuable.

...when children have learned through the love of their parents to feel valuable, it is almost impossible for the vicissitudes of adulthood to destroy their spirit.

-M. Scott Peck

Acknowledgements

I thank Dr. Franco Wong for the opportunity to work on a thesis topic which included a diversity of disciplines from which I could learn and grow. He allowed me to stumble and learn for myself from time to time, provided helpful and truly interesting insights when I needed them most, and ultimately trusted my eagerness, persistence and methodology in the endeavor to achieve rewarding results. This made the final months of experimental work truly enjoyable and invigorating. It has been a privilege to work with and learn from someone who has an impressive knowledge and enthusiasm for the field of nonlinear and quantum optics.

Professor Jeffrey Shapiro's daunting academic acumen has been an example and a model for scientific rigor, professionalism and excellence which I will never forget. He has offered helpful and level critique in all aspects of my academic experience at MIT, and has done so with genuine interest and effortless good nature.

Not enough could possibly be said about Reggie Brothers, a true companion and mentor in more than just the laboratory. Every thesis I have consulted from our research group over the last five years offers countless accolades and tributes to his friendship, humor, stimulating conversation, technical skill and knowledge, all of which are offered in abundance whenever and wherever needed. I am hard pressed to embellish. I can only add that it will indeed be my privilege and honor to continue nurturing our professional and personal friendship for many many years to come.

I would also like to thank the other members of the group, including Phil Nee, Jeff Bounds for his electronic help and electric wit, and Elliott Mason for, as he puts it, "struggling with me through the joys of quantum electronics", not to mention exposing me to some enjoyable music. My office mate Gilbert Leung deserves more

than honorable mention as well, providing me with several hours of great conversation and life-pondering.

James Hockenberry has been a wonderful comrade-in-arms since we first passed through the hallowed halls of MIT, and I know no one else who so succinctly shares my conviction for being a good teacher to others. He puts heart-warming conscientious effort and caring into teaching, and I have learned much from his general approach to "dealing with The Institute".

In spite of cold academics, MIT and its environs have brought me together with people who not only made my stay more human and warm and ethnic ($\smile$) , but whose role in my life will far transcend our experiences here. My real rewards at MIT have been the likes of Marco Skandera, Leonardo Rastelli, Federico Girosi and Dean Lampros, thanks in great part to the "Coffeehouse".

Were it not for the friendship of Diane Bradway, the grey or darker times would have been infinitely blacker. She has been my biggest fan and support net; she often reminds me of how proud she is of my achievements and that they are important, even if I do not always feel it. When I'm riding perhaps too high, she levels the playing field. She is simultaneously sobering objectivity and a one-woman pep rally; a true original that I simply cannot do without.

Finally, I am forever indebted to Dr. Hyun Yoon for believing in me. My personal effort aside, I owe any and all of my professional and academic successes and achievements to his faith. He has been far more than a mentor, for in addition to sharing with me his own insights and knowledge of humanity in general, he has afforded me the opportunity to enter doors to worlds which otherwise may have never been open to me.

Contents

List of Figures

List of Tables

Chapter 1
Introduction

As a direct result of the quantum nature of electromagnetic radiation, all forms of light exhibit inherent and unavoidable random fluctuations. These fluctuations are a source of noise that limits the accuracy with which information can be transmitted by a beam of light. This limit set by the quantum-statistical nature of light for a coherent light beam is referred to as *shot noise.*

It is possible to actually achieve sub-shot noise performance by a phenomenon known as *squeezing* of light. Squeezed light makes it possible to obtain a higher signal-to-noise ratio than from a coherent light source with the same power, and it can be applied to reduced-error lightwave communications, precision measurement based on optical interferometry and spectroscopy.

A variety of methods have been utilized to realize squeezed states of light, including four-wave mixing in atomic vapors [32] and in optical fibers [31], as well as above and below threshold optical parametric oscillators (OPOs) [2, 15, 29]. In the case of an OPO, an optical cavity is loaded with a nonlinear crystal, and parametric down conversion of an input pump beam is achieved by either type-I or type-II phase matching [23, 28]. The OPO is especially attractive for quantum noise studies because the nonlinear medium contributes negligible spontaneous emission noise [12]; available nonlinear crystals have good crystal quality and low losses and do not introduce appreciable excess noise. Additionally, OPOs provide an intense and narrowband non-classical radiation source, having both spatial and temporal coherence, analogous in many respects to a laser.

This thesis describes the use of a triply-resonant OPO, in which the pump

wave as well as the down-converted signal and idler waves are resonant with the optical cavity. This feature allows a low oscillation threshold for the OPO while maintaining a high output transmission of the down-converted beams, which is an important requirement for achieving a high degree of intensity correlation and hence substantial noise reduction below the shot noise limit.

In this introductory chapter, we overview the basic premises of the research. The nature of the fundamental shot noise limit of "classical" light sources is presented, followed by a discussion of the various natures of "non-classical" squeezed light. The operation of the OPO as a source of squeezed radiation is discussed, as well as a summary of previous work in this area. Finally, a motivation for the present work is offered with an outline of the thesis.

1.1 Shot Noise

Since the observation of quantum noise is made in the context of photodetector measurements, it is appropriate to begin by briefly reviewing the concept of noise in general, and the origin of shot noise in photodetection.

Noise represents random electromagnetic fields occupying the same spectral region as that occupied by some "signal". With regard to the measurement of optical power, noise causes fluctuations in the measurement, thus placing a lower limit on the smallest amount of power that can be measured. In most situations, the sources of noise are due to the concerted action of a large number of independent agents. In this case the central limit theorem of statistics [35] tells us that the noise is described by a Gaussian distribution with zero mean and a mean square variance σ^2. Time averaged noise power is proportional to this mean square value, or the statistical variance of random fluctuations. For a given observable quantity A, we will use the notation $\langle A \rangle$

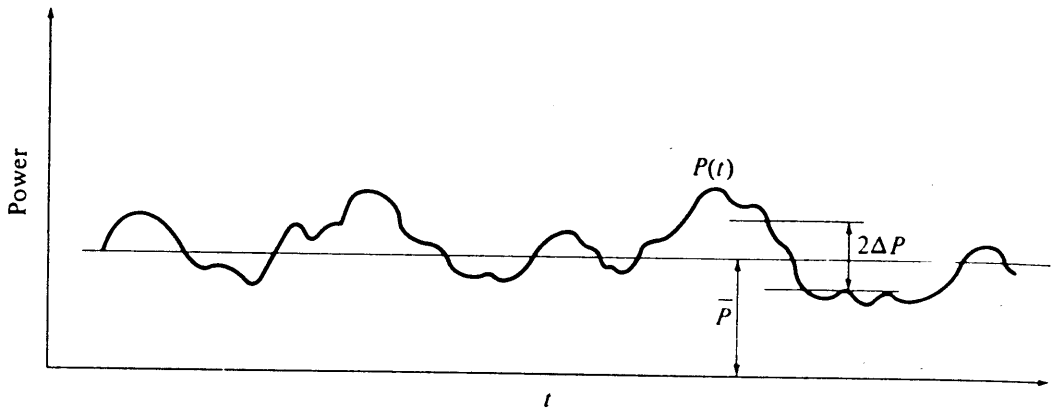

Figure 1.1: The intermingling of noise power with that of a signal causes the total power to fluctuate. The rms fluctuation ΔP limits the accuracy of power measurements. From [41].

to describe the mean of A, and the notation

$$\begin{aligned} \Delta A^2 &= \left\langle (A - \langle A \rangle)^2 \right\rangle \\ &= \langle A^2 \rangle - \langle A \rangle^2 \end{aligned}$$

to describe the variance of A.

The intermingling of noise power with that of a signal causes the total power to fluctuate (Fig. 1.1). This uncertainty resulting from the random nature of the noise limits the accuracy of power measurements. The limit of detectivity is commonly taken to be that at which the rms power fluctuation is comparable to the average signal power [41]. The task of optimizing detection is to therefore determine the main sources of noise power and discover ways to minimize them.

Photodetectors produce an electric current proportional to the incident radiation, or photon flux, via generation of carriers in a semiconductor. These detectors are characterized by a quantum efficiency which expresses the ratio of the rate of

electrons produced (photocurrent) to the rate of incident photons. The photocurrent due to an optical power P is

$$i = \eta e \frac{P}{\hbar\omega} \tag{1.1}$$

where $P/\hbar\omega$ is equal to the rate of photons incident on the detector, ω is the radian frequency of the radiation, e is the electron charge and η is the quantum efficiency, which is less than or equal to unity.

The output of a photodetector is generally contaminated by thermal (Johnson) noise, which represents noise power generated by thermally agitated charge carriers. Any electronic components which are used in the amplification and processing of the photodetector signal will contribute thermal noise, but as a practical matter this noise can be effectively minimized. However, even in the absence of thermal noise, one is still left with a photocurrent noise that can be traced to the quantum fluctuations of the light source. This quantum noise imposes a fundamental limit on the performance of any photodetection system.

There are both semi-classical and quantum mechanical approaches to the derivation of shot-noise. In the former, the radiation field is assumed to be classical, while the electrons in the photodetector are considered as quantized charge-carriers (Fig. 1.2). Noise arising in the photocurrent is attributed to the random emissions of mobile charge carriers. The individual electron emission events that occur at random times are modeled by a Poisson distribution function [22] which gives the probability of n events to occur in an observation period T. The Poisson distribution has the property of having equal mean and variance. The shot noise is calculated from the spectral density function of a train of randomly occurring electron emission events and the Fourier transform of a single current pulse between the two electrodes of the photodetector [41], and is typically given in terms of the mean square current

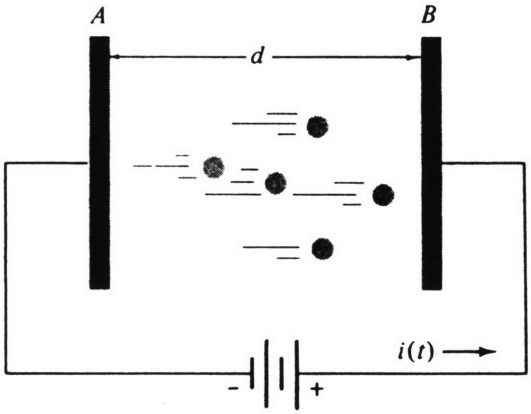

Figure 1.2: Random electron flow between two electrodes of a photodetector. This basic configuration is used in the derivation of shot noise. From [41].

amplitude, or variance, as a function of frequency

$$\overline{i_{SN}^2(f)} = \Delta i_{SN}^2 = 2eI_{DC}\Delta f, \tag{1.2}$$

where I_{DC} is the mean or DC photocurrent, and Δf is the bandwidth of the measurement device (for example, the resolution bandwidth of a spectrum analyzer). It is important to note that although the source of the shot noise appears as a DC current on the right side of Eq. (1.2), Δi_{SN}^2 represents an alternating current with frequencies near f, and is proportional (through some resistance value) to the shot noise power.

1.2 Quantum Origins of Shot Noise

The quantum mechanical approach to the derivation of shot noise using a quantized single mode electromagnetic field reveals more rigorously that indeed the statistical property of the laser field itself is responsible for the fluctuations of photocurrent [42, 26]. In this view, photon arrivals at the detector are regarded as a Poisson process

which subsequently generates electrons with a Poisson distribution. This differs from the classical viewpoint, where a classical light wave incident on the detector randomly generates photoelectrons.

Light is a quantum mechanical entity, and its proper description requires the quantization of the electromagnetic field. In a classical description, complete information about a single mode of the electromagnetic field can be obtained by simultaneously measuring a pair of variables, for example the amplitude E_o and phase ϕ of the electric (or magnetic) field, or equivalently its two quadrature amplitudes (A and B) (Fig. 1.3a), given by

$$\begin{aligned} E &= E_o \cos \omega t - \phi \\ &= A \cos \omega t + B \sin \omega t. \end{aligned} \tag{1.3}$$

Quantum mechanically, such measurement variables are referred to as *canonical conjugates*, and an uncertainty principle applies to any such pair of conjugate variables. One is no longer able to simultaneously measure this pair of variables exactly (Fig. 1.3b), and the uncertainty associated with the measurement of either variable can be quantified by computing its variance. The *uncertainty principle* then states that the product of these two variances has a lower bound [1].

Laser light belongs to a class of quantum states known as coherent states [26]. A coherent state is the quantum state that is the closest to a classical state. It behaves in the mean as a classical sinusoidal field, with the two conjugate variables of amplitude and phase or quadrature amplitudes having equal quantum mechanical uncertainties. Coherent states are also minimum uncertainty states. It has been shown [26] that the mean and variance for the number of energy quanta or photons in the single mode coherent state are equal quantities, which is a characteristic of the

[1] For two quantum operators, $\hat{A}$ and $\hat{B}$, with a commutator $[\hat{A}, \hat{B}] = i\hat{C}$, the uncertainty principle states that $\Delta\hat{A}^2 \Delta\hat{B}^2 \geq \frac{1}{4}|\langle\hat{C}\rangle|^2$. From [26].

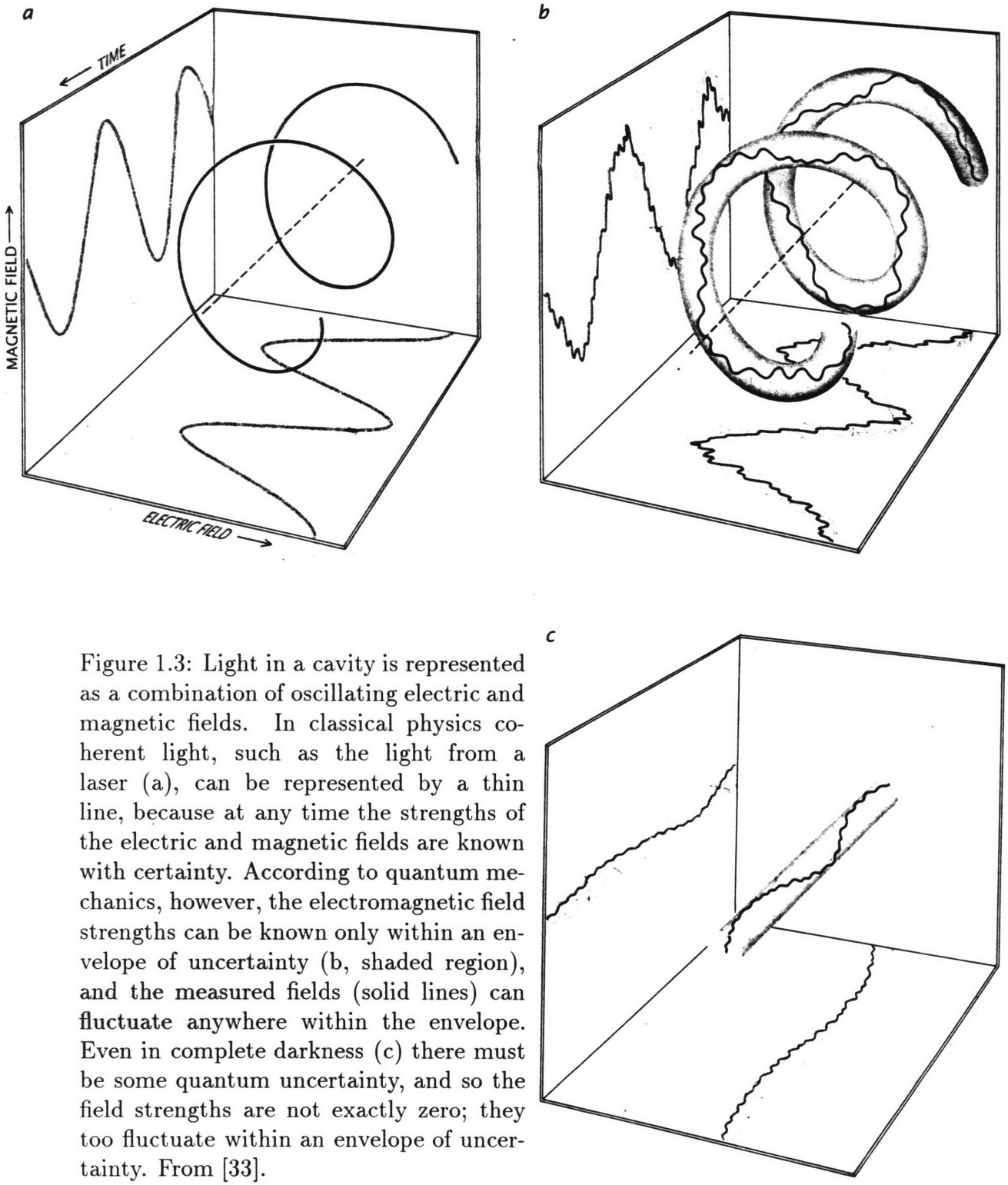

Figure 1.3: Light in a cavity is represented as a combination of oscillating electric and magnetic fields. In classical physics coherent light, such as the light from a laser (a), can be represented by a thin line, because at any time the strengths of the electric and magnetic fields are known with certainty. According to quantum mechanics, however, the electromagnetic field strengths can be known only within an envelope of uncertainty (b, shaded region), and the measured fields (solid lines) can fluctuate anywhere within the envelope. Even in complete darkness (c) there must be some quantum uncertainty, and so the field strengths are not exactly zero; they too fluctuate within an envelope of uncertainty. From [33].

Poisson distribution. The DC photocurrent generated by the laser light is then given by

$$I_{DC} = \eta e \frac{\langle n \rangle}{T} \tag{1.4}$$

where η is again the quantum efficiency, and e is the charge per electron generated by an expected number of photons $\langle n \rangle$ arriving in a time period T. For illustrative purposes, let us consider a perfect photodetector with efficiency $\eta = 1$. If the number of arriving photons fluctuates about the average $\langle n \rangle$, a fluctuating photocurrent results. The mean square fluctuation of the current is proportional to the variance Δn^2 in the Poisson photon arrivals (Fig. 1.4), and is given by

$$\begin{aligned} \Delta i^2 &= \left(\frac{e}{T}\right)^2 \Delta n^2 \\ &= \left(\frac{e}{T}\right)^2 \langle n \rangle \\ &= \left(\frac{e}{T}\right)^2 \frac{T}{e} I_{DC} \\ &= \left(\frac{e}{T}\right) I_{DC} \end{aligned} \tag{1.5}$$

where we have used Eq. (1.4) and the result that $\Delta n^2 = \langle n \rangle$. If we take a bandwidth based on the measurement time $T = \frac{1}{2\Delta f}$ (counting both negative and positive frequency contributions), we again arrive at the expression for shot noise given in Eq. (1.2). Hence, the quantum mechanical analysis reveals that the origin of the photocurrent noise from the detector is the radiation source itself.

1.3 Squeezed Light

As shown in the previous section, the electromagnetic field associated with a single mode of radiation may be described by two independent components: its magnitude and phase, or alternatively, its cosine and sine quadratures, as shown in Eq. (1.3). According to quantum mechanics, each of these measurable components inherently

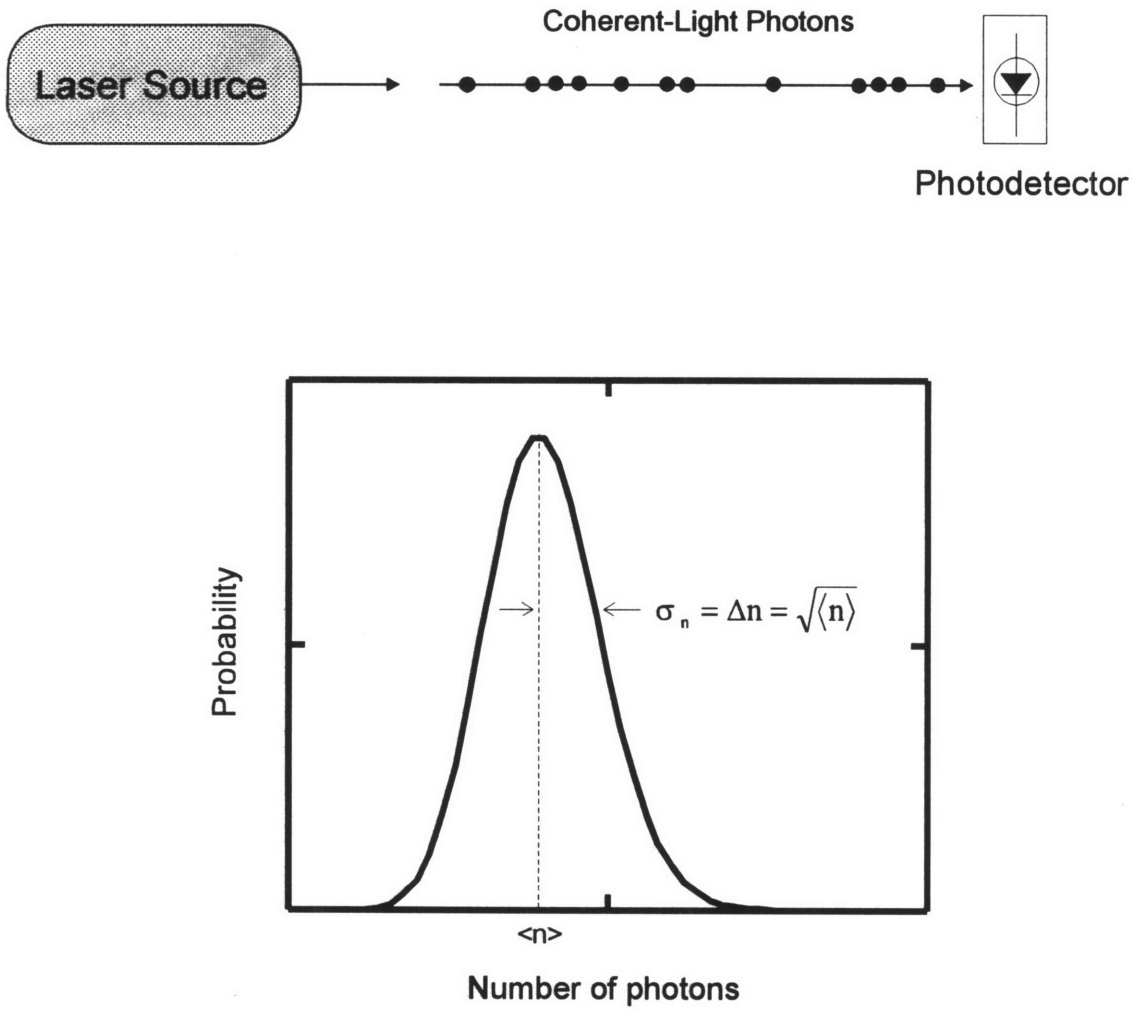

Figure 1.4: Whereas in the classical derivation of shot noise, random electron emissions from a constant intensity classical light source result in a Poisson distribution for the charge carriers, a more rigorous quantum mechanical approach to shot noise shows that the coherent light source itself consists of photons that impinge on a photodetector with a Poisson arrival process (mean = variance). From [36].

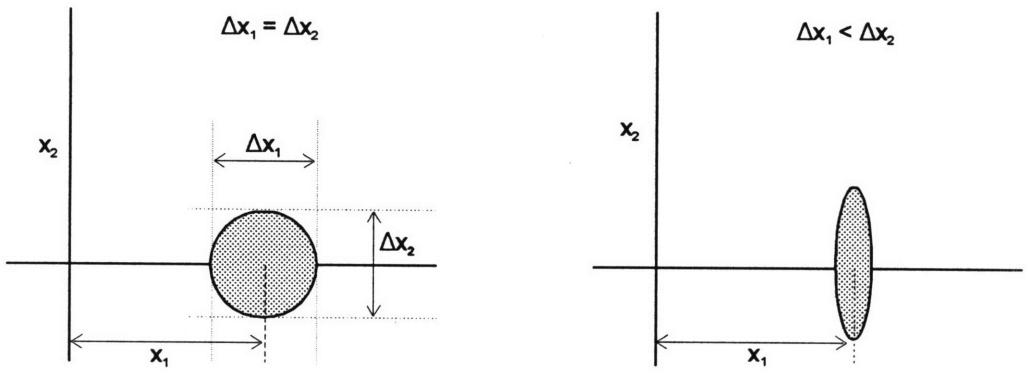

Figure 1.5: Squeezing may be visualized by considering two variables, x_1 and x_2, with equal variances, such that when plotted x_1 vs. x_2 the graph is circular. By reducing the variance of x_1 but increasing that of x_2, the plot becomes elliptical, giving the appearance that the original circle has been squeezed. From [42].

contain some uncertainty or "noise", and the product of these uncertainties obeys a fundamental lower bound. As a result, the two components cannot be simultaneously known with perfect precision, and the value of the electric or magnetic field cannot be totally certain.

However, the uncertainty of either of the measurable variables may in principle be reduced without limit, rendering it "noiseless". Of course, this reduction comes at the expense of an increase in the uncertainty of the other conjugate variable, so that the product of the two remains unchanged and the uncertainty principle is still satisfied. Unlike the coherent light described in the previous section, with a minimum uncertainty product and equal variances in the conjugate variables, light with a minimum uncertainty product but an unequal apportionment of fluctuations in the conjugate variables is said to be *squeezed* [36]. The nomenclature indicates that some of the fluctuations are "squeezed" out of one component and into the other (Fig. 1.5).

We may look at the phenomenon of squeezing fluctuations out of one variable and "dumping" them into another more fundamentally. Indeed, according to quantum mechanics there must be some amount of noise even in "darkness", when no other light is present. A classical wave representing darkness would be flat (it would not really be a wave at all); in quantum mechanics, on the other hand, one can say only that the wave is flat to within some small degree of uncertainty, and within the envelope of uncertainty the wave fluctuates randomly. This implies that even in a vacuum, with no external light sources, there must still be small fluctuations in the electromagnetic field; hence the terminology vacuum or zero-point fluctuations (Fig. 1.3c).

In a sense, it is really these zero-point fluctuations that underlie the noise of ordinary beams of light [33]. The wave representing a light beam can be seen as consisting of the irregular vacuum fluctuations superposed on the smooth wave described by classical physics. In this perspective, it is interference with the vacuum fluctuations that causes ordinary light waves to be noisy, and it is therefore the vacuum fluctuations which we describe as having variances governed by the uncertainty principle. Subsequently, we may think of squeezing noise out of the vacuum itself, with the somewhat peculiar result of a propagating wave that at some point contains less fluctuation than does an absolute vacuum. By making observations with a beam of squeezed light and a detector that looks only at the squeezed part of the light wave and not at the noisy part, one can make measurements with more precision than seems possible under the constraints of the uncertainty principle, i.e., the shot noise limit.

1.4 Generation of Squeezed Light

As alluded to above, the method of detection plays a paramount role in the observation of squeezed light. It is more concise to speak of generating light in such a way so

that once it is detected by some particular method, a substantial reduction in one of its quadrature amplitudes can be observed (with a corresponding increase in the conjugate variable amplitude).

With this subtlety in mind, squeezed radiation may be generally categorized as either *phase* squeezed or *amplitude* squeezed (Fig. 1.6). The former refers to a state in which the phase is known to a high degree of certainty while the amplitude undergoes large fluctuations. In the latter case, the opposite is true; the amplitude is known to high precision while the phase information has a greater uncertainty than in the coherent state.

1.4.1 Intensity Correlation and the OPO

Another method of achieving sub-shot noise performance takes advantage of the intensity correlation between "twin" light beams. The nonlinear χ^2 process of parametric down conversion (Ch. 2) is known to produce highly correlated twin photon beams [7]. This process involves the generation of two frequencies, a *signal* field at ω_s and an *idler* field at ω_i by a nonlinear crystal irradiated with a *pump* field at frequency ω_p. Parametric down conversion can be thought of simply as a source emitting photons in pairs, where the three fields must satisfy both energy and linear momentum conservation conditions

$$\omega_p = \omega_s + \omega_i \tag{1.6}$$

$$\mathbf{k_p} = \mathbf{k_s} + \mathbf{k_i} \tag{1.7}$$

where ω is the frequency and $\mathbf{k}$ is the wave vector. The linear momentum relationship (1.7) is also known as the phase matching condition, discussed further in Appendix B. If the parametric medium is inserted in an optical cavity resonant for both signal and idler frequencies, oscillation on a single pair of modes takes place and the device is referred to as a doubly-resonant Optical Parametric Oscillator (OPO) (Fig. 1.7).

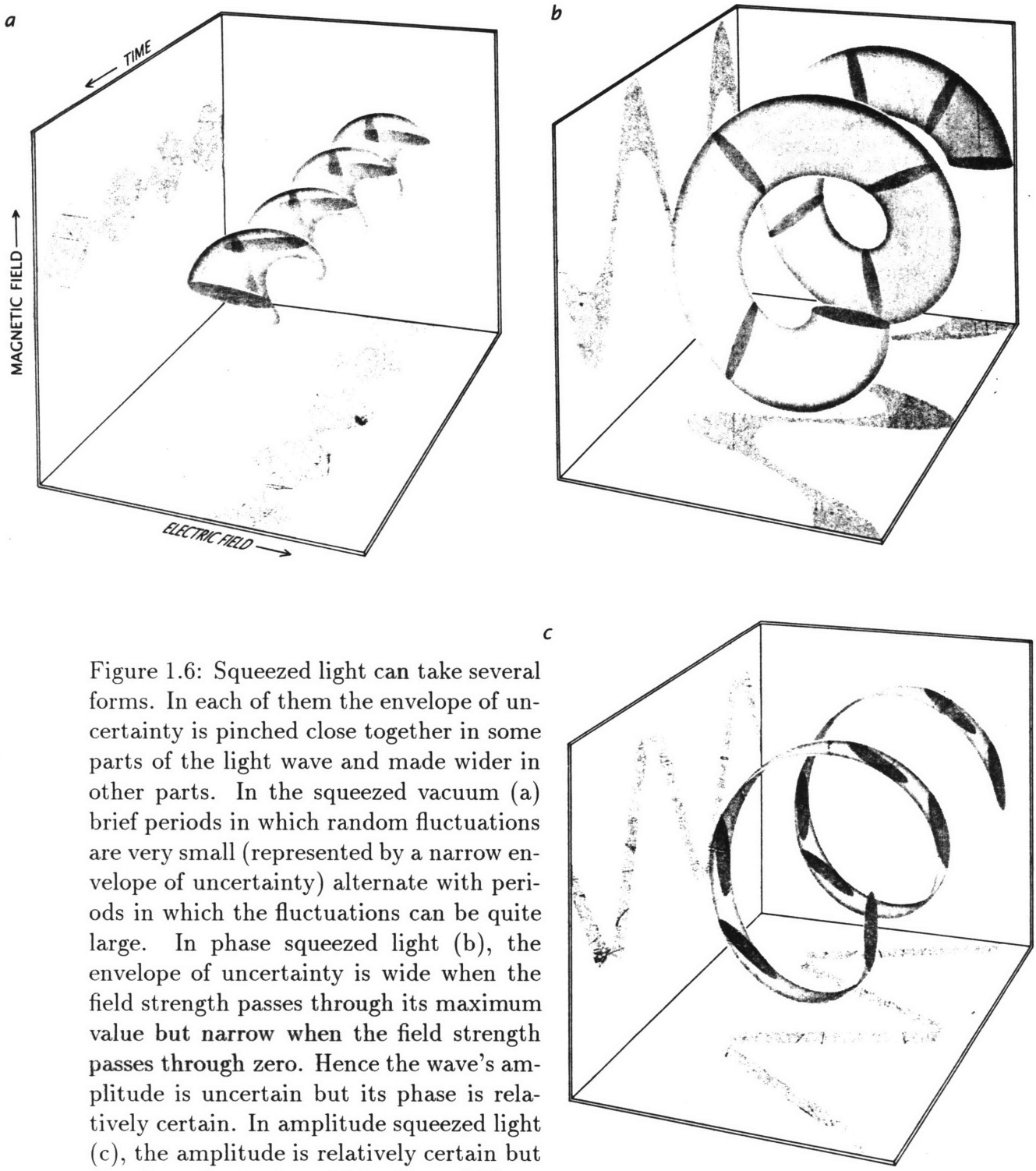

Figure 1.6: Squeezed light can take several forms. In each of them the envelope of uncertainty is pinched close together in some parts of the light wave and made wider in other parts. In the squeezed vacuum (a) brief periods in which random fluctuations are very small (represented by a narrow envelope of uncertainty) alternate with periods in which the fluctuations can be quite large. In phase squeezed light (b), the envelope of uncertainty is wide when the field strength passes through its maximum value but narrow when the field strength passes through zero. Hence the wave's amplitude is uncertain but its phase is relatively certain. In amplitude squeezed light (c), the amplitude is relatively certain but the phase fluctuates widely. From [33].

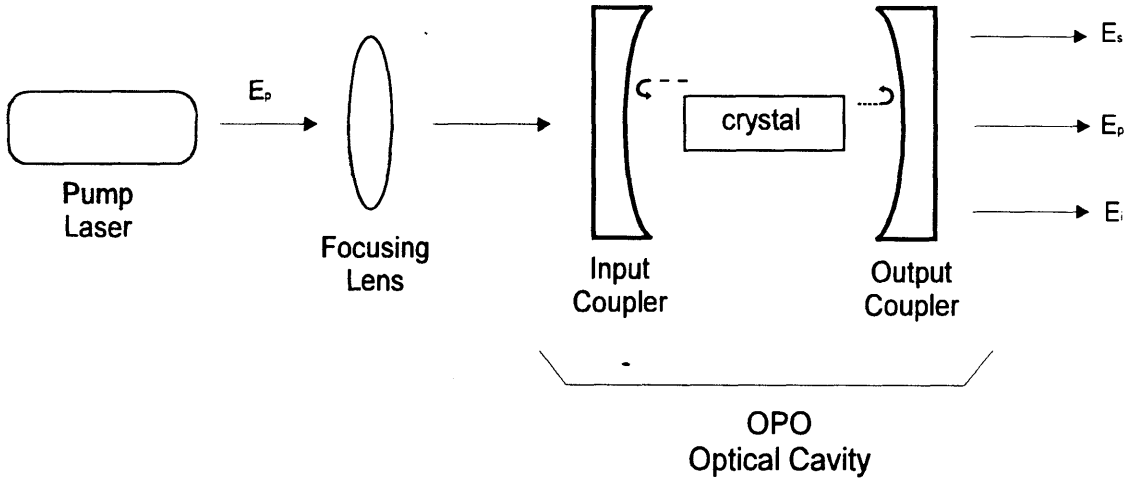

Figure 1.7: Schematic of an Optical Parametric Oscillator.

It has been theoretically shown [10] that an OPO operating above threshold produces two intense coherent twin beams having intensities correlated to better than the shot noise limit. This intensity correlation corresponds to a squeezing of the amplitude *difference* between the twin fields. The noise reduction on the intensity difference can be understood simply in terms of the photon pairs. In parametric down conversion, the nonlinear crystal emits pairs of simultaneous photons at frequencies ω_s and ω_i each time a pump photon is annihilated, generating twin beams which have exactly the same photon statistics; there is no noise on the intensity difference. In the OPO, the cavity placed around the crystal induces some decorrelation between the two beams as a result of loss mechanisms such as mirror transmission, absorption and scattering. These losses may be expressed in terms of a *cavity lifetime* for the photons given by

$$\tau_c = \frac{2l_{cav}}{c\kappa} \tag{1.8}$$

where l_{cav} is the cavity length, c is the speed of light in a vacuum, and κ is the total fractional loss for the signal or idler beams circulating in the cavity. Photons are

stored in the cavity for time τ_c and the number of photons delivered in the two beams outside of the cavity are expected to be nearly equal only when counted during a time long compared to this cavity lifetime . In the frequency domain, the noise on the intensity difference $I = I_s - I_i$ between the two beams is expected to be below the shot noise level for noise frequencies lower than the cavity bandwidth given by

$$\Delta f = \frac{1}{2\pi\tau_c}. \tag{1.9}$$

The action of correlation in the intensity difference between the signal and idler beams may alternatively be understood in terms of the statistics of random processes [22]. It has already been noted that each beam taken as a random process of photon arrivals obeys a Poisson distribution. If the processes of the two beams are uncorrelated, subtracting one process from the other results in the difference process with a variance (mean square fluctuations) equal to the sum of the individual processes; i.e. subtracting the uncorrelated beams results in *adding* the individual noise powers. If however the two processes are correlated as in the twin photon beam outputs of the OPO, the difference of the outputs results in *subtracting* the individual variances from each other. It is in this manner that the amplitude fluctuations of the difference is greatly reduced. Of course, this amplitude squeezing comes at the expense of a reduction in the certainty of the phase information, which is however of no consequence to the realization of noise levels below the shot noise limit.

1.5 Previous Work

One of the earliest demonstrations of squeezed states of the electromagnetic field generated by parametric down conversion in an OPO operating below threshold was by Wu, *et al* [40]. Employing a type-I phase matched magnesium oxide doped lithium niobate crystal in an OPO operating at degeneracy, noise reductions of 50% (-3 dB)

relative to the shot noise level were observed in a balanced homodyne detector.

A subsequent demonstration of twin-beam intensity correlation utilizing a type-II phase matched potassium titanyl phosphate (KTP) OPO was given by Heidman, *et al* [15]. Here, as a consequence of type-II phase matching, the twin beam outputs of the OPO were orthogonally polarized and were easily separated by a polarizing beam splitter. The photodetector currents from these beams were then differenced to obtain an intensity difference spectrum. In their earliest attempts, the noise power measured on the intensity difference between two such beams was reduced by a maximum of 30% (-1.5 dB) below the shot noise limit, and noise reduction was observed over a broad range of frequencies up to 20 MHz.

Continued efforts by this group (Mertz, *et al*) [27] to reduce the OPO cavity losses which tend to decrease the twin-beam intensity correlation resulted in a quantum noise reduction of 86% (-8.5 dB) near 3 MHz. An important point of this experiment was the use of a high transmission output coupling mirror in the OPO for the orthogonal twin-beam outputs ($T = 6.3\%$ as opposed to .8% in the earlier experiment). A simplified model of the measured intensity difference spectrum normalized to its associated shot noise level, which assumes identical losses for both signal and idler beams, is given by [15]

$$S_{ID}(f) = 1 - \left[\frac{\eta \left(1 - \frac{\mu}{T + \mu} \right)}{1 + \frac{f^2}{\Delta f^2}} \right] \tag{1.10}$$

where f is the noise frequency, Δf is the OPO cavity bandwidth, η is the photodiode quantum efficiency, T is the transmission of the cavity output coupling mirror and μ represents all other extraneous losses in the cavity (mirror absorption, crystal absorption and scattering, etc., Fig. 1.7). From Eq. (1.10), a high value of η and a low ratio of $\mu/(T + \mu)$ should minimize the noise spectrum. Therefore, improvements in the noise reduction require a high photodetector efficiency, low extraneous cavity

losses and a high output coupling.

However a high output coupling increases the oscillation threshold significantly. The threshold pumping power scales approximately as $(T + \mu)^2/F_p$, where F_p is the cavity pump finesse. To keep the threshold at a reasonable level, an increase in T should be accompanied by an increase in F_p, which can be accomplished with a double-pass or resonant-pump cavity configuration. The available pump power and the pump cavity design therefore place a limit on T and hence the maximum observable noise reduction. In the second experiment by Mertz, *et al*, a pump cavity finesse of $\sim$25 resulted in a pump threshold of 460 mW.

Experiments at the Research Laboratory of Electronics at Massachusetts Institute of Technology have investigated similar approaches. Leong [23, 24] followed more or less the approach of Wu, *et al* [40] using a type-I phase matched lithium niobate OPO. Because the OPO was operated above threshold, the co-polarized signal and idler output beams were separated using a Mach-Zehnder interferometer configuration. The maximum observed correlation yielded a noise level 50% (-3 dB) below the shot noise. The experiment showed good agreement with an improved theory for the intensity correlation that included the effect of pump excess noise and loss mismatches between the twin beam outputs [39].

In a recent experiment by Patterson [28], the approach of Mertz, *et al* was followed. The available pump power after intensity stabilization of the pump laser however was limited to $\sim$400 mW. The cavity designs investigated were of a double pass pump configuration (a relatively low cavity pump finesse) which consequently limited the output coupling transmission T. In addition, monolithic, two-piece and three-piece cavity constructions were investigated with regard to continuous wave output stability of the OPO. An output coupler of $T = .75\%$ was ultimately employed in a two piece cavity design which resulted in an OPO threshold of $\sim$30 mW. The maximum observed correlation was 38% at 3 MHz, resulting in a noise level 2.1 dB below shot noise.

1.6 Thesis Motivation and Organization

The research proposed was to design a high quality OPO that had a low pump threshold and a high twin-beam output correlation. The novel approach to the OPO design that facilitated these results relied on a four-piece three-mirror triply-resonant OPO with a substantial pump cavity finesse, F_p. The goal was to achieve a broadband intensity noise correlation spectrum up to ~10 MHz, with a maximum noise reduction that approached and/or exceeded the benchmark set by Mertz, *et al* [27]. The development of such a twin beam generator would allow the study of a wide variety of quantum noise phenomena, such as an injection-seeded optical parametric amplifier (OPA) operating in the saturated gain regime [38].

Quantum noise reduction over a broad frequency range opens the way to ultrasensitive optical measurements with significant improvements in the signal to noise ratios. Measurements of very small effects which break the balance between the intensities of the quantum correlated beams, such as modulation of one of the beams for optical communications [30], linear absorption [3] and scattering and polarization rotations [34] can be performed with a higher sensitivity by monitoring the intensity difference signal. An additional motivation was given by applications based on precision optical absorption spectroscopy [39].

The thesis is organized as follows: Chapter 2 and associated appendices provide a review of the useful theoretical concepts relevant to the experiment, including the nonlinear wave equation, difference frequency generation (parametric down-conversion), the Fabry-Perot resonator, Gaussian optics and mode matching, the OPO oscillation threshold, intensity correlation models and servo control basics used for the pump laser intensity and frequency stabilization as well as OPO cavity length stabilization. Chapter 3 gives a detailed description of the pump laser system, including the methodologies used for intensity and frequency stabilization as well as a characterization of the excess pump intensity noise spectrum. Chapter 4 outlines

the OPO cavity design and characterization, including the triply-resonant system. Chapter 5 describes the intensity correlation experiment, including the cavity stabilization techniques, and compares the experimental results to theoretical predictions. The concluding chapter summarizes the thesis contents and presents suggestions for future work.

Chapter 2

Theory

2.1 Introduction

In this chapter, the useful theoretical concepts relevant to the experiment are presented. Many of the discussions will be either of an "orientational" or review nature, and the reader is encouraged to consult the references for thorough treatments of the material, in particular [17] and [14] regarding optics and nonlinear interactions. In addition, some fundamental derivations are included as appendices.

In Appendix A, the classical nonlinear wave equation is derived in terms of a general nonlinear polarization for nonmagnetic media. This serves as a starting point here for reviewing the fundamental aspects of three-wave mixing processes, in particular parametric amplification or "down-conversion". Related topics of interest, including phase matching and the effective nonlinear constant d_{eff} are described in Appendix B and further in Sec. 4.3.1 as they particularly relate to the nonlinear medium used in the experiment. Following in this chapter, the Manley-Rowe relations are derived, which are a set of energy conservation equations which couple the wave viewpoint to the photon viewpoint.

Next, the basics of the Fabry-Perot interferometer and Gaussian optics are reviewed (Appendix D additionally gives a brief overview of mode matching for Gaussian beams which is used throughout the experiment) and applied to an optical parametric oscillator (OPO), which is the twin-beam generation device employed in the experiment. The OPO is essentially a parametric amplifier placed within a Fabry-Perot resonator. The single-pass pump oscillation threshold for the OPO is

first derived using reasonable simplifications for illustrative purposes, followed by the results of a more detailed analysis. This result is later applied in Sec. 4.5 to estimate the threshold of the device used for the experiment.

Models of the intensity correlation spectrum for the twin-beam outputs of the OPO are presented, beginning with a simplified conceptual view which is again applied in Sec. 4.5 to arrive at a reasonable and intuitive estimate based on the OPO design for this experiment. A more rigorous model is then described which is used in Sec. 5.7 to evaluate the experimental results. Appendix F contains a computer program which implements this more detailed intensity correlation model.

Finally, concepts of servo control are presented, which are used extensively in the various stabilization techniques employed throughout the experiment. While this includes descriptions of the electronic building blocks used in servo signal conditioning circuit design, the reader is again encouraged to consult the references for a thorough treatment of the material herein. An excellent tutorial of the relevant concepts in laser related servo control systems is given in [13].

2.2 Parametric Down-conversion

In Appendix A we developed a nonlinear wave equation (A.16) for a propagating field that was driven by a nonlinear polarization P_{NL}

$$\left(\frac{\partial}{\partial z}+\frac{n}{c}\frac{\partial}{\partial t}\right)E+\alpha E=-j\frac{\omega\mu_o c}{2n}(\hat{\mathbf{e}}\cdot\hat{\mathbf{p}})\;P_{NL}e^{j(\Delta kz)}. \tag{2.1}$$

The nonlinear polarization was the result of an interaction between two or more strong fields present in a material. Hence, the nonlinear polarization couples several fields which may be present in a material and can yield a variety of nonlinear processes.

In general, there will be a nonlinear polarization for *each* of the frequencies present in a material, which results in a system of coupled differential equations of

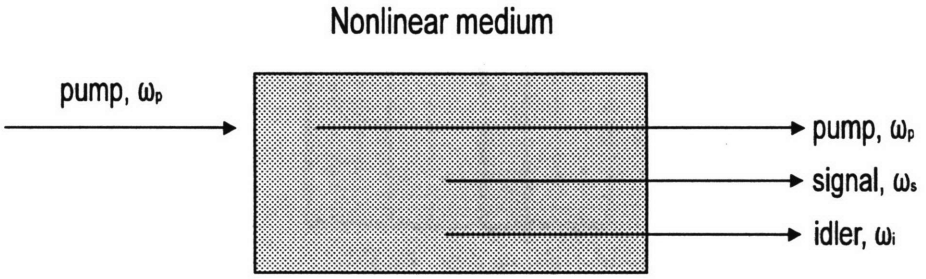

Figure 2.1: An optical parametric amplifier used for frequency down-conversion.

the form of Eq. (2.1). All nonlinear processes require energy and momentum conservation. For this experiment we are interested in the three wave mixing process of parametric down-conversion. This is a second order nonlinear process which involves the generation of two frequencies, a *signal* field at ω_s and an *idler* field at ω_i by a nonlinear crystal irradiated with a *pump* field at ω_p, where as required by energy and momentum conservation

$$\begin{aligned} \omega_p &= \omega_s + \omega_i \\ \mathbf{k_p} &= \mathbf{k_s} + \mathbf{k_i}, \end{aligned} \tag{2.2}$$

where the $\mathbf{k}$'s are the wave vectors. The linear momentum relationship (2.2) is also known as the phase matching condition, discussed further in Appendix B. Fig. 2.1 shows an optical parametric amplifier used for down-conversion.

In Appendix B, we further explored the origin of the nonlinear polarization in terms of an effective nonlinear coefficient d_{eff}, which essentially reduced the tensorial relationships between fields, nonlinear susceptibilities and polarizations to a scalar

relationship based on the field and crystal geometries, given by

$$\begin{aligned} P_{NL}(\omega_p) &= 2\epsilon_o d_{eff} E(\omega_s) E(\omega_i) e^{j\Delta kz} \\ P_{NL}(\omega_s) &= 2\epsilon_o d_{eff} E(\omega_p) E^*(\omega_i) e^{-j\Delta kz} \\ P_{NL}(\omega_i) &= 2\epsilon_o d_{eff} E(\omega_p) E^*(\omega_s) e^{-j\Delta kz} \end{aligned} \tag{2.3}$$

where $\Delta k = k_p - k_s - k_i$ and the d_{eff}'s are equal in each of the three equations describing the interaction as required by energy conservation. If we now substitute Eqs. (2.3) into Eq. (2.1), and ignore the time derivative for a steady state solution, we arrive at a set of coupled differential equations describing the three wave mixing parametric process

$$\frac{\partial}{\partial z} E(\omega_s) + \alpha_s E(\omega_s) = -j \frac{\omega_s d_{eff}}{n_s c} E(\omega_p) E^*(\omega_i) e^{-j\Delta kz} \tag{2.4}$$

$$\frac{\partial}{\partial z} E(\omega_i) + \alpha_i E(\omega_i) = -j \frac{\omega_i d_{eff}}{n_i c} E(\omega_p) E^*(\omega_s) e^{-j\Delta kz} \tag{2.5}$$

$$\frac{\partial}{\partial z} E(\omega_p) + \alpha_p E(\omega_p) = -j \frac{\omega_p d_{eff}}{n_p c} E(\omega_s) E(\omega_i) e^{j\Delta kz} \tag{2.6}$$

where the α's represent the single pass loss (per unit distance, 1/m) through the material for the respective fields.

2.3 The Manley-Rowe Relations

The Manley-Rowe relations couple the classical wave view of nonlinear interactions to the quantum mechanical photon viewpoint. This paradigm is particularly useful for interpreting the "twin" beam characteristic and intensity correlation of the signal and idler beam outputs from parametric down-conversion, as discussed in Sec. 1.4.1.

We begin by assuming phase matched conditions, i.e. $\Delta k = 0$, neglect material

losses ($\alpha = 0$) and we define the quantity

$$K_j = \frac{\omega_j d_{eff}}{n_j c}. \tag{2.7}$$

Multiplying the complex conjugate of Eq. (2.6) by $E(\omega_p)$ and substituting Eq. (2.7) yields

$$E(\omega_p)\frac{\partial E^*(\omega_p)}{\partial z} = jK_p^* E^*(\omega_s)E^*(\omega_i)E(\omega_p). \tag{2.8}$$

Taking the complex conjugate again yields

$$E^*(\omega_p)\frac{\partial E(\omega_p)}{\partial z} = -jK_p E(\omega_s)E(\omega_i)E^*(\omega_p). \tag{2.9}$$

We are interested in an expression that relates the change in beam power with propagation through the nonlinear medium. Starting with

$$\frac{\partial |E(\omega_p)|^2}{\partial z} = \frac{\partial}{\partial z}[E(\omega_p)E^*(\omega_p)] = E(\omega_p)\frac{\partial E^*(\omega_p)}{\partial z} + E^*(\omega_p)\frac{\partial E(\omega_p)}{\partial z} \tag{2.10}$$

and applying Eqs. (2.8) and (2.9) gives

$$\frac{\partial |E(\omega_p)|^2}{\partial z} = jK_p^* E^*(\omega_s)E^*(\omega_i)E(\omega_p) + \text{complex conjugate}, \tag{2.11}$$

and similarly for the signal and idler waves

$$\frac{\partial |E(\omega_s)|^2}{\partial z} = jK_s^* E(\omega_s)E(\omega_i)E^*(\omega_p) + \text{complex conjugate} \tag{2.12}$$

$$\frac{\partial |E(\omega_i)|^2}{\partial z} = jK_i^* E(\omega_s)E(\omega_i)E^*(\omega_p) + \text{complex conjugate}. \tag{2.13}$$

The intensity of a wave (in W/m^2) is given by

$$I(\omega) = \frac{1}{2} n_\omega \epsilon_\circ c \, |E(\omega)|^2 \tag{2.14}$$

and is proportional to the power through the effective area of the radiation. We may then write the change in intensity with propagation for the pump beam, using Eq. (2.11), as

$$\frac{\partial I(\omega_p)}{\partial z} = \frac{1}{2} n_p \epsilon_o c \frac{\partial |E(\omega_p)|^2}{\partial z}$$

$$= \frac{1}{2} \omega_p \epsilon_o [j d^*_{eff} E(\omega_p) E^*(\omega_s) E^*(\omega_i) + \text{complex conjugate }] \quad (2.15)$$

where we have used the substitution of Eq. (2.7). Similarly, using Eqs. (2.12) and (2.13) for the signal and idler intensities

$$\frac{\partial I(\omega_s)}{\partial z} = \frac{1}{2} \omega_s \epsilon_o [-j d_{eff} E(\omega_p) E^*(\omega_s) E^*(\omega_i) + \text{complex conjugate }] \quad (2.16)$$

$$\frac{\partial I(\omega_i)}{\partial z} = \frac{1}{2} \omega_i \epsilon_o [-j d_{eff} E(\omega_p) E^*(\omega_s) E^*(\omega_i) + \text{complex conjugate }]. \quad (2.17)$$

In a lossless material, $d_{eff} = d^*_{eff}$. If we now divide Eq. (2.15) by $\hbar\omega_p$, Eq. (2.16) by $\hbar\omega_s$ and Eq. (2.17) by $\hbar\omega_i$ and multiply the respective intensities by the effective radiation areas, we have

$$-\frac{1}{\hbar\omega_p} \frac{\partial P(\omega_p)}{\partial z} = \frac{1}{\hbar\omega_s} \frac{\partial P(\omega_s)}{\partial z} = \frac{1}{\hbar\omega_i} \frac{\partial P(\omega_i)}{\partial z} \quad (2.18)$$

where P is the beam power and $P/\hbar\omega$ is a photon rate. Eq. (2.18) is a conservation of energy equation called the Manley-Rowe relations. It states that for each photon destroyed at ω_p, one photon must be created at ω_s and one at ω_i. Hence, parametric down-conversion can be viewed as a process that emits pairs of simultaneous signal and idler photons each time a pump photon is annihilated.

2.4 The Fabry-Perot Interferometer

In Secs. 2.2 and 2.3 we have shown that a pump wave can cause a simultaneous amplification in a nonlinear medium of a signal and idler wave. If the nonlinear medium is placed within an optical resonator that provides resonances for the signal and idler waves, the parametric gain will, at some threshold pumping intensity, cause a simultaneous oscillation at the signal and idler frequencies. The threshold pumping corresponds to the point at which the parametric gain just balances the resonator cavity losses of the signal and idler waves. This is the physical basis of the optical parametric oscillator. Its practical importance derives from its ability to convert the power output of the pump laser to power at the signal and idler frequencies.

In this section, we review the basics of the Fabry-Perot interferometer, which serves as the resonator structure for the OPO. The terminology developed here will be useful throughout the experiment to describe various parameters and characteristics of the OPO and optical resonator systems in general.

The Fabry-Perot interferometer has many applications, including narrowband transmission filters, resonator structures for lasers and optical spectrum analyzers. Two parallel partially transmitting mirrors separated by a distance l_{cav} form the Fabry-Perot interferometer (Fig. 2.2). The distance l_{cav} is in general large compared with the wavelength.

From first principles, we may express the electric field portion of a wave travelling in the positive z-direction as Ee^{jkz}, where $k = 2\pi/\lambda$ is the propagation constant, and kz indicates the phase of the wave. This implies that for $z = \lambda$, the wave undergoes a phase change of 2π, or essentially, the wave is "back in phase". For a particular wavelength λ, if the interferometer cavity length $l_{cav} = n\frac{\lambda}{2}$, constructive interference occurs and the cavity is said to be *on resonance* at λ.

The important property of the Fabry-Perot interferometer is its power transmission or reflection dependence on cavity length and/or wavelength. For mirror

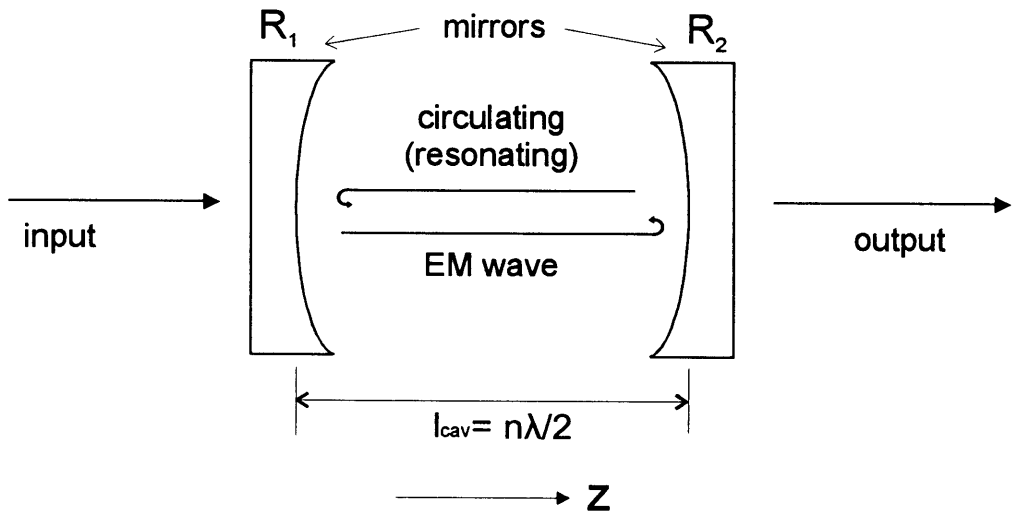

Figure 2.2: The Fabry-Perot interferometer.

reflectivities R_1 and R_2, the ratio of transmitted to input power is given by [14]

$$\left|\frac{E_{out}}{E_{in}}\right|^2 = \frac{(1-R_1)(1-R_2)}{(1-\sqrt{R_1R_2})^2 + 4\sqrt{R_1R_2}\sin^2\left[(\frac{2n\pi}{\lambda})l_{cav}\right]} \,. \tag{2.19}$$

From energy conservation, the ratio of reflected to input power is 1 minus the quantity given in Eq. (2.19). Fig. 2.3 shows plots of Eq. (2.19), where for simplicity the mirror reflectivities have been assumed to be identical, $R = R_1 = R_2$. The transmission curves have a characteristic Lorentzian lineshape.

Fig. 2.4 shows the detail of a transmission curve, which we will use to define some common terminology useful for describing characteristics of the resonator. The *free spectral range* (FSR) defines the "distance" (in terms of length or frequency) between successive transmission peaks, given by

$$\begin{aligned} FSR &= \frac{\lambda}{2} \text{ meters, or} \\ &= \frac{c}{2l_{cav}} \text{ Hz} \end{aligned} \tag{2.20}$$

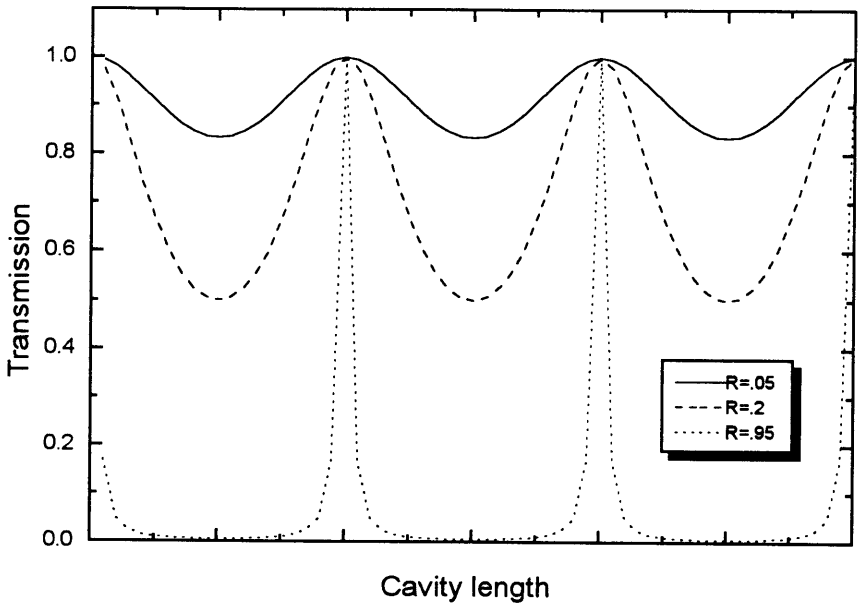

Figure 2.3: Transmission of a lossless Fabry-Perot interferometer.

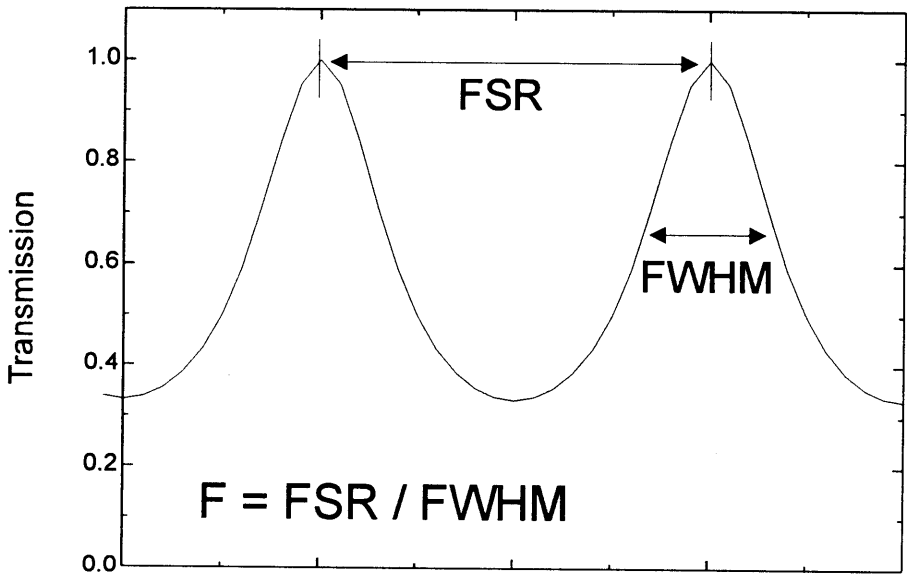

Figure 2.4: Detail of Fabry-Perot transmission for definition of common terminology.

where c is the speed of light in vacuum.

The *full width at half max* (FWHM) defines the cavity transmission bandwidth, or "linewidth". This can be obtained from Eq. (2.19) approximately, when $1 - R \ll 1$, as

$$FWHM = \frac{(1 - R)\, c}{2\pi\sqrt{R}\, l_{cav}}. \tag{2.21}$$

This width is a function of the total "losses" in the cavity, due to mirror transmission T ($R = 1 - T$). As will be seen in Ch. 4, other potential sources of loss in the cavity come from the parametric medium placed in the resonator to construct the OPO.

Finally, the *finesse* (F) of the cavity is defined as

$$F \equiv \frac{FSR}{FWHM} = \frac{\pi\sqrt{R}}{1 - R} \tag{2.22}$$

where we have shown the formula for the simplified case above. The finesse is a convenient dimensionless measure of relative linewidths of cavities; high finesse implies sharp peaks and thin linewidths. By virtue of the FWHM in the denominator, finesse is also a direct function of cavity losses, and can be approximated by [28]

$$F \approx \frac{2\pi}{\text{total round trip losses}} \tag{2.23}$$

where the total losses can include the cavity end-mirrors plus any absorption and scattering resulting from a material loaded in the cavity, such as the nonlinear medium used for parametric amplification.

2.5 Gaussian Beams

While up to this point we have only considered plane waves as a solution to the nonlinear wave equation, they are not the only possible solution. Another very interesting solution is the family of Hermite-Gaussian beams. When constructing interferometers

and resonators, one is interested in the modes and resonant frequencies of these structures. The Hermite-Gaussian beam solutions of the wave equation are well suited for this purpose and in fact represent the field profile characteristic of laser light [1].

While the Hermite-Gaussian family is an infinite orthogonal set of functions, we consider here only the "lowest order" member as a profile for an electric field

$$E(r,z) = E_\circ \frac{w_\circ}{w(z)} e^{-j(kz-\phi)} e^{-\left(\frac{r^2}{w^2(z)}\right)} e^{-j\left(\frac{kr^2}{2R(z)}\right)} \tag{2.24}$$

where

$$w^2(z) = \frac{b}{k}\left(1 + \frac{z^2}{(b/2)^2}\right) \tag{2.25}$$

$$\frac{1}{R(z)} = \frac{z}{z^2 + (b/2)^2} \tag{2.26}$$

$$\tan\phi = \frac{2z}{b} \tag{2.27}$$

and we define the *confocal parameter* b

$$b = \frac{2\pi w_\circ^2}{\lambda}. \tag{2.28}$$

Eq. (2.24) is a wave traveling in the +z-direction with a Gaussian amplitude profile (given by the second exponential argument) and curved phase fronts of radius $R(z)$ (given by the third exponential argument). The beam radius r, at which the amplitude decreases to $1/e$ of its value on axis is $w(z)$. From Eq. (2.25), we see that the minimum beam radius, or *beam waist* $w_\circ$, is

$$w_\circ = \sqrt{\frac{b}{k}} \tag{2.29}$$

and occurs at the reference location $z = 0$. The confocal parameter b can be consid-

[1] The material in this section comes in large part from reference [14, Chap. 5]

ered as a measure of the "depth of focusing" of the Gaussian beam. If one travels a distance $z = \pm b/2$ from the beam waist, from Eq. (2.25) we see that the beam radius increases to $\sqrt{2}w_o$. Hence, this confocal or "focusing" length is a function of the beam spot size; a smaller beam waist w_o (a "tighter" focus) indicates a shorter focused distance around the waist location. We use the term *near field* to describe propagation in the z-direction within a confocal distance of the waist location, or $|z| < b/2$. Note also from Eq. (2.26) that at the waist location the field is planar ($R(0) = \infty$), and within the confocal distance is assumed to be nearly planar; this is commonly referred to as the *near field approximation.*

2.5.1 Gaussian Beams and Resonators

In the discussion of the Fabry-Perot interferometer, we described a resonance condition that corresponded essentially to perfect standing waves of the electromagnetic field between the mirrors, with nodal planes coincident with the mirror surfaces (round trip phase of $2n\pi$). In the case of circulating plane waves in the cavity, we assumed flat mirror surfaces with infinite transverse dimensions. This assumption is unrealistic when one considers finite mirror dimensions and potential diffraction losses at the mirror boundaries. Curved mirror resonators on the other hand eliminate the effect of mirror boundaries on the mode amplitude distribution and the associated diffraction loss.

Gaussian amplitude profiles are well suited to resonators with curved mirror surfaces. If the resonator mirrors of curvature R_1 and R_2 are placed at distances z_1 and z_2 from the waist of a Gaussian beam such that by Eq. (2.26) the Gaussian beam radius at those distances is equal to the mirror curvature

$$\frac{1}{R_1} = \frac{z_1}{z_1^2 + (b/2)^2} \tag{2.30}$$

$$\frac{1}{R_2} = \frac{z_2}{z_2^2 + (b/2)^2}, \tag{2.31}$$

one may "capture" a standing wave in the cavity. Of course, the spacing between the mirrors has to correspond precisely to an integer number of nodes of the standing wave between the two mirrors.

The Gaussian resonator problem is typically attacked by selecting a set of mirrors of radii of curvature R_1 and R_2 and either their separation distance d (the cavity length) or a target confocal parameter b, and solving for the other parameter. The case of selecting the distance d a priori implies that Eqs. (2.30) and (2.31) must be solved for b under the constraint $z_2 - z_1 = d$. This results in a general solution

$$d = \frac{R_1}{2} + \frac{R_2}{2} \pm \sqrt{\frac{R_1^2}{4} - b^2} \pm \sqrt{\frac{R_2^2}{4} - b^2}. \tag{2.32}$$

After further algebraic manipulation, on may obtain an equation for b^2

$$4b^2 = \frac{R_1^2 R_2^2}{4}\left[\frac{1 - [(2d/R_1R_2)(d - R_1 - R_2) + 1]^2}{[d - (R_1 + R_2)/2]^2}\right]. \tag{2.33}$$

This equation yields real solutions for b only when the numerator is positive. It can be shown that this is the case when

$$0 \leq \left(1 - \frac{d}{R_1}\right)\left(1 - \frac{d}{R_2}\right) \leq 1. \tag{2.34}$$

Eq. (2.34) is the *stability criterion* for Gaussian resonators.

2.5.2 The q-Parameter and Gaussian Beam Transformations

The resonator analysis above was carried out by fitting reflecting boundaries to nodal planes of a standing wave solution. Similar results can be obtained from the q-parameter description of Gaussian beams. This method has the advantage that it gives a concise description of beam transformation by lenses, mirrors and other optical components which is well suited for computer simulation techniques.

A Gaussian beam is completely described by the complex parameter

$$q = z + j(b/2). \tag{2.35}$$

The real part gives the distance from the position of a beam waist, and the imaginary part gives the waist size. Thus, if we know how q transforms, we know how to transform Gaussian beams.

The transformations of q by an optical system may be expressed as a bilinear transform

$$q' = \frac{Aq + B}{Cq + D} \tag{2.36}$$

with the transformation matrix $\begin{bmatrix} A & B \\ C & D \end{bmatrix}$. Such transformation matrices are derived in [14] and [18] for propagation through free space or a medium of index n, a thin lens of focal length f, reflection from a mirror of radius R, and other optical elements. The transformation produced by a cascade of two or more optical elements is the matrix product of the matrices of the individual transformations. For all transformation matrices which relate the input q-parameter in free space to the output q'-parameter in free space, the relation

$$\det \begin{bmatrix} A & B \\ C & D \end{bmatrix} = 1 \tag{2.37}$$

holds. Since the determinant of the product of matrices is equal to the product of determinants, this also holds for any cascade, and serves as a good check for multiple transformations.

q-parameter transformations can be easily applied to resonator structures to obtain the stability criterion given by Eq. (2.34). If a mode is to exist in a resonator, q must repeat itself after one full round trip, i.e. $q = q'$. Once the ABCD matrix for a cavity round trip beam transformation is determined (see [14, Sec. 5.6]), from

Eq. (2.36) we obtain

$$q = \frac{A - D}{2C} \pm \sqrt{\left(\frac{A + D}{2C}\right)^2 - \frac{1}{C^2}} \tag{2.38}$$

where we have used Eq. (2.37). Once the q-parameter at a specific point in the resonator is known, so are all characteristics of the resonant Gaussian beam, including the confocal parameter b, as per Eq. (2.35).

The matrix method of Gaussian beam transformation lends itself more elegantly to computer algorithms which may be constructed to simulate more complex optical systems. For example, using the ABCD matrix approach, the confocal parameter in the nonlinear crystal of the OPO (Sec. 4.3) can be plotted as a function of other parameters such as cavity length. In this way, the desired value of the confocal parameter can be chosen while ensuring that the resonator is stable. Appendix C gives a MATLAB program used to simulate the OPO resonator structure which, given the mirror curvatures, generates confocal parameters and beam waist locations for stable cavity lengths.

Another consideration of Gaussian optics is that of matching the beam parameters from the output of one resonator to that of another for which the beam serves as an input, for example a laser pump source beam which is input to an OPO. This process is called *mode matching* and is addressed in Appendix D. The program of Appendix C also implements the concepts of Appendix D and generates the effective mode matching parameters for the OPO.

2.6 The OPO Double Resonance Threshold

From the coupled wave equations (2.4), (2.5) and (2.6) for parametric down-conversion, an expression can be found for the threshold pump power needed for doubly resonant oscillation to occur in the OPO. As as a starting point, reasonable assumptions are made which simplify the analysis but preserve the important physical results. We

assume first that the OPO resonator is constructed such that the beam waist w_o of the signal and idler beams is located within the crystal, and that the nonlinear interaction is taking place in the near field of the Gaussian beam; hence a plane-wave approximation is used.

The case where the pump wave makes a single pass through the OPO cavity is examined. Since we are looking for solutions for steady state oscillation, we assume the circulating amplitudes E_s and E_i are approximately constant over the length of the crystal. Eq. (2.6) can then be integrated from $z = 0$ to $z = l$ to give

$$E_p(l) = E_p(0) - j\frac{\omega_p d_{eff}}{n_p c} E_s E_i l \left[\frac{\sin(\Delta kl/2)}{\Delta kl/2}\right] e^{j(\Delta kl/2)}. \tag{2.39}$$

Making use of the relationship between the steady state signal and idler waves [4]

$$\frac{E_s^2}{E_i^2} = \frac{\omega_s n_i \alpha_i}{\omega_i n_s \alpha_s} \tag{2.40}$$

as well as Eq. (2.14), the threshold pump intensity required for the parametric gain to overcome the cavity losses can be found to be

$$I_{th}(\omega_p) = \frac{\alpha_s \alpha_i n_s n_i n_p c^3 \epsilon_o}{2\omega_s \omega_i l^2 d_{eff}^2} \left[\frac{(\Delta kl/2)^2}{\sin^2(\Delta kl/2)}\right]. \tag{2.41}$$

As the phase mismatch Δk increases, so does the minimum pump power needed for oscillation, i.e. momentum conservation results in the lowest pump threshold. The threshold pump power is obtained by multiplying the threshold intensity by the effective area of the Gaussian pump beam (Appendix E) in the interaction region.

The exact form of the pump threshold power relationship has been calculated by Boyd and Kleinman [6], who assumed fractional *round trip* losses κ_p, κ_s and κ_i and focused Gaussian beams for the pump, signal and idler modes, respectively. They showed using a rigorous calculation that the single-pass pump threshold power is given

by

$$P_{th}(\omega_p) = \frac{\pi \kappa_s \kappa_i n_p n_s n_i \epsilon_o c^3}{8 l \omega_s \omega_i d_{eff}^2 k_o \overline{h}(B,\xi)(1-\delta^2)} \tag{2.42}$$

where $k_o = 2\pi n_o/\lambda_o$ and λ_o is the degenerate wavelength. The term δ is the fractional deviation from degeneracy defined by

$$\delta = \frac{\omega_s - \omega_o}{\omega_o} \tag{2.43}$$

where $\omega_o = \omega_p/2$ is the degenerate angular frequency. The dimensionless quantity $\overline{h}(B,\xi)$ introduced by Boyd and Kleinman is a function of the degree of focusing of the respective waves within the crystal and also depends upon the amount of double refraction due to crystal birefringence, or *walkoff*. This is explained further in Sec. 4.3.1 as it pertains particularly to the nonlinear crystal employed in the OPO design. If we assume nearly degenerate outputs ($\omega_s \approx \omega_i \approx \omega_o$), we may simplify Eq. (2.42) somewhat, yielding

$$P_{th}(\omega_p) = \frac{\pi \kappa_s \kappa_i n_p n_s \epsilon_o c^4}{8 l \omega_o^3 d_{eff}^2 \overline{h}(B,\xi)} \tag{2.44}$$

where the signal index n_s has been arbitrarily substituted for the degenerate index n_o. This form of the pump threshold power serves as a useful estimation and is applied to the OPO design and characterization in Sec. 4.5.

2.7 The Intensity Correlation Spectrum

In Sec. 1.5 a model for the intensity correlation spectrum [27] was introduced for the signal and idler twin beam outputs of the OPO, which we repeat here for convenience

$$S_{ID}(f) = 1 - \left[\frac{\eta \left(1 - \frac{\mu}{T+\mu}\right)}{1 + \frac{f^2}{\Delta f^2}} \right]. \tag{2.45}$$

This relation was rigorously developed in [10]. It has been shown earlier through the Manley-Rowe relations that the process of parametric down-conversion emits pairs of simultaneous photons each time a pump photon is annihilated, generating twin beams which have exactly the same photon statistics; there is no noise on the intensity difference. In the OPO, the cavity placed around the crystal induces some decorrelation between the two beams.

The quantum noise reduction in the intensity difference spectrum is Lorentzian in profile. For noise frequencies outside the cavity bandwidth Δf, the noise spectrum returns to the standard quantum (shot noise) limit. For zero noise frequency (DC), the noise spectrum can ideally be reduced to zero. Degradations from this ideal are due to optical losses in the system, which occur both in the optical cavity, where the twin beams are generated, and in the photodiodes, where they are detected. Improvements in noise reduction require improvements in both the detection efficiency η and the ratio of output coupling to total losses, $T/(T+\mu)$. In Ch. 4 all sources of loss in the OPO are determined, and in Sec. 4.5 the effects of the various sources of loss on the intensity correlation given by Eq. (2.45) are examined.

The model of Eq. (2.45) assumes equivalent cavity losses for the orthogonally polarized signal and idler light. This is an idealized approach, for while the cavity end-mirrors may indeed be insensitive to polarization, the birefringent nonlinear crystal may have substantially different absorption properties or scattering from anti-reflective end-face coatings for each polarization. Lane *et al.* [20] has shown that the intensity noise spectrum of an OPO operated just above threshold is sensitive to the signal-idler cavity loss matching, such that the low frequency noise can rise dramatically above the shot noise level. Subsequently, Leong [23] and Wong *et al.* [39] have shown that excess pump noise further reduces the intensity correlation spectrum at low frequencies in the presence of cavity loss mismatch.

Given signal, idler and pump round trip cavity losses $\kappa_{s,i,p}$, output coupler transmission γ (we have previously referred to this as T, but we use here the notation

of the references), and the cavity free spectral range (FSR), the analysis of [23] and [39] begins with the definitions of various loss rates (in Hz) given by

$$\begin{aligned} \kappa &= \frac{(\kappa_s + \kappa_i)FSR}{2\pi} \\ \delta &= \frac{(\kappa_s - \kappa_i)FSR}{2\pi} \\ \kappa_p^{'} &= \frac{(\kappa_p)FSR}{2\pi} \end{aligned}$$

where κ is the sum of the loss rates for the signal and idler beams, δ is the difference of the loss rates, and $\kappa_p^{'}$ is the pump loss rate. Additional loss related parameters are defined

$$\begin{aligned} \Gamma &= \frac{1}{2}\left(\frac{\gamma}{\kappa_s} + \frac{\gamma}{\kappa_i}\right) \\ g &= \frac{1}{2}\left(\frac{\gamma}{\kappa_s} - \frac{\gamma}{\kappa_i}\right)/\Gamma \end{aligned}$$

where Γ is a normalizing factor used to determine g, which describes the signal-idler loss mismatch. A parameter which expresses the pump field strength above threshold is given by

$$\epsilon = \sqrt{\frac{P_p}{P_{th}}} - 1$$

where P_p is the pump power and P_{th} is the threshold power. Finally, the parameters are defined

$$D(f) = (\kappa^2 - \delta^2)\kappa_p^{'}\epsilon - f^2(\kappa_p^{'} + \kappa) - jf[\kappa\kappa_p^{'}(\epsilon + 1) - f^2]$$

$$Z_1(f) = (\kappa + \delta)\left\{\frac{1}{\kappa - jf} - \frac{\kappa - jf - \delta}{D(f)}\left[\frac{\delta\kappa_p^{'}\epsilon}{\kappa - jf} - g(\kappa_p^{'} - jf)\right]\right\}$$

$$Z_2(f) = (\kappa - \delta)\left\{\frac{1}{\kappa - jf} - \frac{\kappa - jf + \delta}{D(f)}\left[\frac{\delta\kappa_p'\epsilon}{\kappa - jf} - g(\kappa_p' - jf)\right]\right\}.$$

The difference intensity noise spectrum at the output of the OPO is then given by

$$\begin{aligned} S_{out}(f) &= \left\{1 + \frac{1}{2}\Gamma(|Z_1(f)|^2 + |Z_2(f)|^2) - \left(\frac{\gamma}{\kappa_s}\mathrm{Re}[Z_1(f)] + \frac{\gamma}{\kappa_i}\mathrm{Re}[Z_2(f)]\right)\right\} \\ &+ \frac{2\Gamma\kappa_p'^2\epsilon}{|D(f)|^2}[g^2(\kappa^2 - \delta^2)^2 + f^2(g\kappa + \delta)^2]h(f) \end{aligned} \tag{2.46}$$

where $h(f)$ is the excess pump noise spectrum. The last term in Eq. (2.46), proportional to $h(f)$, is the pump-induced noise. The g^2 coefficient in this term reflects the sensitivity of the spectrum to the cavity loss mismatch. The special case of an OPO with no internal losses ($g = 0$, $\Gamma = 1$) and well balanced output couplings ($\delta = 0$) yields Eq. (2.45) for $\eta = 1$.

Finally, if we consider the detection efficiency n, the detected intensity correlation spectrum in the presence of signal-idler loss mismatch and excess pump noise is then given by

$$S_{ID}(f) = \eta S_{out}(f) + (1 - \eta) \tag{2.47}$$

where we have taken η to be the average detection efficiency of the signal and idler beam paths. Appendix F implements the above formulation for intensity correlation using the conditions and parameters of this experiment, as discussed in Sec. 5.7. The excess pump noise spectrum is given in Sec. 3.5.

2.8 Elements of Servo Control

The term *servo* refers to a device or system for automatically correcting the performance of a mechanism. In bulk optics, one is often interested in optical cavities with fixed and stable lengths. Often it is desirable to precisely control the length of a cavity and monitor its effect on the optical system; for this, a feedback or servo

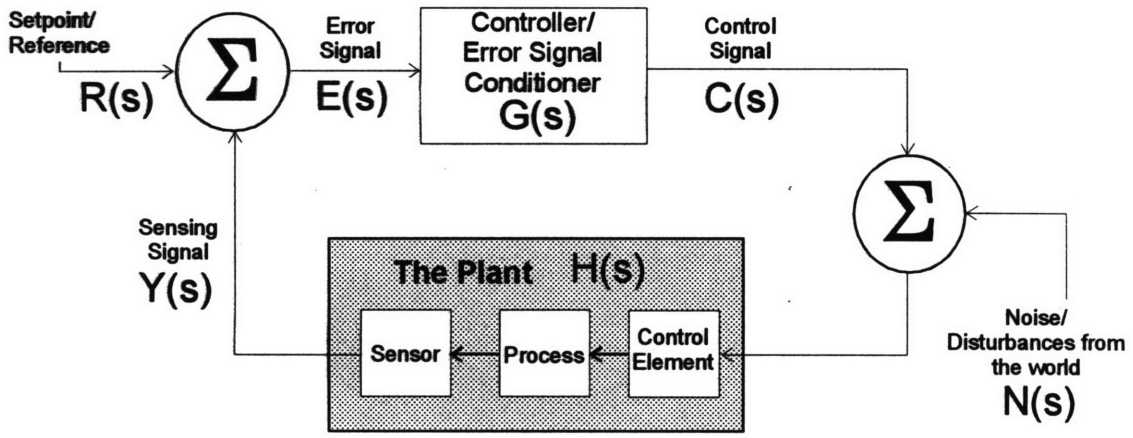

Figure 2.5: Block diagram of a servo control system

control system is required.

Throughout this experiment, concepts of servo control are implemented in various configurations to stabilize the intensity and frequency of the laser pump source as well as the OPO cavity lengths in order to achieve stable continuous wave output. In this section we review some of the basic elements of servo control and the electronic building blocks used in many of the implementations encountered here.

Fig. 2.5 gives a block diagram of a servo control system with some of the general terminology. The mechanism that is desired to be controlled is called the *process.* For each process, there must be a means by which we can actuate some change in the process as well as a method of detecting this change; these are referred to as the *control element* and *sensor*, respectively. The system of control element, process and sensor is termed the *plant.*

Servo control functions as follows: a *sensing signal* from the plant is compared to a *reference setpoint*, which is some signal that is equivalent to the desired per-

formance of the process. Comparing the sensing signal to the setpoint results in an *error signal.* If the process is performing as desired, the sensing signal will be equal to the setpoint and the resulting error signal will be zero. If there is however an error signal, the servo control system must take some action to correct for this performance error. The error signal is therefore interpreted or conditioned by a *controller* which generates a *control signal* to the control element of the plant, thereby initiating some corrective action. Once the process responds and any change is detected by the sensor, the sensing signal is again compared to the setpoint. The goal of the servo control system is to drive the error voltage to zero, where the system will be *at rest.*

The servo control system accomplishes its goal by *negative feedback.* This is typically accomplished through the design of the controller, which insures that the error signal conditioning will effect changes in the plant that result in a decreased error signal. Other issues of control regard the *dynamic response* of the system, which describes how fast and how accurately the system can reach and maintain a desired performance setpoint. Here, disturbances and noise must be considered in the context of perturbations to the process which cause it to deviate from the setpoint. Because the controller is essentially the "backbone" of the servo control system, we will concentrate on controller methodology and performance as it relates to the servo systems used in the experiment.

We first examine the complete system using s-domain (Laplace) analysis [11]. From Fig. 2.5 we have

$$\begin{aligned} E(s) &= R(s) - Y(s) \\ C(s) &= E(s)G(s) \\ &= G(s)[R(s) - Y(s)] \\ Y(s) &= H(s)[C(s) + N(s)] \\ &= H(s)\{G(s)[R(s) - Y(s)] + N(s)\} \end{aligned}$$

$$= H(s)G(s)R(s) - Y(s)G(s)H(s) + N(s)H(s)$$

which, after regrouping terms, results in the sensing signal

$$Y(s) = \left(\frac{G(s)H(s)}{1 + G(s)H(s)}\right) R(s) + \left(\frac{H(s)}{1 + G(s)H(s)}\right) N(s) \tag{2.48}$$

where the quantity $G(s)H(s)$ is termed the *loop gain.*

Whereas the plant response $H(s)$ is more or less fixed, servo control system response can be implemented through design of the controller $G(s)$. There are three basic types of controller design, *proportional, integral* and *differential* control. These designs may be implemented separately or in various combinations to tailor the dynamic response of the system. For our purposes here, we compare only proportional vs. integral control, from which our design choice becomes apparent.

In proportional control, $G(s)$ is equal to some constant K which is independent of frequency. If for the moment we assume no noise or disturbances, we have

$$Y(s) = \left(\frac{KH(s)}{1 + KH(s)}\right) R(s).$$

If both $H(s)$ and K are very large, then $Y \approx R$, or the system will drive the plant to very close to the setpoint. There will however always be some steady state error. If we additionally consider the effect of a disturbance on the system with $R(s) = 0$

$$Y(s) = \left(\frac{H(s)}{1 + KH(s)}\right) N(s)$$

again Y will not go to zero as required by the setpoint; there will be some steady state error.

With integral control, the controller has the basic function of an integrator, where

$$G(s) = K/s. \tag{2.49}$$

The primary advantage of integral control is to reduce or eliminate constant steady state errors. The feedback mechanism including the integral controller has the primary virtue of being able to provide a finite value of control signal $C(s)$ with no error signal $E(s)$. This is because $C(s)$ is a function of all past values of $E(s)$ rather than just the current value, as in the proportional control case. In essence, the system has "memory", and past errors "charge up" the integrator to some value that will remain, even if the error is reduced to zero. This implies that any disturbance $N(s)$ can be cancelled with no residual steady state error, because $E(s)$ no longer has to be non-zero to produce a control signal to counteract the disturbance. By substituting Eq. (2.49) into Eq. (2.48), it can be observed that at DC ($s = 0$), $G(s)$ has infinite gain and that the system will be driven to $Y = R$ with no steady state error.

Another practical consideration of integral control is the system's frequency response. The control element employed in the system is often the limiting factor in the system's dynamic response, and is indeed the case for three of the four servo systems employed for this experiment (The piezoelectric actuator attached to a cavity mirror for control of cavity length has a response time on the order of $\tau = 2\mu$s, or a frequency response bandwidth $\Delta f = 1/2\pi\tau \approx 80$kHz, see Ch. 4). The frequency response of an integral controller can be tailored around the control element such that disturbances beyond the response range of the element can be significantly attenuated.

The frequency response of a typical single-pole integrator is 20 dB/decade, with a constant phase of 90°. Other issues of integral control include *gain margin* and *phase margin*, in which the system is insured to maintain a negative feedback configuration regardless of the frequency response. Fig. 2.6 shows two standard integrator building blocks used commonly in the controller circuits of this experiment, with their transfer functions $H(f)$ as well as their magnitude and phase frequency characteristics. Combinations of these circuits provide the necessary high gain at low frequencies and rapid roll-off well within the bandwidth of the control element, while insuring adequate gain and phase margins to maintain negative feedback. Specific

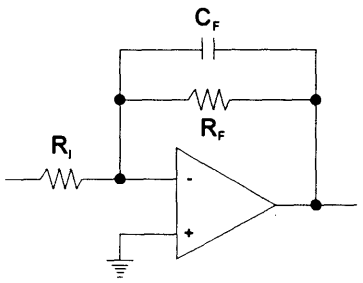

$$H(f) = \frac{-R_F}{R_I}\left[\frac{1}{1+j\frac{f}{f_p}}\right], \quad f_p = \frac{1}{2\pi R_F C_F}$$

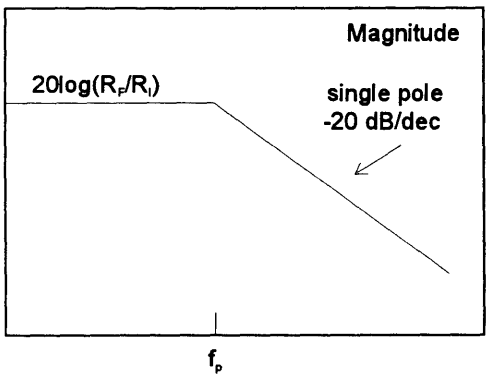

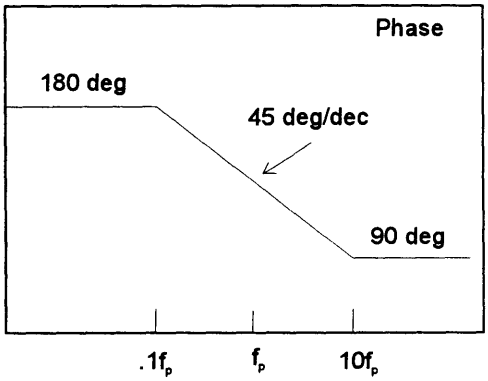

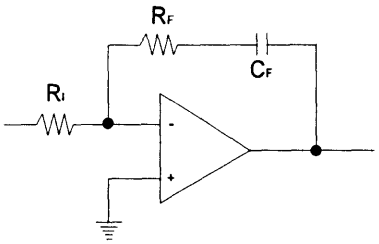

$$H(f) = \frac{-R_F}{R_I}\left[1+\frac{1}{j\frac{f}{f_z}}\right], \quad f_z = \frac{1}{2\pi R_F C_F}$$

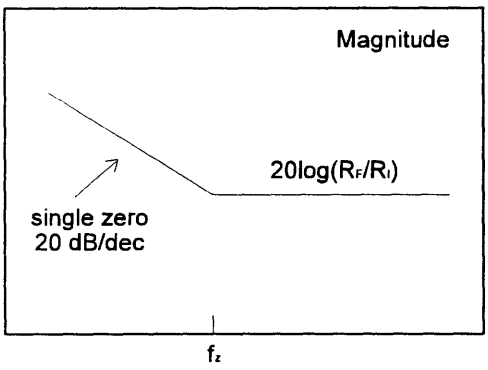

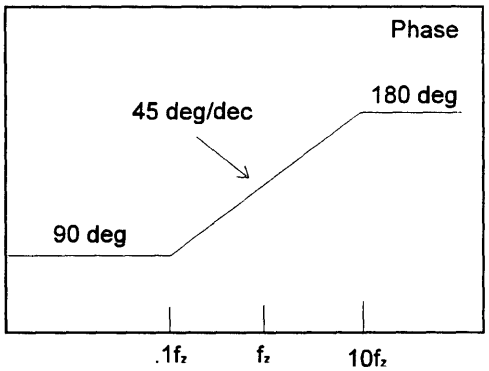

Figure 2.6: Transfer functions $H(f)$ for integrator circuits used in servo controllers and their magnitude and phase frequency response.

controller circuit designs are discussed in Ch. 3 for frequency stabilization of the pump laser system as well as in Ch. 5 for stabilization of the pump resonator and OPO cavity lengths. These circuits were simulated using the PSPICE [2] micro-circuit design center which generated the frequency and phase response curves that accompany the circuit schematics.

2.9 Summary

In this chapter, we have presented the useful theoretical concepts relevant to the experiment, including a description of nonlinear wave interactions of parametric amplification, a quantum-photon viewpoint of the down-conversion process, and a review of basic optics concepts including Fabry-Perot resonators and Gaussian beams. The oscillation threshold of the OPO was discussed along with models for the intensity correlation spectrum of the twin beam outputs. Finally, we examined some basic concepts of servo control which were useful throughout the experiment for stabilization of the pump laser intensity and frequency, as well as the OPO cavities.

[2]PSPICE is a trademark of MicroSim Corporation, Irvine, CA

Chapter 3

Pump Laser System

3.1 Introduction

The main purpose of the pump laser system is to provide an appropriate pump beam for the OPO. The triply resonant condition of the OPO places stringent requirements on the intensity and frequency stability of the input pump laser. Any intensity or frequency fluctuation in the input field is transferred to the OPO outputs.

Excess pump intensity noise above the shot noise level can degrade the intensity correlation of the OPO outputs due to the unavoidable small mismatch in signal and idler losses (as shown in Ch. 2). This may not be a serious problem if one can work at a higher frequency range where the laser is shot noise limited. However, significant low frequency intensity fluctuations could contribute uncertainty to the DC optical power level, making OPO cavity stabilization more difficult.

Fluctuations in pump frequency would also have an adverse effect on OPO cavity stabilization. The OPO signal-idler frequency difference is approximately immune to the pump frequency noise. This implies that the individual signal and idler frequency undergoes a frequency deviation that is equal to half of the input pump frequency deviation. Since the OPO IR cavity linewidth is on the order of 18 MHz (see Chap. 4, Table 4.3), any pump frequency fluctuation that is larger than 36 MHz can prevent the OPO from sustaining a cw oscillation. This places an upper limit on the allowable pump frequency fluctuation (the linewidth of the OPO pump resonator cavity is on the order of 20 MHz, which is a less stringent requirement).

In this chapter, we will describe the laser source and the techniques employed

for intensity and frequency stabilization (Fig 3.1). Since elements of this system were previously utilized in references [23, 19, 21] some aspects have been covered in detail in those references. Additionally, an excellent tutorial of the relevant concepts in laser related servo control systems is given in [13]. Here, we will provide brief descriptions of the source and intensity stabilization techniques, while providing a more rigorous treatment of the frequency stabilization. Finally, we will characterize the excess pump intensity noise spectrum after stabilization.

3.2 The Krypton Ion Laser

The pump laser was a Coherent INNOVA 200 krypton ion (Kr^+) laser operating at a wavelength of 530.9 nm with a single transverse and longitudinal mode. The choice of wavelength results from the fact that the properties of the crystal used in the experiment have been extensively studied at 532.1 nm and its subharmonic at 1064 nm. Many factors are favorable at these wavelengths, including a convenient phase-matching temperature and low crystal losses. Moreover, krypton ion lasers have a strong line at 530.9 nm.

The krypton ion laser consists of a two mirror linear cavity (Fig. 3.2). The laser gain medium is contained in a tube filled with ionized krypton gas. The ends of the tube are at Brewster's angle to reduce losses and to obtain linearly polarized output light. The krypton ions are excited by passing an electric current through the gas along the length of the tube.

The laser can be operated with one line or multiple lines. For single frequency operation, the laser cavity contains a prism which bends light of different wavelengths at different angles. At a fixed back mirror position, only one wavelength is bent at the proper angle to oscillate back and forth between the cavity mirrors. All other wavelengths are reflected out of the laser cavity by the back mirror, preventing oscillation at those wavelengths. The prism/back mirror combination can then be tuned

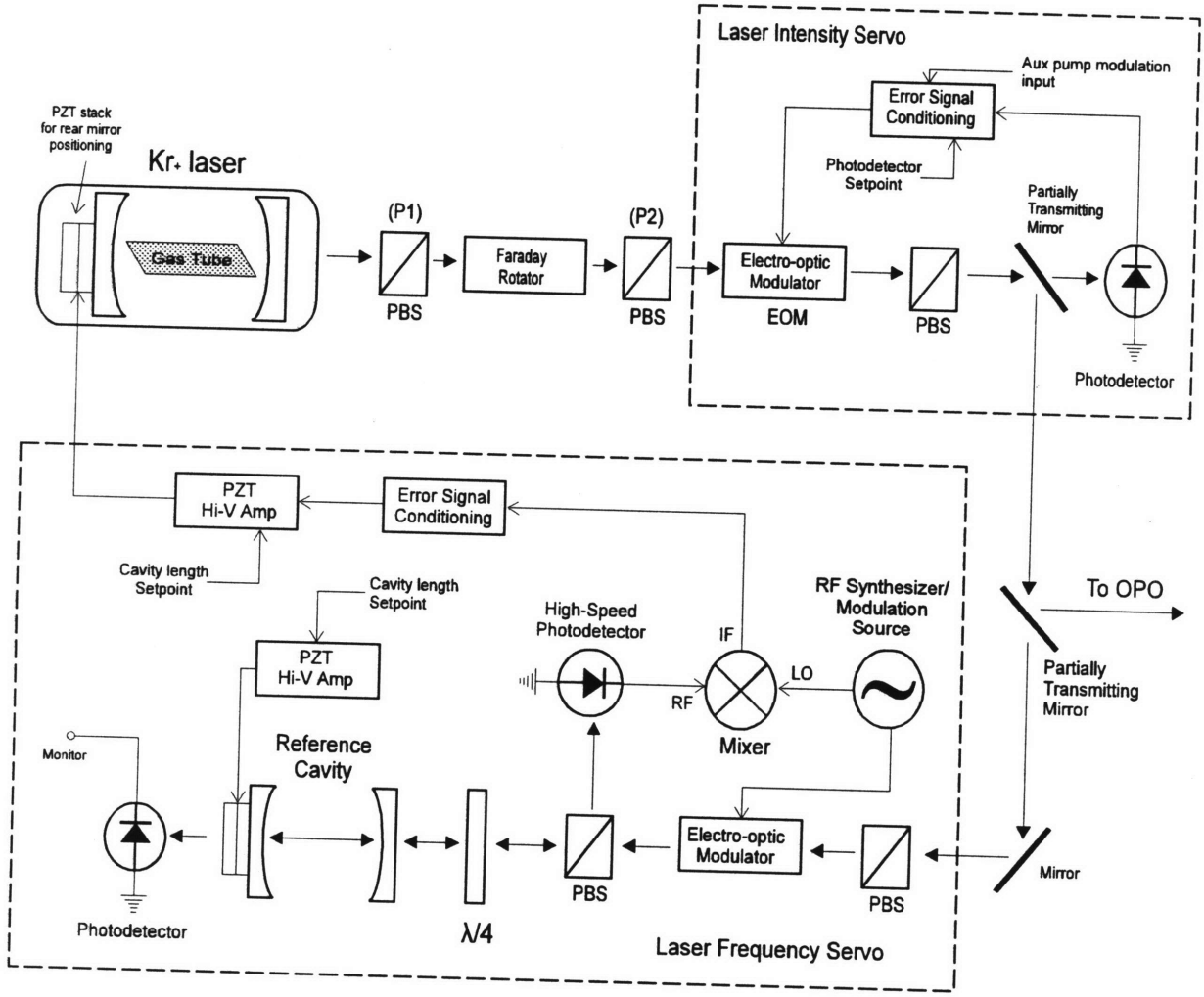

Figure 3.1: Block diagram of the laser pump system

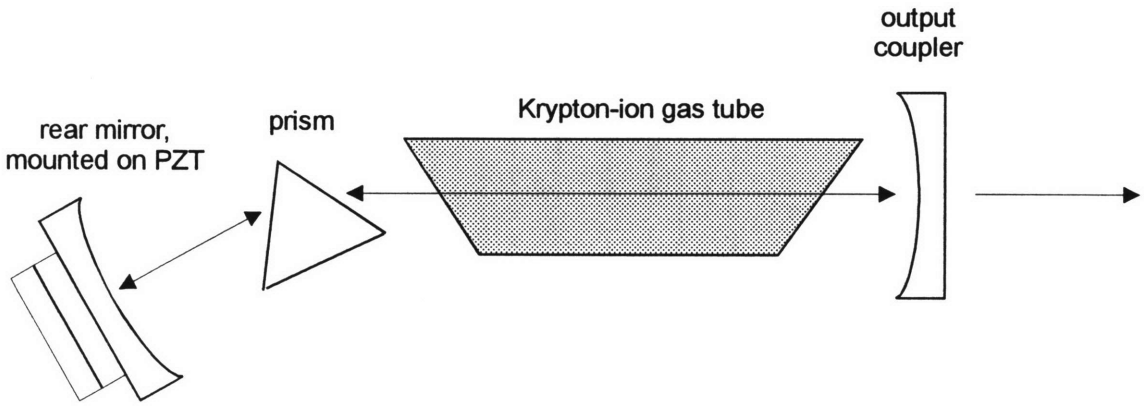

Figure 3.2: The krypton-ion laser.

to select the output wavelength.

The laser exhibited a significant amount of intensity and frequency noise at low frequencies around 400 Hz, caused by the laser's plasma tube structural vibrations induced by the flow of coolant water inside the laser. Under free running conditions, the laser peak-to-peak intensity noise was ~2.6% at 400 mW with an estimated frequency jitter of $\geq \pm 20$ MHz. Table 3.1 summarizes the relevant properties of the Coherent INNOVA 200 laser.

The laser output passed through a Faraday isolator which was used to block any optical feedback from entering the laser cavity. Such a device was especially necessary since there was a strong back-reflection from the OPO when it was well aligned. The isolator consisted of two polarizing beam splitters (PBS) and a Faraday rotator (Fig. 3.1); it allowed a light beam to travel through it in one direction but not in the opposite one.

Light passing in the forward direction (from left to right) was linearly polarized by the input polarizer P1. The Faraday rotator produced a rotation of 45°; for purposes of illustration, let us say in the clockwise sense. The second polarizer P2 was set at 45° to P1 so that it transmitted light emerging from the rotator. However,

Single frequency line	530.9 nm
Beam quality	TEM_{00}
Cavity Configuration	15 m radius output coupler Flat back high reflector mounted on PZT Prism and etalon for single line operation
Cavity length	1.95 m
Maximum Power	400 mW
Free Spectral Range (FSR)	76 MHz
Intensity Noise	~2.6% at 400 mW output power
Frequency Jitter	$\geq \pm 20$ MHz
Beam parameters for mode matching:	
Effective Confocal Parameter, b_{eff}	8.825 m
Effective waist location, t_{eff}	2.5544 m from front surface of laser

Table 3.1: Coherent INNOVA 200 krypton-ion laser output properties.

a beam entering from the right was plane polarized at 45° by P2, and then had its plane rotated by 45°, again in the clockwise sense due to the nonreciprocal property of the rotator [37]. It was therefore incident on P1 with its plane of polarization at right angles to the plane of transmission and was eliminated. The device thus isolated the components on its left from light incident from the right. The Faraday isolator used in the experiments provided 40 dB (0.01%) isolation.

3.3 Intensity Stabilization

The laser intensity was actively controlled by a feedback servo loop to reduce the intensity noise and to allow for adjustment of the incident power to the OPO. Referring to Fig. 3.1, the intensity servo consisted of an electro-optic modulator (EOM, Conoptics Model 370), a polarizing beam splitter (PBS), a partially transmitting mirror (T=0.6%), a photodetector and an amplifier for error signal conditioning.

The photodetector measured a small portion of the laser beam, and its electri-

cal output was compared with a DC voltage reference level inside the servo amplifier. This voltage established the setpoint of the servo loop, which represented the electrical equivalent of the desired system power output. The output of this comparison constituted the loop's error signal, which was fed through a high gain integration stage that limited the bandwidth of the error signal to within the physical constraints of the system (the bandwidth of the EOM driver was ~1 MHz.) An auxiliary input port was included in the amplifier circuit to permit an external signal and the conditioned intensity error signal to be summed before the EOM, thus providing a means for pump laser amplitude modulation (the utility of this will be addressed in the experimental chapter).

The electro-optic modulator was used in conjunction with the polarizer as an intensity modulator [37]. In response to the error signal, the EOM rotated the polarization of the incoming linearly polarized laser field. After passing through the EOM only the portion of the E-field along the transmitting axis of the second polarizer was propagated; in this manner, the PBS acted as a polarization analyzer. By changing the voltage applied to the EOM and hence the amount of rotation of the E-field vector, the transmitted intensity was controlled. Due to some power being rejected by polarization rotation and the subsequent analyzer, the maximum pump power available after intensity stabilzation was on the order of 160 mW. The intensity servo loop had a measured unity-gain bandwidth of 1 MHz [21] and reduced peak to peak intensity noise fluctuations from approximately 2.6% to .5%.

3.4 Frequency Stabilization

The laser frequency was stabilized per the method of Drever, *et al.* [9]. Since this method of stabilzation relies primarily on phase modulation, it is instructive to first briefly review the basic concepts and terminology associated with phase modulation in order to facilitate a thorough theoretical and experimental description of the frequency

stabilization technique.

3.4.1 Phase Modulation

In general, we may express a signal which has been phase modulated by [35]

$$\phi_{pm}(t) = A\cos(\theta(t)) \tag{3.1}$$

where

$$\theta(t) = \omega_c t + k_p f(t) \tag{3.2}$$

so that, combining Eqs. (3.1) and (3.2),

$$\phi_{pm}(t) = A\cos(\omega_c t + k_p f(t)). \tag{3.3}$$

A is the signal amplitude, ω_c is the carrier frequency, k_p is the phase modulation constant and $f(t)$ is the modulating signal. The *instantaneous frequency* of the phase modulated signal is defined as

$$\omega_i(t) \equiv \frac{d\theta(t)}{dt} = \omega_c + k_p \frac{df(t)}{dt}. \tag{3.4}$$

Let us consider the case of a sinusoidal modulation, where

$$f(t) = a\cos(\omega_m t) \tag{3.5}$$

so that the instantaneous frequency of the phase modulated signal is given by

$$\omega_i(t) = \omega_c - ak_p\omega_m \sin(\omega_m t). \tag{3.6}$$

We then define the *peak frequency deviation*

$$\begin{aligned} \Delta\omega &\equiv \max \mid \omega_i(t) - \omega_c \mid \\ &= \max \mid \omega_c - ak_p\omega_m \sin(\omega_m t) - \omega_c \mid \\ &= ak_p\omega_m \end{aligned} \tag{3.7}$$

where a is the amplitude and ω_m is the frequency of the modulating signal. Next, we define the *modulation index* β, as

$$\beta \equiv \frac{\Delta\omega}{\omega_m} = ak_p. \tag{3.8}$$

The modulation index β has the units of radians, is proportional to the amplitude of the modulating signal through the phase modulation constant k_p and serves as a guide to the behavior of the carrier and sidebands generated by the phase modulation, as we shall soon show. We may now rewrite the sinuosoidally phase modulated signal from Eq. (3.3) as

$$\begin{aligned} \phi_{pm}(t) &= A\cos(\omega_c t + \beta\cos(\omega_m t)) \\ &= \mathrm{Re}(Ae^{j\omega_c t}e^{j\beta\cos\omega_m t}). \end{aligned} \tag{3.9}$$

The function $e^{j\beta\cos\omega_m t}$ has period $T = 2\pi/\omega_m$ and so it has a Fourier series

$$e^{j\beta\cos\omega_m t} = \sum_{n=-\infty}^{\infty} F_n e^{jn\omega_m t} \tag{3.10}$$

where

$$F_n = \frac{1}{T}\int_{-T/2}^{T/2} e^{j\beta\cos\omega_m t}e^{-jn\omega_m t}dt. \tag{3.11}$$

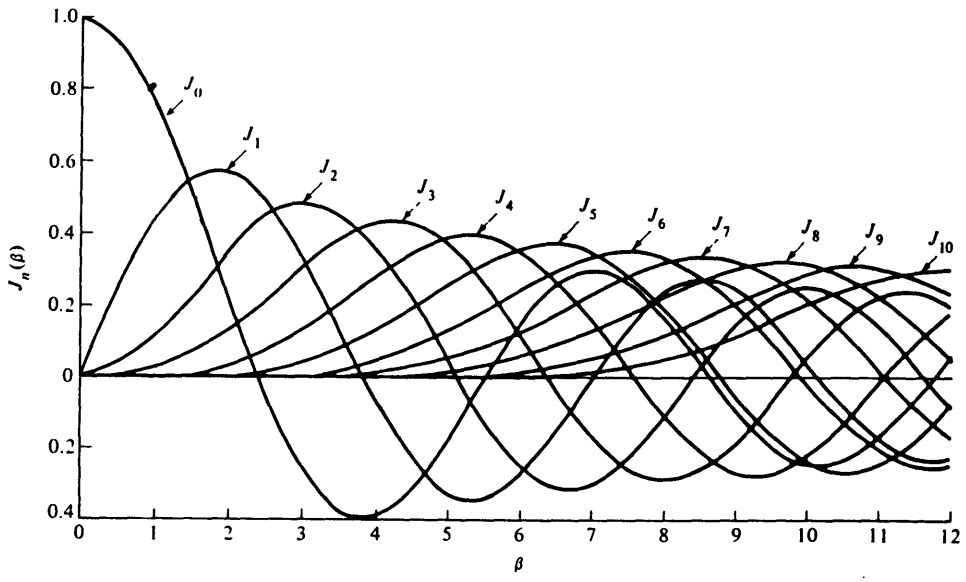

Figure 3.3: Plot of Bessel Function of the first kind, $J_n(\beta)$. From [35].

Setting $u = \omega_m t$ yields

$$F_n = \frac{1}{2\pi}\int_{-\pi}^{\pi} e^{j(\beta\cos u - nu)}du \equiv J_n(\beta). \tag{3.12}$$

The function $J_n(\beta)$ is well characterized and real valued, and known as a Bessel function of the first kind of order n and argument β (Fig. 3.3). Using the Bessel functions, we can write

$$e^{j\beta\cos\omega_m t} = \sum_{n=-\infty}^{\infty} J_n(\beta)e^{jn\omega_m t} \tag{3.13}$$

so that, from Eq. (3.9)

$$\begin{aligned}\phi_{pm}(t) &= \mathrm{Re}\left(Ae^{j\omega_c t}\sum_{n=-\infty}^{\infty} J_n(\beta)e^{jn\omega_m t}\right)\\ &= A\sum_{n=-\infty}^{\infty} J_n(\beta)\cos(\omega_c + n\omega_m)t.\end{aligned} \tag{3.14}$$

In this case, each term $J_n(\beta)$ determines the magnitude of a sideband of the signal. In particular, if we look at the Fourier transform of Eq. (3.14), we have in the frequency

domain

$$\Phi_{pm}(\omega) = A\pi \sum_{n=-\infty}^{\infty} J_n(\beta)[\delta(\omega - (\omega_c + n\omega_m)) + \delta(\omega + (\omega_c + n\omega_m))]. \tag{3.15}$$

From the sumnation, it appears that we have an infinite number of sidebands, and hence an infinite bandwidth. However, from Eq. (3.12) we note that

$$|J_n(\beta)| \approx 0, \quad (n \gg \beta) \tag{3.16}$$

so that as a reasonable approximation for large β, the last important sideband occurs around $n = \beta$, resulting in a bandwidth

$$BW \approx 2\beta\omega_m \approx 2\Delta\omega. \tag{3.17}$$

For small β (< 1), only the first two sidebands are important, and

$$BW \approx 2\omega_m. \tag{3.18}$$

Carson's Rule combines these two facts as

$$\begin{aligned} BW &\approx 2(\Delta\omega + \omega_m) \\ &= 2\omega_m(1 + \beta). \end{aligned} \tag{3.19}$$

This approximation is considered valid for general modulating signals as well. Fig. 3.4 shows examples of the magnitude spectrum of a phase modulated signal for small and large β.

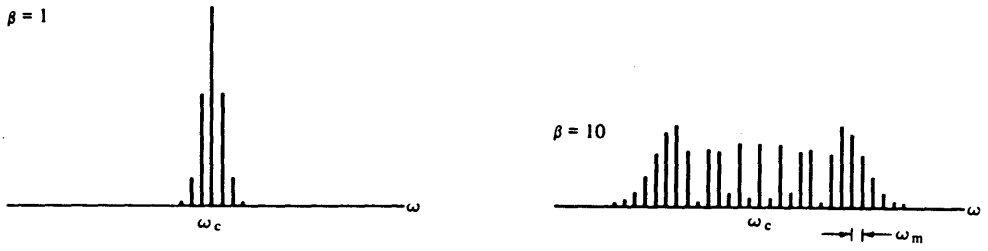

Figure 3.4: Magnitude spectrum of a phase modulated signal, a) for $\beta = 1$ and, b) for $\beta = 10$. From [35].

3.4.2 The Pound-Drever Implementation

The Pound-Drever implementation presented in [9] employed phase modulation of the laser output "carrier" beam by a radio frequency (rf) sinuoisdal signal. A novel optical technique based on signals reflected from a stable Fabry-Perot reference cavity provided a discriminator signal which allowed locking the laser output frequency to the resonant frequency of the reference cavity. Fig. 3.1 shows a block diagram of the frequency stabilization scheme, while Fig. 3.5 shows the details of the setup. The major components of the frequency servo loop included an electro-optic modulator (Conoptics Model 370), a Zerodur reference cavity, a high speed photodetector, an rf synthesizer, an electronic mixer for demodulation, error signal conditioning electronics and a PZT mirror actuator for the back mirror of the laser source. The selected modulation frequency for the laser sidebands was 15 MHz with a modulation index β of 1.1. The choice of modulation frequency and β will be made clear in the following discussion.

The modulation source was a Stanford Research Systems (SRS) model DS345 frequency synthesizer, with an output of -7 dBm. This was subsequently amplified by a Mini-Circuits model ZHL-1-2W amplifier with a gain of ~33 dB. The amplifier output was sent to a Mini-Circuits model ZDC-10-1 directional coupler. The primary

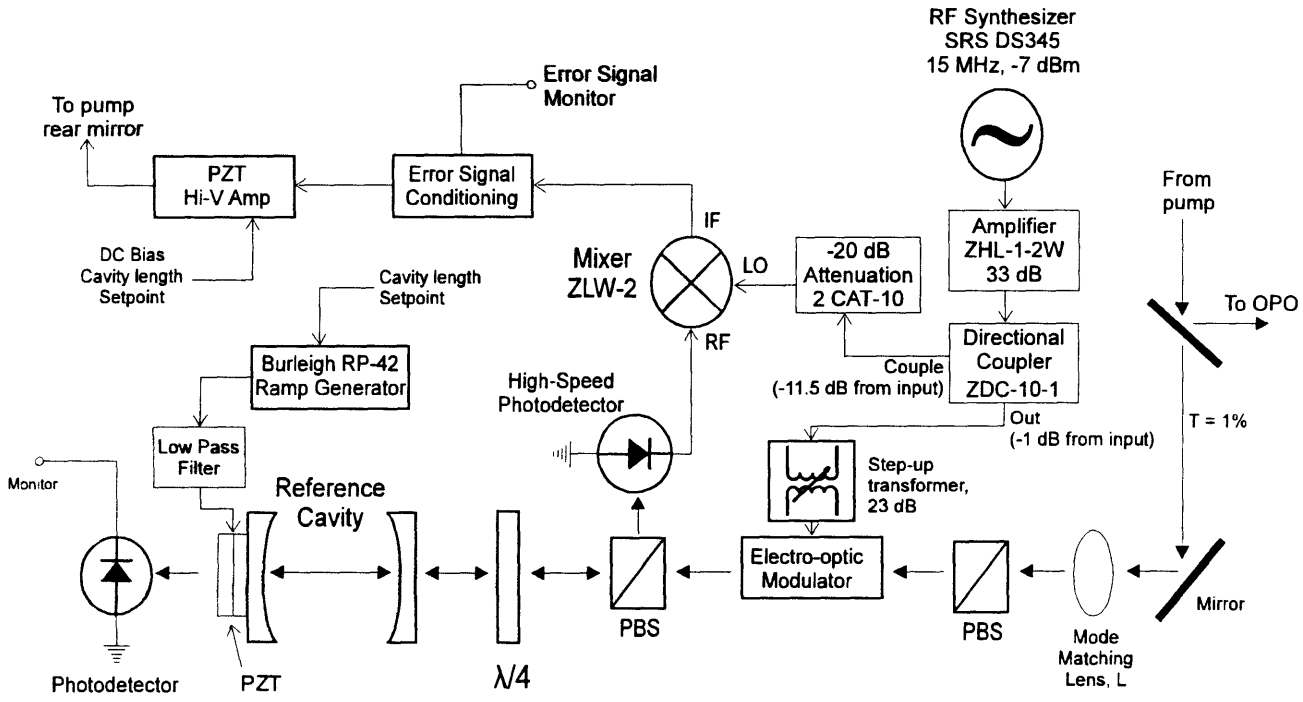

Figure 3.5: Detail of Pound-Drever frequency stabilization implementation

output of this coupler (~1 dB below the input) was fed to a step-up transformer with a gain of ~23 dB and then to the electro-optic modulator. The signal arriving at the modulator therefore had an amplitude of ~80 V. The Conoptics modulator had a response (phase modulation constant k_p) of ~14 mrad/V at $\lambda = 532$ nm. β was then given by

$$\begin{aligned} \beta &= ak_p \\ &\approx 80 \text{ V X } .014 \frac{\text{rad}}{\text{V}} \\ &\approx 1.1 \text{ rad.} \end{aligned}$$

The secondary output of the coupler (11.5 dB below the primary output) was attenuated by 20dB to -5 dBm via two Mini-Circuits model CAT-10 attenuators, and served as the local oscillator for demodulation of the photodetector signal, to be explained later.

Table 3.2 gives the relevant physical parameters of the reference cavity. To

Cavity Length	20.7 cm
Mirror Reflectivities	99.4%
Mirror Thickness	1 cm
Free Spectral Range (FSR)	725 MHz
Finesse (F), measured	514
Linewidth (FWHM)	1.4 MHz
Beam parameters for mode matching:	
Effective Confocal Parameter, b_{eff}	20.483 cm
Effective waist location, t_{eff}	11.55 cm from front surface of input coupler

Table 3.2: Reference cavity physical parameters.

improve isolation from vibrations that were transmitted through the optical table, the reference cavity was placed on top of Sobrothene absorbers, a soft damping material.

A portion of the pump beam was "tapped off" via a partially transmitting

($T = 1\%$) mirror, and was mode matched to the reference cavity via lens L. The beam passed through the phase modulator, generating sidebands at $f_c \pm f_m$, as dictated by Eq. (3.15) and illustrated in Fig. 3.4a for $\beta = 1.1$. For practical convenience, we assume that the higher order sidebands are too weak to be of concern, and hereafter ignore them. The electric field signal exiting the phase modulator was therefore given by

$$\begin{aligned} E_{pm}(t) &= A[J_0(\beta)\cos\omega_c t + J_1(\beta)\cos(\omega_c+\omega_m)t - J_1(\beta)\cos(\omega_c-\omega_m)t] \\ &= A\left[\mathrm{Re}\left(J_0(\beta)e^{j\omega_c t} + J_1(\beta)e^{j(\omega_c+\omega_m)t} - J_1(\beta)e^{j(\omega_c-\omega_m)t}\right)\right] \end{aligned} \tag{3.20}$$

where A is the amplitude of the pump source field, and we have used the identity

$$J_n(\beta) = -J_{-n}(\beta), \quad \text{for n odd.} \tag{3.21}$$

The beam, incident on the polarizing beam splitter (PBS) and quarter-wave plate ($\lambda/4$), propagated through to the reference cavity. The two sidebands were far enough removed from the resonant frequency and much less than the linewidth of the cavity so as to be totally reflected, and were steered via the polarization rotation of the quarter-wave plate (two passes results in 90° rotation) and the PBS to the high speed photodetector and associated preamplifier (Fig. 3.6). The pump laser carrier frequency approximately matched the cavity resonance frequency and this led to a buildup of intracavity standing-wave intensity at the laser frequency. On resonance, the leakage field was basically in antiphase with the input field. The approximate cancellation of these two fields in reflection thus led to a small net reflection coefficient Γ with a phase shift θ which was strongly frequency dependent in the vicinity of the resonance [14, pg. 67]

$$\Gamma \equiv |\Gamma|e^{j\theta} = \frac{-R(1-e^{-j\delta})}{1-R^2e^{-j\delta}}. \tag{3.22}$$

R is the reflectivity of the cavity mirrors and δ is the cavity round trip phase delay

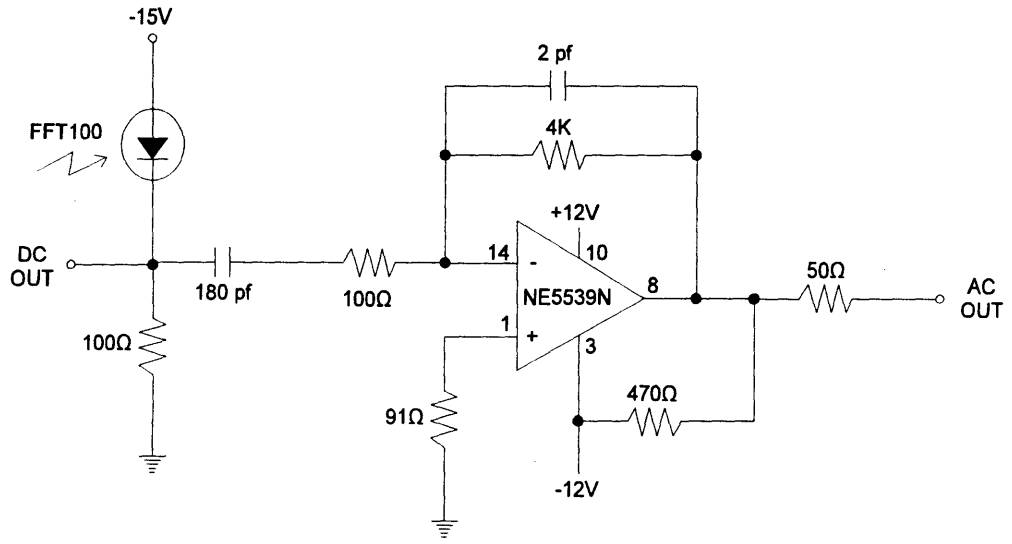

Figure 3.6: Circuit schematic for high speed photodetector preamplifier

incurred by the pump field, given by

$$\delta = \frac{2\omega l_{cav}}{c}\,, \tag{3.23}$$

where c is the speed of light in a vacuum. Note that δ is a function of both frequency and cavity length. Fig. 3.7 shows plots of the magnitude and phase spectra of the reflection coefficient. The phase information of the reflected wave provided the zero-crossing signal necessary for "locking" the pump frequency to the reference cavity resonance.

The reflected carrier field was similarly steered by the quarter-wave plate and the PBS, so that the total field incident on the photodetector was given by

$$E_{PD}(t) = A\left[\mathrm{Re}\left(J_0(\beta)\Gamma e^{j(\omega_c t+\theta)} + J_1(\beta)e^{j(\omega_c+\omega_m)t} - J_1(\beta)e^{j(\omega_c-\omega_m)t}\right)\right]. \tag{3.24}$$

The photodiode, being a square-law detector, squared this signal. Including only those terms whose frequency was measureable by the photodetector, and utilizing the

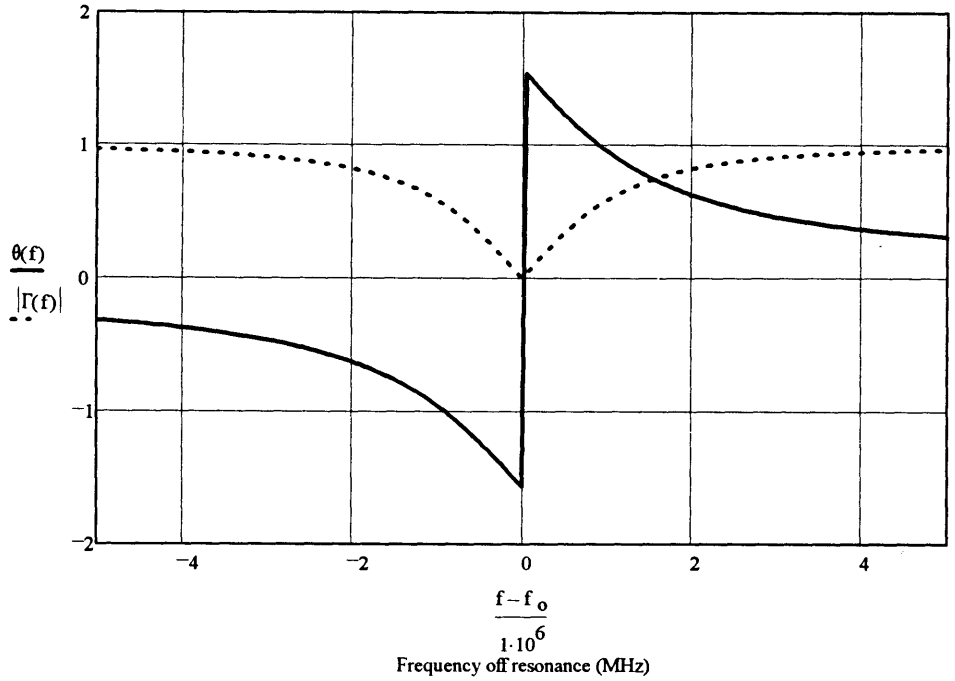

Figure 3.7: Magnitude and phase spectra of the reflection coefficient from the reference cavity.

appropriate trigonmetric identities, the signal output of the photodetector was given by

$$PD(t) = A^2\eta \left[(J_0(\beta)\Gamma)^2/2 + J_1^2(\beta) + 2\Gamma J_0(\beta)J_1(\beta)\sin\theta\sin\omega_m t\right] \tag{3.25}$$

where η is the photodetector efficieny in A/W. The photodetector amplifier passed only the AC portion of the signal (from $\sim$ 5 to 20 MHz). The signal output was then given by

$$PD_{out}(t) = 2A^2\eta G\Gamma J_0(\beta)J_1(\beta)\sin\theta\sin\omega_m t \tag{3.26}$$

where G is the amplifier gain. For the circuit utilized here, the FFT100 photodiode had a measured efficiency η of .21 A/W at λ = 531 nm, and the amplifier had a measured gain G of 30 V/V (29.5 dB) at $f_m = \omega_m/2\pi$ = 15 MHz.

From Eq. (3.26), we see that the modulation at ω_m allowed us to detect the reflected phase information θ which ultimately provided the discriminator or error signal for the servo control loop. To recover this signal, the photodetector output was

demodulated by the attentuated local oscillator/modulation signal via a Mini-Circuits Model ZLW-2 mixer, providing the intermediate frequency signal

$$IF(t) = \left(A^2\eta G\Gamma B J_0(\beta)J_1(\beta)\right)(\sin\theta - \sin\theta\cos 2\omega_m t) \tag{3.27}$$

where B is the amplitude of the attentuated local oscillator. The ZLW-2 mixer provided ~60 dB isolation from the LO input to the IF output. In order to limit the amount of 15 MHz LO signal that "bled through" to the IF output, it was preferable to keep B as low as possible. The mixer operated to within specification for an LO amplitude as low as -5 dBm.

The first stage of the error signal conditioning circuitry (Fig. 3.8) provided low-pass filtering, resulting in the dispersive error signal

$$e(t) = A^2\eta G\Gamma B J_0(\beta)J_1(\beta)\sin\theta. \tag{3.28}$$

A plot of the transmitted laser intensity and the error signal $e(t)$ as the reference cavity was tuned over the sideband structure of the phase modulated laser beam is given in Fig. 3.10. Cavity tuning was accomplished by applying a ramp voltage to the PZT actuator affixed to one of the reference cavity mirrors, which scanned the cavity length. A Burleigh Model RP-42 ramp generator was used to drive the PZT. From the figure, it is seen that the lock point for the servo was the zero in the central high slope region of the error signal, which corresponded to the pump source being precisely resonant in the reference cavity. The span of this high slope region corresponded to the cavity bandwidth of 1.4 MHz. The error signal sign was correct for servo purposes however over the full spectral interval $2f_m$ of 30 MHz.

The significance of the selection of modulation index β becomes apparent at this point. From Eq. (3.28), the amplitude of the error signal was partially dictated by the product $J_0(\beta)J_1(\beta)$. In order to assess the degree of frequency stabilization, one

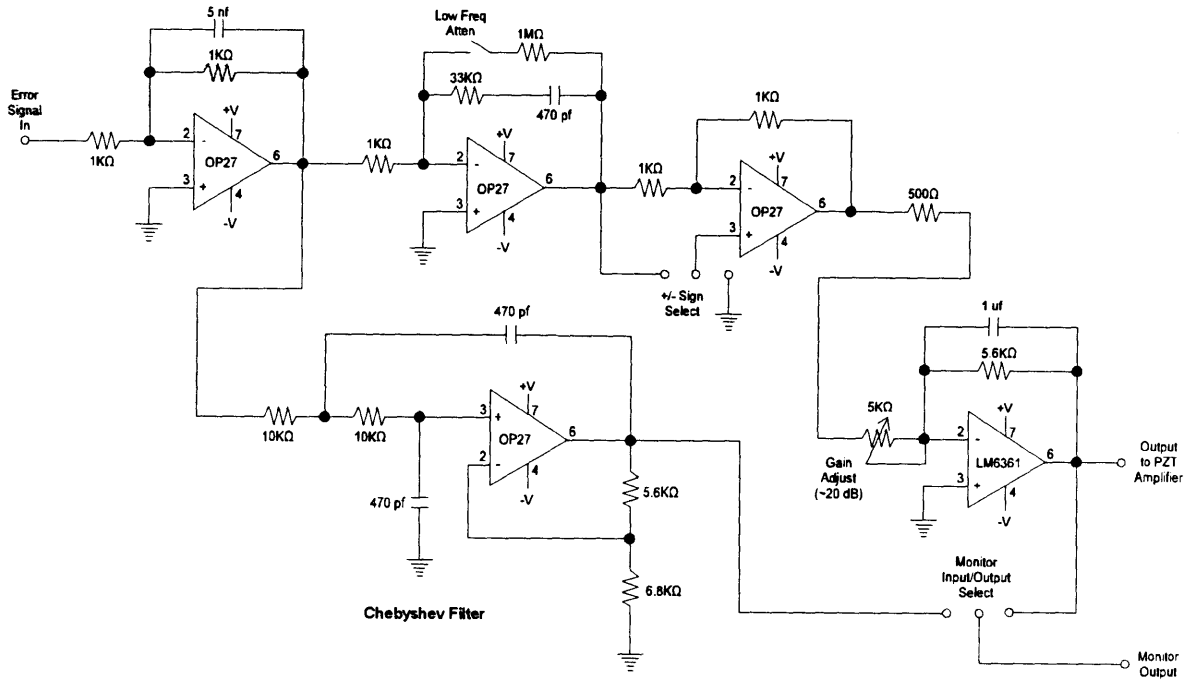

Figure 3.8: Circuit schematic for frequency servo error signal conditioning

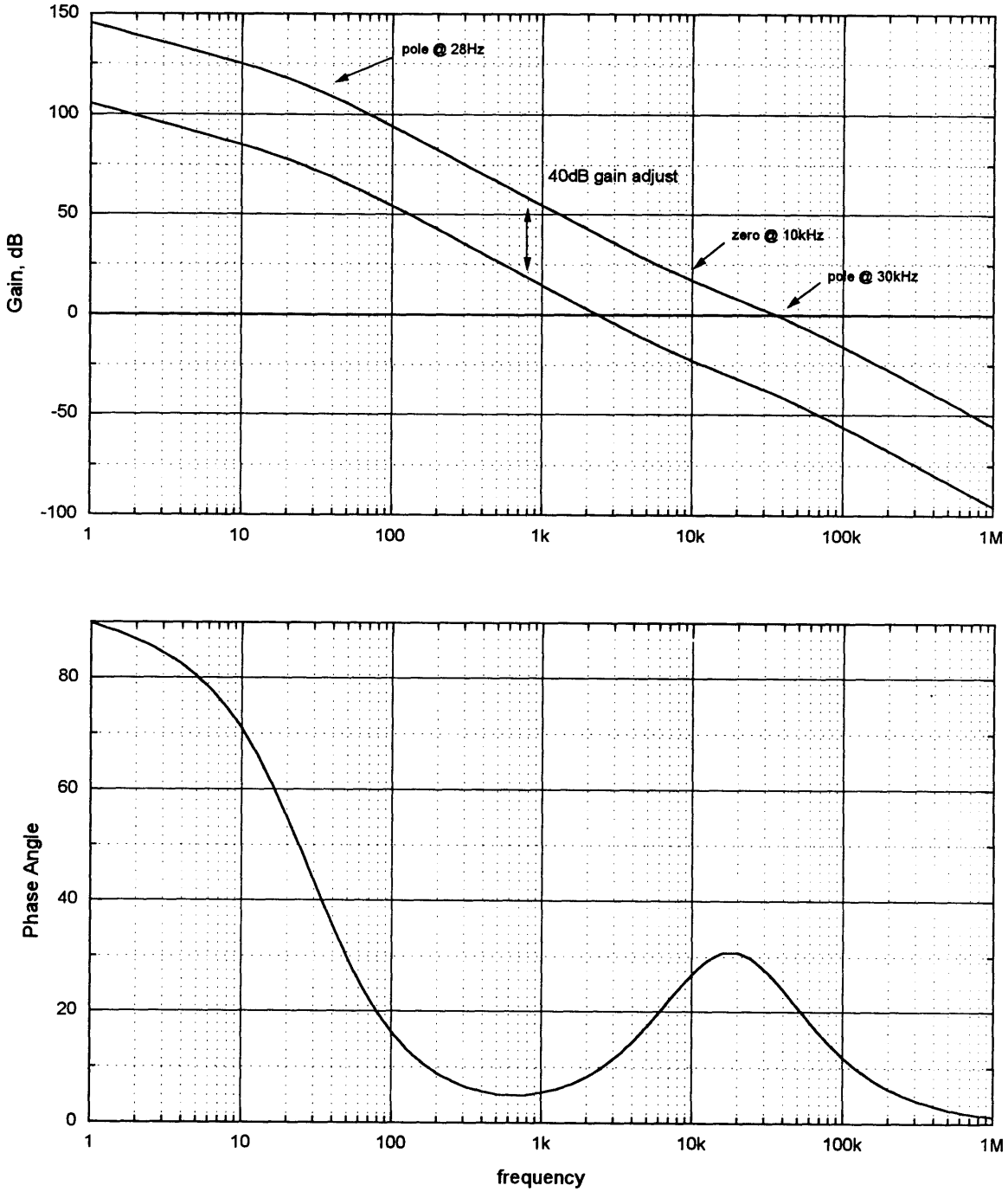

Figure 3.9: Frequency response of frequency servo electronics

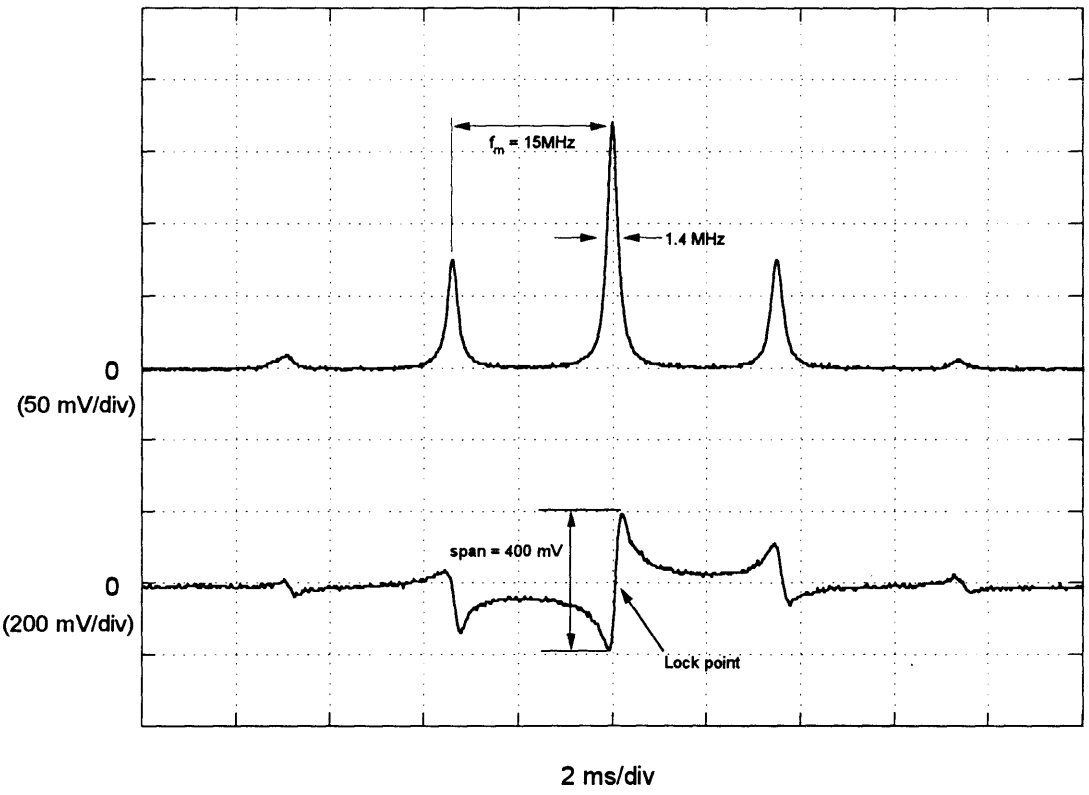

Figure 3.10: Upper trace (50 mV/div), transmitted laser intensity as reference cavity is tuned over sideband structure of phase modulated laser beam. First and second sidebands are visible symmetrically on both sides of the carrier (prominent central line). Lower trace (200 mV/div), error signal output of phase detection scheme. Lock point for servo is the zero in the central high slope region. Note that the error signal sign is correct for servo purposes over the full spectral interval $2f_m$, and that the span of the central high slope region corresponds to the cavity bandwidth of 1.4 MHz.

examines the peak to peak fluctuations of the residual zero-mean error signal when the system is locked, and then compares this peak to peak voltage to the voltage span of the error signal central region, which corresponds to the cavity bandwidth; hence, a conversion factor of MHz/V. This conversion factor was favorably minimized for the largest possible voltage span, and hence the maximum $J_0(\beta)J_1(\beta)$ product. This was achieved by selecting a $\beta = 1.1$.

The error signal conditioning electronics are shown in Fig. 3.8 and the frequency response of the circuitry is shown in Fig. 3.9. After an initial filtering stage, the error signal was again filtered by a two-pole Chebyshev filter, which removed any residual 15 MHz local oscillator signal for monitoring purposes. The error signal was additionally conditioned by integration and gain stages to provide the appropriate high gain at low frequencies. The conditioned error signal was subsequently passed to a high voltage PZT driver amplifier (Fig. 3.11), which controlled the position of the back mirror of the laser pump source. The response time of the PZT ($\tau \approx 2\mu s$) limited the frequency stabilization unity gain bandwidth to approximately 30 kHz.

The closed loop gain of the frequency stabilization system is analyzed through the aid of the block diagram of Fig. 3.12 as follows. The PZT mirror actuator has a response of 0.8 nm/V. From Table 3.1, the free spectral range (FSR) of the laser is 76 MHz, which corresponds to changing the cavity length by $\lambda/2 \approx 265$ nm. The error signal from the demodulation is evaluated, as described above, by the maximum voltage span which corresponds to the reference cavity bandwidth of 1.4 MHz. For a pump source operating power of ~120 mW, the span of the central sloping region was ~400 mV peak-to-peak. The signal in turn is processed by the electronics whose frequency response is shown in Fig. 3.9, and then amplified by the PZT high voltage driver of Fig. 3.11, which has a 20 dB adjustable gain from 9 to 100 V/V. Using the maximum gain available from the adjustable amplifiers, we then have, for the

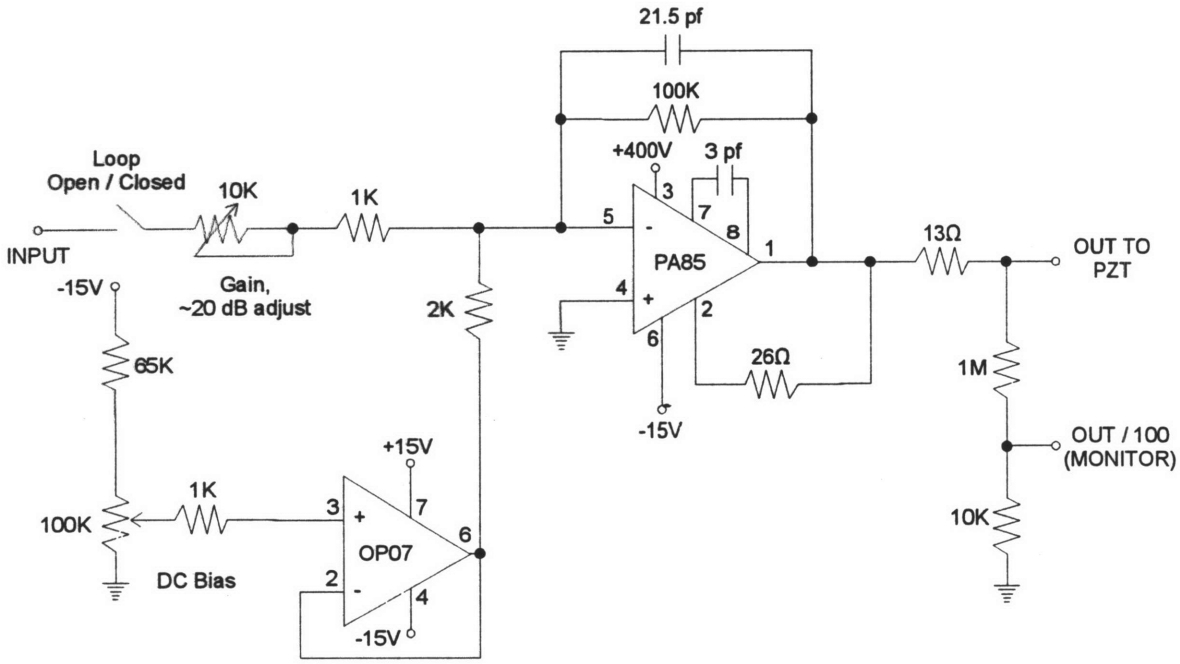

Figure 3.11: Circuit schematic of PZT high voltage driver/amplifier for frequency stabilization loop.

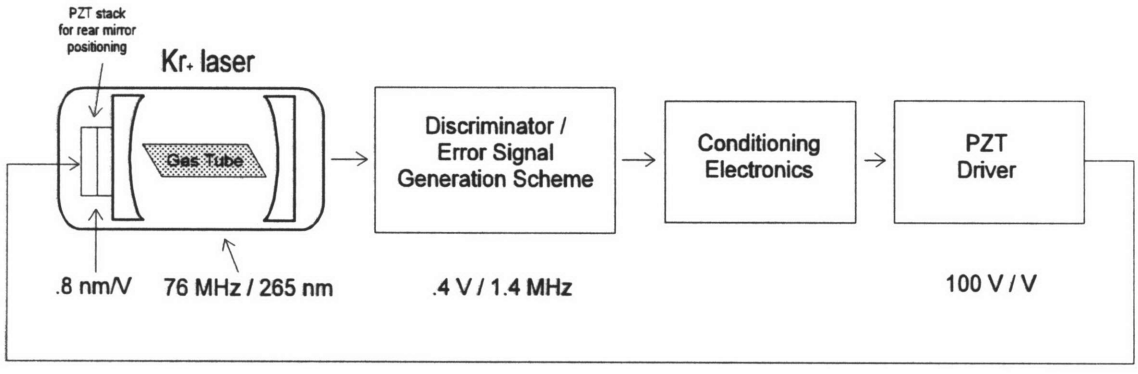

Figure 3.12: Block diagram of frequency stabilization system for determination of closed loop response.

frequency stabilization loop signal chain

$$\frac{.8 \text{ nm}}{\text{V}} \times \frac{76 \text{ MHz}}{265 \text{ nm}} \times \frac{.4 \text{ V}}{1.4 \text{ MHz}} \times \text{cond. elec. (V/V)} \times \frac{100 \text{ V}}{\text{V}}$$
$$\approx 6.5 \times \text{cond. elec.} \qquad (3.29)$$

Therefore, the spectra given in Fig. 3.9 gives a reasonable approximation of the closed loop system response, where the magnitude spectrum may be decreased by 40 dB (20 dB adjustment in the error signal conditioning electronics, 20 dB in the PZT driver electronics).

In order to lock the laser frequency to the reference cavity resonance, with the loop "open" the DC bias for the PZT on the laser rear mirror was set to approximately one-half of its span (~ 400 V max, set to 200 V). The DC bias for the PZT stabilizing the reference cavity was manually scanned until strong transmission was seen, indicating the cavity resonance was close to the laser frequency.

The DC bias for the reference cavity supplied by the Burleigh ramp generator was not sufficiently stable (peak-to-peak noise of 40 mV), so that a low pass filter was required with a -3 dB frequency of $f = .8$ Hz, which reduced the low frequency noise to less than 800 μV peak-to-peak. The accuracy of the reference cavity resonance was then obtained, using the free spectral range (FSR) from Table 3.2:

$$\frac{.8 \text{ nm}}{\text{V}} \times \frac{724.6 \text{ MHz}}{265 \text{ nm}} \times 800 \ \mu\text{V}$$
$$= 1.75 \text{ kHz}$$
$$= \pm 875 \text{ Hz}. \qquad (3.30)$$

The loop was then "closed", and the system locked to the cavity resonance. This was ascertained by monitoring the error signal from the conditioning electronics as well as the DC voltage level that was used to bias the laser rear mirror PZT; the latter was fine-tuned during locking to maintain the half-span (200 V) bias. The

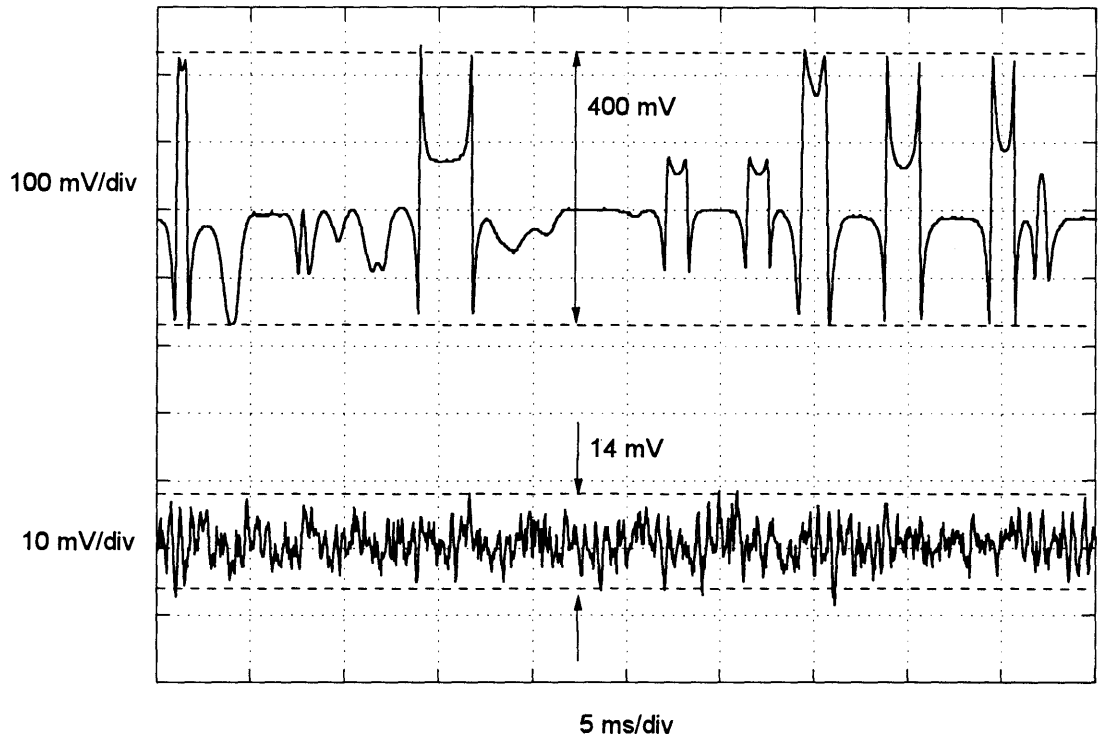

Figure 3.13: Frequency servo error signal, top trace (100 mV/div) unlocked, bottom trace (10 mV/div) locked. Note in the unlocked state that the peak-to-peak span of the error signal is ~400 mV, and that the frequency jitter is well beyond the reference cavity bandwidth of 1.4 MHz. In the locked state, the residual error signal peak-to-peak fluctuations are on the order of 14 mV.

gain of the loop, via the error signal conditioning electronics or the PZT driver, was adjusted to achieve the minimum peak-to-peak residual error signal fluctuations, which were observed to be on the order of 14 mV. Fig. 3.13 shows the error signal under both the unlocked and locked conditions. Using the conversion factor from Eq. (3.29), we assessed the stability of the locked laser frequency to have been

$$\begin{aligned} 14 \text{ mV} \times \frac{1.4 \text{ MHz}}{400 \text{ mV}} \quad + \quad \text{ref. cav. error} \quad &\approx 50 \text{ kHz} \\ &= \pm 25 \text{ kHz}. \end{aligned} \tag{3.31}$$

The frequency servo control was quite robust, maintaining a locked state for several

minutes, often times up to a half-hour or more. Compared to the estimated unlocked frequency jitter of $\geq \pm 20$ MHz, this was a substantial improvement that subsequently allowed OPO cavity stabilization and intensity correlation measurements with greater ease and accuracy than possible in the unlocked state.

3.5 Excess Pump Noise Spectrum

The effect of excess pump noise above the shot noise limit, especially in the low frequency range ($<\sim 1$ MHz), has been shown to have a deleterious effect on the OPO twin beam output intensity correlation spectrum [39]. This effect is strongly dependent on cavity loss mismatches between the orthogonal signal and idler beams, which is a natural consequence of the crystal birefringence, absorption, beam walk-off and optical coatings for the cavity mirrors used in the OPO. We will describe these losses in detail in Ch. 4. Here, we characterize the excess pump noise spectrum for typical operating conditions and determine the excess pump noise factor $h(f)$.

The excess pump noise spectrum was monitored at the input port of the OPO for a pump power of ~ 160 mW. A high speed photodiode and preamplifier (Fig. 3.14) with a flat frequency response through ~ 8 MHz was utilized to obtain both a white light spectrum and the pump spectrum for equivalent DC photocurrents (average intensities). Neutral density filters were also used to insure that neither the photodetector nor the amplifier were saturated (the detected optical power was on the order of 10 mW). The pump noise and shot noise levels for the equivalent full 160 mW power were then extracted from the raw data, keeping in mind that for a given neutral density filter of transmission T, the excess pump noise power upon attenuation went as $1/T^2$, whereas the attenuated shot noise power went as $1/T$. After subtracting the electronic noise due to the photodetector circuitry, the excess

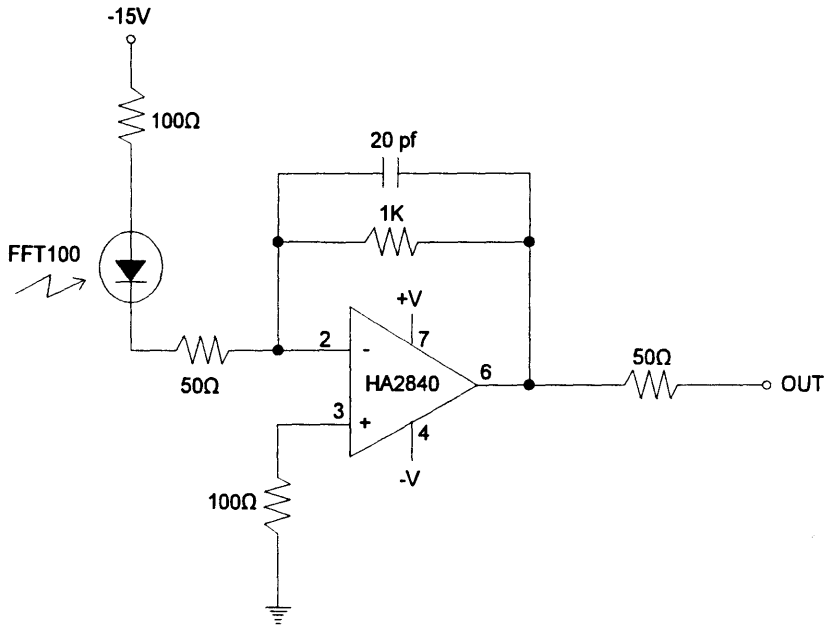

Figure 3.14: Photodetector amplifier circuit for pump noise spectrum measurements.

pump noise factor for the full pump power was determined by

$$h(f) \equiv \frac{\text{excess pump noise power}}{\text{shot noise power}}. \tag{3.32}$$

The pump noise factor $h(f) = 1$ for a shot noise limited pump. Fig. 3.15 shows two spectra samples of the excess pump noise factor, and their average. The first measurement was performed after the laser was operating for approximately an hour, and the second measurement was taken after the laser had been operating for several hours over the course of a day. While the two measurements differed slightly in the range of ~2-4 MHz, both measurements became shot noise limited at ~5 MHz.

3.6 Summary

In this chapter, we have discussed the pump laser system including the laser source, the intensity and frequency stabilization servos and the excess pump noise spectrum.

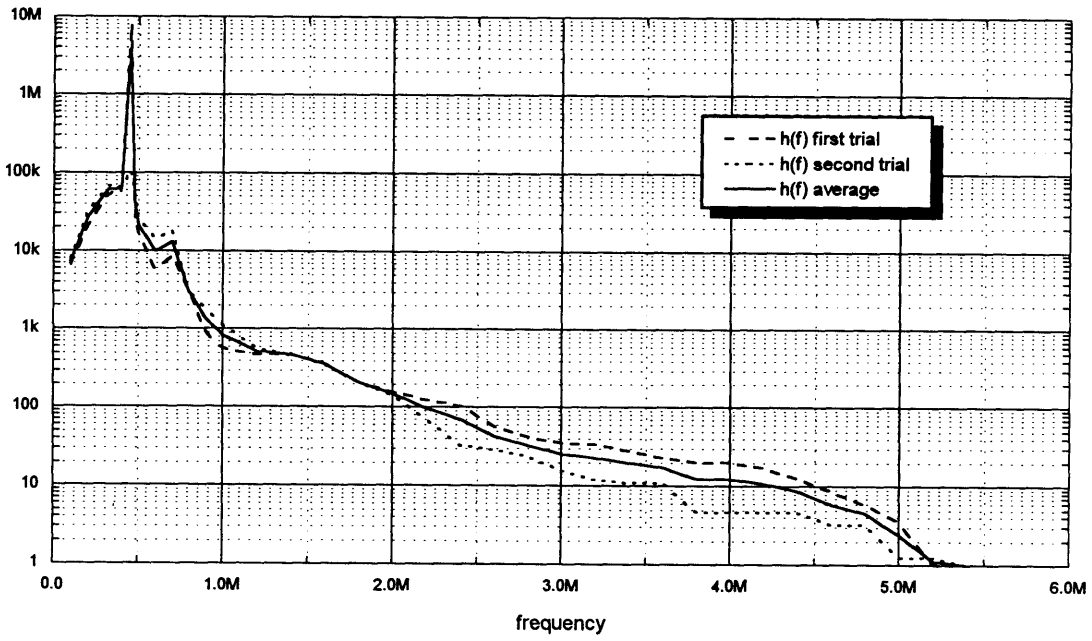

Figure 3.15: Excess pump noise factor, $h(f)$

Table 3.3 summarizes the relevant operating properties of the pump laser field at the OPO input port.

Wavelength	Single frequency @ 530.9 nm
Maximum power at OPO input	160 mW
Intensity Noise	0.5%
Frequency Jitter	$\pm$25 kHz
Shot Noise Limited Frequency	$\sim$5 MHz

Table 3.3: Summary of pump laser operating properties at the input port of the OPO.

Chapter 4

OPO Cavity Design and Characterization

4.1 Introduction

The two major OPO design criteria were cavity length stability and low cavity losses. The stringent requirement of cavity length stability was the result of the doubly-resonant condition, in which both the signal and idler fields were simultaneously resonant with the optical cavity. The goal of low cavity losses corresponded to a low oscillation threshold and a high output intensity correlation. These issues were first discussed in Ch. 2, where the single-pass pump power threshold (in watts) for the doubly-resonant OPO was estimated for degenerate outputs as (Eq. 2.44)

$$P_{th}(\omega_p) = \frac{\pi \kappa_s \kappa_i n_p n_s \epsilon_o c^4}{8 l \omega_o^3 d_{eff}^2 \overline{h}(B,\xi)} \tag{4.1}$$

and a simplified model of the intensity correlation spectrum normalized to its associated shot noise level, which assumed identical losses for both signal and idler fields, was given by [15]

$$S_{ID}(f) = 1 - \left[\frac{\eta \left(1 - \frac{\mu}{T+\mu}\right)}{1 + \frac{f^2}{\Delta f^2}} \right]. \tag{4.2}$$

In Eq. (4.1) the parameters of interest regarding losses are $\kappa_{s,i}$ which are the effective round-trip field losses in the cavity for the signal and idler, respectively. These are equivalent to the quantity $(T + \mu)$ in Eq. (4.2), where the losses are distinguished between the output coupling loss T and all other extraneous losses μ, i.e. $\kappa = T + \mu$. Minimizing these total losses has the effect of simultaneously minimizing threshold and maximizing correlation.

In this chapter, we will look at the possible design configurations for the OPO cavity and justify the final selection based on cavity stability. The techniques for cavity stabilization will be presented in Ch. 5. Based on this cavity selection, we will look at the OPO physical construction in terms of its constituent parts, and report a complete "optical loss accounting" for the final design. The nonlinear crystal will be given particular attention for its contribution to losses and its role in determining the oscillation threshold in Eq. (4.1) through the additional parameters of refractive indices, nonlinear coefficient d_{eff} and reduction factor $\overline{h}(B, \xi)$. From the total loss accounting which additionally includes the cavity end mirrors, reasonable estimates for the single-pass oscillation threshold and intensity correlation will be made.

Finally, the particular novelty of the OPO design employed for the experiment will be presented, which was a four-piece (three mirror) triply-resonant system with a substantial pump cavity finesse. This design, while placing additional requirements on cavity length stability, was motivated by the need to reduce the oscillation threshold power of the OPO in order to avoid potential power limitations of the pump system. As a stepping stone to the final cavity design, we will also discuss the effect of a double-pass pump on the oscillation threshold and how modeling this intermediate solution as a weak pump resonance leads to a useful qualitative description of the triply-resonant system.

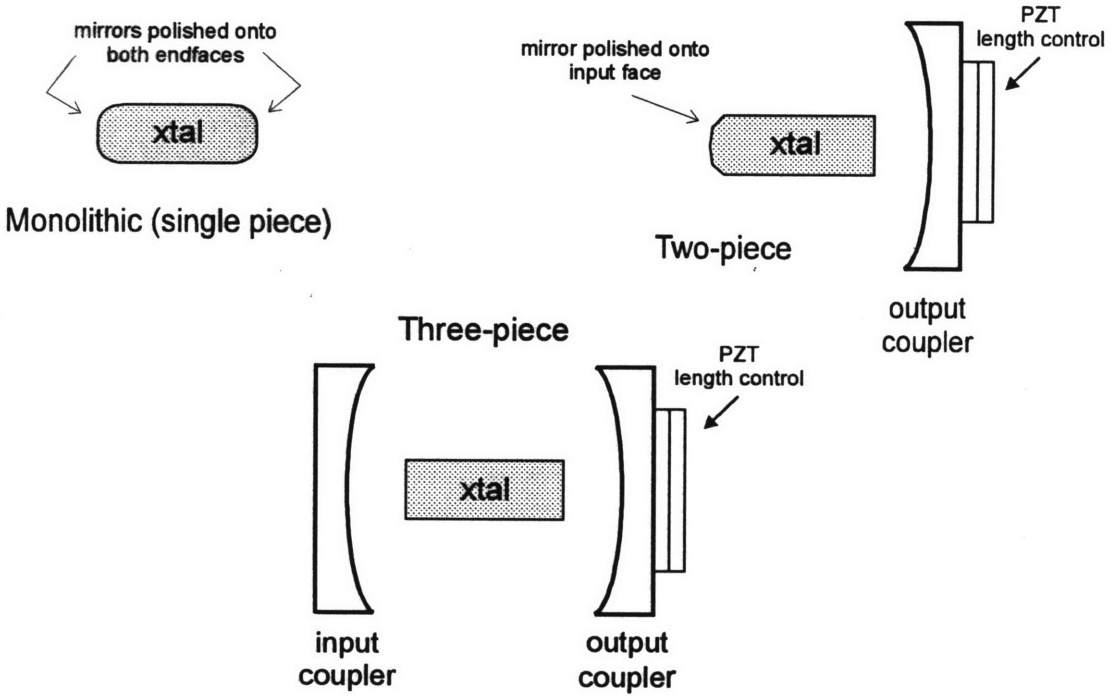

Figure 4.1: OPO Cavity Configurations.

4.2 Cavity Structure Alternatives

Figure 4.1 shows three basic types of OPO configurations: monolithic, 2-element and 3-element. They all share the same simple concept: a nonlinear crystal placed between two reflecting surfaces. They differ in their implementation of the two cavity mirrors. A monolithic cavity is the simplest possible design, having both input and output mirrors polished onto the crystal, and it requires no mechanical stabilization. Although compact and low-loss, complex and costly fabrication as well as difficulty in alignment render this cavity configuration intractable for practical use.

In a multi-element design, one or both of the reflective surfaces of the crystal are replaced with mirrors, and the corresponding crystal surfaces are polished flat and anti-reflective (AR) coated to minimize reflective losses. A two-element OPO consists of a crystal and one mirror, and a three-element design consists of a crystal

and two mirrors.

The three-element OPO is the easiest to construct and most flexible in changing cavity parameters. One of the external mirrors is mounted on piezoelectric transducer (PZT) stacks to provide cavity length control. The primary potential drawback in the three-element OPO is its greater loss and hence higher threshold due to its two air-crystal interfaces.

A two-element OPO is a compromise between the monolithic and the three-element design. It is easier to construct and more flexible than the monolithic design in changing cavity parameters after fabrication. Additionally, it has lower losses than the three-piece cavity (the number of times the beam passes through the crystal faces in one round trip is reduced from four for the three-piece to two), and therefore a lower threshold. However, both multi-element designs are inherently more susceptible to environmental perturbations than the monolithic design, hence the actual cavity construction becomes a concern; it is necessary to eliminate any spring-loaded mount from the design and the cavity elements should be fixed in position by attaching them rigidly to a common platform.

In a previous experiment [28], a two-piece OPO design was chosen for low loss considerations. Stabilization of the cavity proved to be difficult however, due to mounting construction which included a tilt mount for the output coupler to aid alignment. In light of this, the inherently more stable mounting design of the three-piece cavity rendered it an attractive alternative, albeit at the expense of higher losses, and this was a suggested approach for future work. It was hence the design selection for this research.

4.3 The OPO Cavity Design

Fig. 4.2 shows the detailed construction of the OPO cavity. A Lees cavity structure was used which had fixed end-plates in which to mount the input and output mirror

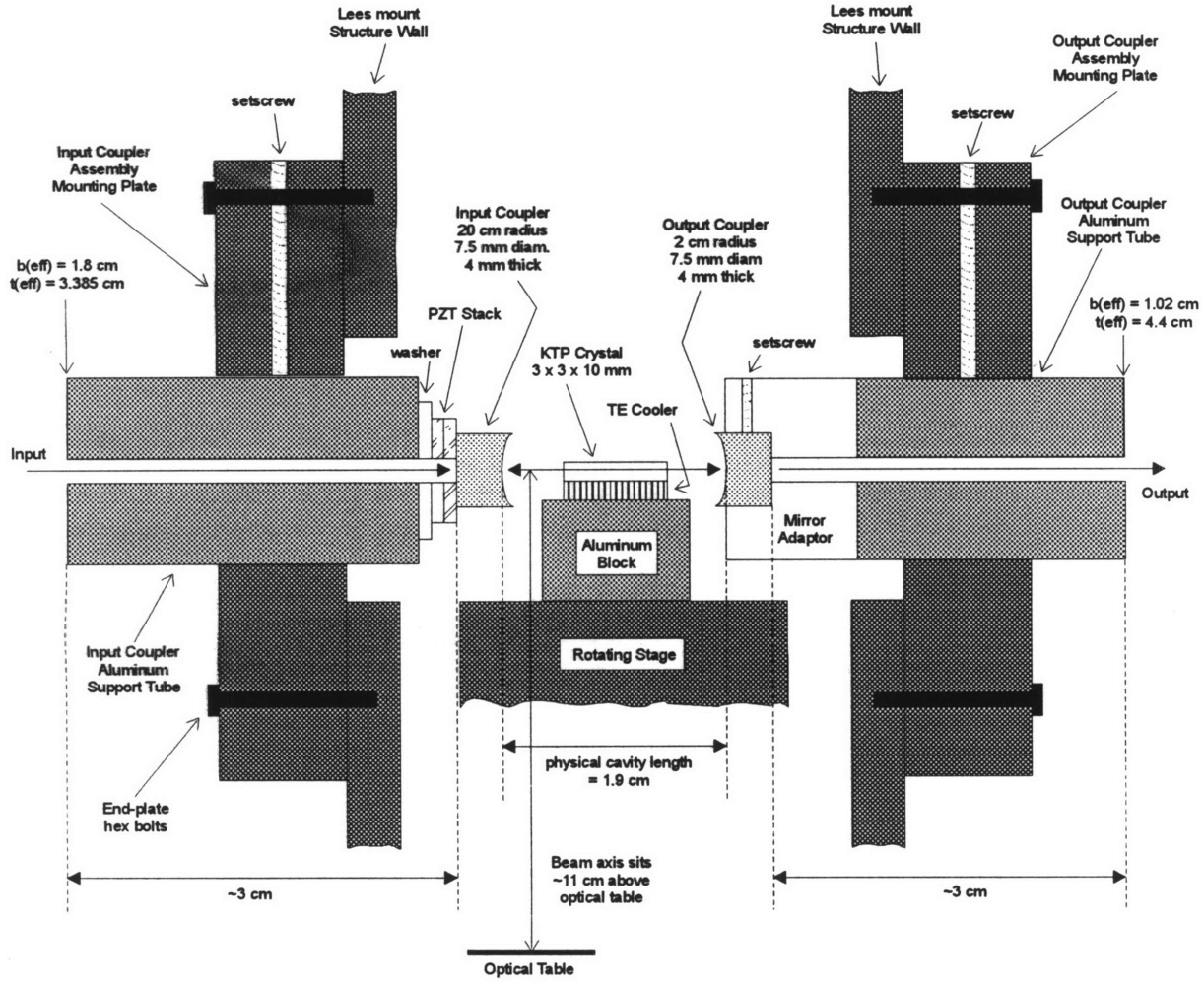

Figure 4.2: Detail of OPO cavity construction (not to scale).

assemblies. Mirror positioning was accomplished through gross movements of the end-plates which were tightened in place with hex-head bolts; no axial adjustments of the mirrors were provided so that once mounted, positioned and affixed via setscrews, the mirror assemblies provided a high degree of mechanical stability. The cavity length was adjustable via setscrews by horizontal positioning of the mirror assemblies.

The only moving portion of the mount was a rotational stage in the center for mounting of the nonlinear crystal. This provided some degree of freedom in cavity alignment and angle tuning, but was used sparingly; most of the cavity alignment was performed as the cavity was assembled, and subsequently fine tuned with external control of the pump beam direction. Hence, once assembled, the cavity required no further adjustment, was sturdy and mechanically stable.

The cavity mirrors were supplied by Research Electro-Optics, Inc. The input coupler had a radius of curvature of 20 cm on one side and was flat on the other. The curved surface was specially coated for high reflection at $\lambda = 1064$ nm and high transmission at $\lambda = 532$ nm. The flat surface was anti-reflection (AR) coated for $\lambda = 532$ nm. The input coupler was epoxied to a stack of two piezoelectric transducers (PZT) supplied by Piezokinetics, Inc. (model #PK1-500, 0.5" O.D., 0.225" I.D., 0.05" thick), which allowed for voltage controlled movement of the mirror position and hence adjustment of the cavity length. Each PZT had a piezoelectric constant $d_{33} = 400$ pm/V, so for the stack of two this resulted in $\sim$0.8 nm movement for each volt applied.

The output coupler had a radius of curvature of 2 cm on one side and was flat on the other. The curved surface was specially coated for high reflection at $\lambda = 532$ nm and a transmission of $T = 2.7\%$ at $\lambda = 1064$ nm. This mirror also served as an end mirror for the pump resonance cavity, as will be explained later.

The nonlinear crystal was affixed with two-sided tape to a thermal-electric (TE) cooler, which was in turn epoxied to an aluminum block on the rotating stage of the mount, such that the horizontal axis of the crystal sat at $\sim$11 cm above the

surface of the optical table. This was approximately the location of the pump beam at the input to the cavity. The only vertical beam adjustment was through external mirrors for the pump beam, requiring that the aluminum block be carefully machined so that the crystal was at the appropriate height within the OPO assembly. The TE cooler provided a means of thermally adjusting the refractive indices and hence the phase matching conditions of the crystal. Specific properties of the crystal will be addressed in the following section, as well as the choice of cavity length.

4.3.1 The Nonlinear Crystal

Potassium Titanyl Phosphate (KTP) was chosen as the nonlinear medium in this study because of its type-II phase matching (see App. B), large nonlinear coefficients, low absorption, large temperature and angular tolerances, and good optical quality. The orthogonality of the signal and idler polarizations as a result of type-II phase matching greatly simplified the detection scheme as will be explained in Ch. 5, where the two beams were separated by a polarizing beam splitter. The signal and idler designations may be arbitrarily assigned to the extraordinary and ordinary output polarizations. The crystal was placed in the OPO cavity such that its axis was vertically oriented; hence, the pump input was horizontally (p) polarized, the extraordinary output was vertically (s) polarized and the ordinary output was horizontally (p) polarized.

Since KTP is a biaxial crystal, the signal and idler waves see different refractive indices in the type-II phase matching geometry. The Sellmeir equations for KTP (empirical equations used to determine the indices of refraction for the three crystal axes) are given by [1]

$$n_x^2(\lambda) = 2.1146 + \frac{.89188}{1 - \left(\frac{.20861}{\lambda}\right)^2} - .01320\lambda^2$$

$$n_y^2(\lambda) = 2.1518 + \frac{.87862}{1 - \left(\frac{.21801}{\lambda}\right)^2} - .01327\lambda^2$$

$$n_z^2(\lambda) = 2.3136 + \frac{1.00012}{1 - \left(\frac{.23831}{\lambda}\right)^2} - .01679\lambda^2. \tag{4.3}$$

Table 4.1 gives the results for the refractive indices at the particular wavelengths of interest. Fig. 4.3 shows the type-II phase matching arrangement and the refractive indices of KTP as a function of wavelength.

Wavelength	n_x	n_y	n_z
1.064 μm	1.7377	1.7453	1.8297
532 nm	1.7780	1.7886	1.8887

Table 4.1: Refractive indices of KTP.

A phenomenon called *walk-off* results from the differences in the refractive indices. When a beam walks-off, the direction of propagation of the phase velocity is not collinear with the direction of energy propagation; in essence, there is an imperfect overlap among the three interacting fields in the nonlinear medium. It has been shown by Boyd and Kleinmann [6] that such walk-off is a function of the degree of focusing of the respective Gaussian beams in the crystal and reduces the single pass conversion efficiency by a factor of $\overline{h}(B,\xi)$, where $\xi = l/b$ is the focusing parameter for the confocal parameter $b = \frac{2\pi n\omega^2}{\lambda}$ (Sec. 2.5), and B is the double refraction parameter defined as

$$B = \frac{\rho}{2}\sqrt{\frac{lk_p}{2}}, \tag{4.4}$$

where ρ is the walk-off angle, l is the physical crystal length and $k_p = \frac{2\pi n_p}{\lambda_p}$ is the pump wave number. For a given B and ξ, Boyd and Kleinmann have plotted an empirical set of graphs from which the reduction factor can be obtained. However, in a "near-field" approximation where the crystal length l is less than the confocal parameter b, walk-off can be considered negligible and the reduction factor may be

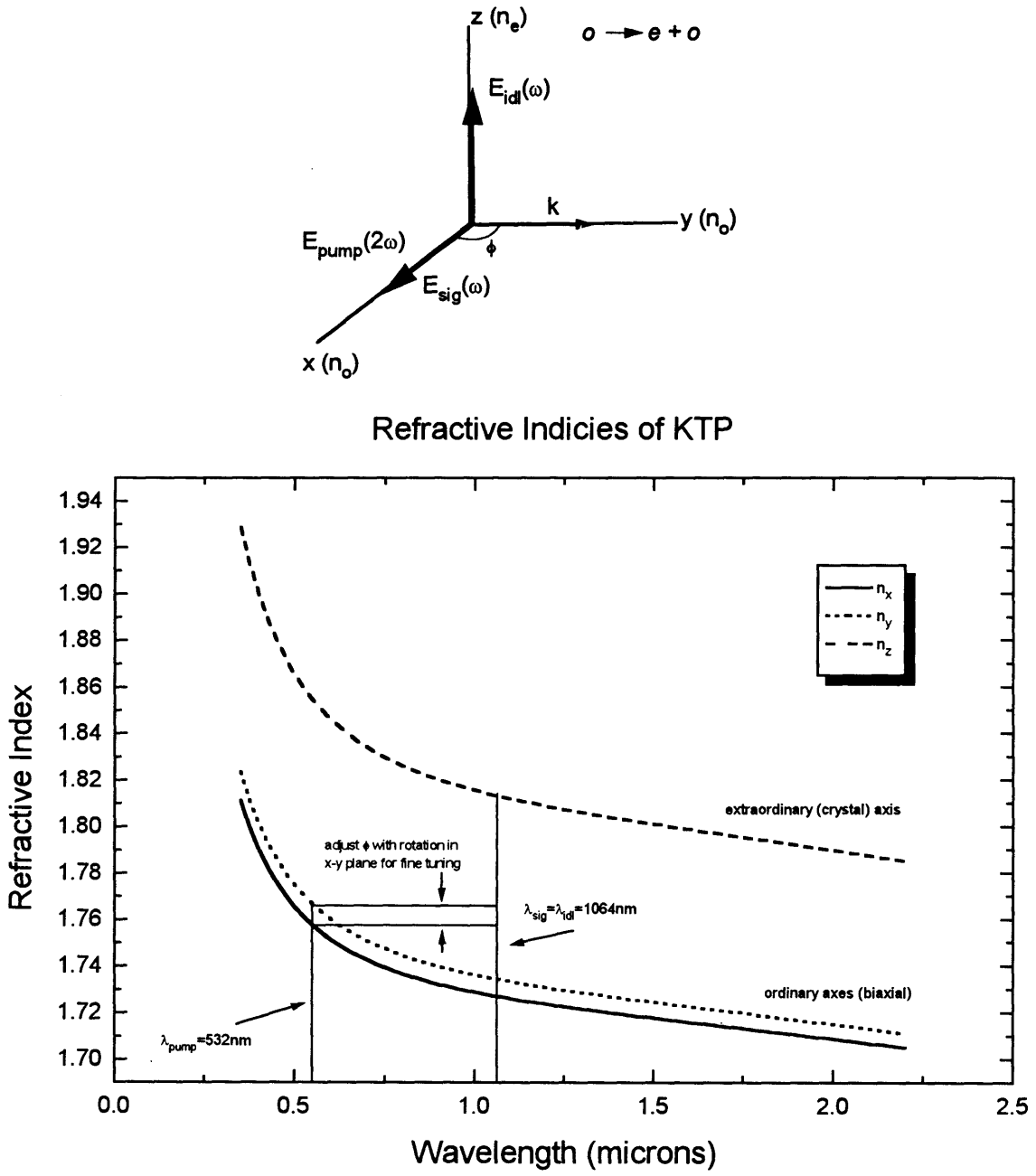

Figure 4.3: KTP is ideally suited for type-II 90° phase matching in second harmonic generation from 1064nm to 532nm (degenerate parametric down conversion is essentially the "inverse" process). Fine angle tuning of phase matching can still be accomplished as a result of the crystal being biaxial; rotation around the crystal axes (in the x-y plane) by an angle ϕ provides subtle adjustments of the pump and signal (as shown above) refractive indices.

approximated by [19]

$$\overline{h}(B,\xi) \approx \xi = l/b, \quad \text{for } \xi < 0.4. \tag{4.5}$$

To make use of this approximation, given a crystal length of 1 cm, the OPO cavity was designed to have a confocal parameter b of approximately 3.5 cm, resulting in $\xi \approx .3$. A MATLAB simulation of the Gaussian beam propagation in the cavity (Appendix C) provided a relationship between the cavity length and the resulting confocal parameter. From this relationship, it was determined that a total physical cavity length, including the crystal, of 1.9 cm resulted in a confocal parameter $b = 3.22$ cm. From Eq. (4.5), this results in a reduction factor $\overline{h}(B,\xi) \approx .31$.

KTP has an orthorhombic crystal structure with the following nonlinear coefficients (in pm/V) [1]:

$$\begin{aligned} d_{31} &= 2.45 \\ d_{32} &= 4.35 \\ d_{33} &= 16.9 \\ d_{24} &= 3.64 \\ d_{15} &= 1.91 \end{aligned} \tag{4.6}$$

For type-II phase matching, it is shown in App. B that the nonlinear coefficient d_{eff} is given by

$$d_{eff} = -[d_{15}\cos^2(\phi) + d_{24}\sin^2(\phi)]\sin(\theta_p). \tag{4.7}$$

The crystal for this study was supplied by Litton-Airtron, Inc. It was a hydrothermally grown crystal, 3 × 3 × 10 mm in dimension, with anti-reflection coatings on each end-face. The crystal was cut at $\theta_p = 90°$ and $\phi = 23.18°$, which resulted in a d_{eff} from Eqs. (4.6) and (4.7) of 2.18 pm/V.

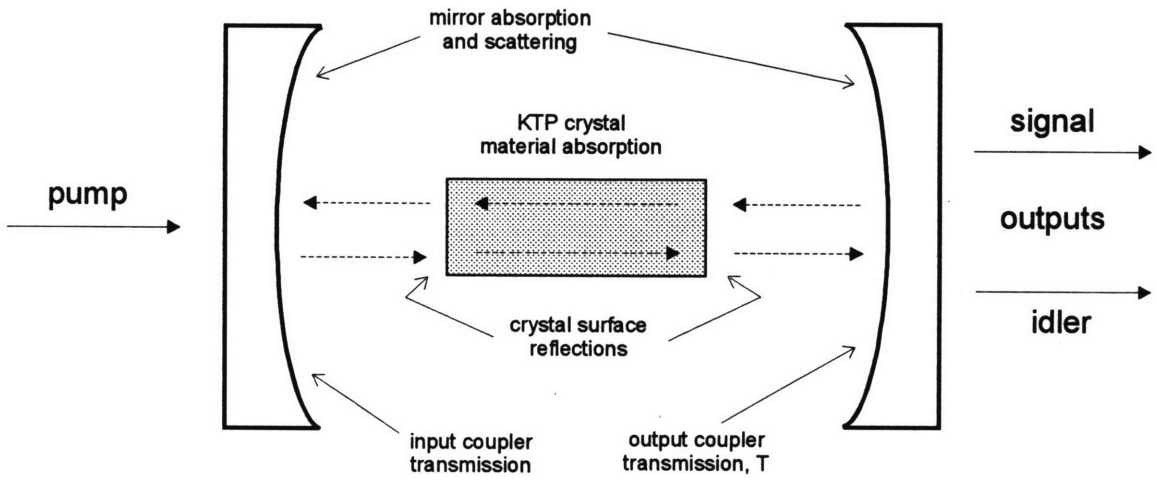

Figure 4.4: Sources of loss in an OPO cavity.

4.4 Optical Loss Accounting

Fig. 4.4 shows the potential sources of loss in the OPO. Three techniques were used to assess the optical losses in the OPO cavity: direct measurement of optical components prior to the assembly of the OPO, and transmission and reflection measurements through and from the cavity respectively after assembly. This provided a complete optical loss accounting of the OPO system and enabled estimation of the oscillation threshold and the output intensity correlation spectrum. An Amoco Nd:Yag laser with an operating wavelength $\lambda = 1.06$ μm and a linearly polarized output was used as the pump source for all loss measurements.

The sources of loss are broken down as follows:

T_m $\equiv$ lumped mirror transmission loss (input + output)

A_m $\equiv$ lumped mirror absorption loss

$A_x \equiv$ crystal absorption loss, per pass

$R_x \equiv$ crystal surface reflection loss, per surface

so that the total round-trip loss for either polarization, i.e. the signal or idler field loss $\kappa_{s,i}$ is given by

$$\kappa_{s,i} = T_m + A_m + 2A_x + 4R_x \tag{4.8}$$

where we account for two passes through the crystal per round-trip, which includes two absorption losses and four crystal surface reflections.

4.4.1 Direct Component Measurements

The transmission of the input and output couplers were easily measured by placing each mirror in the beam path of the laser which was focused onto a photodetector. A $\lambda/2$ plate was used to rotate the polarization of the laser output to examine qualitatively the effect of polarization on the mirror transmission. The ratio of the photodetector output with the mirror in the beam path versus no mirror in the path provided the transmission factor. Several measurements were taken for each mirror, and the alignment of the beam on the photodetector was repeatedly verified. As expected, laser polarization had no distinguishable effect on the mirror transmissions. The average transmission of the output coupler was 2.6857% and that of the input coupler was .0168%, giving a lumped mirror transmission $T_m = 2.7025\%$.

The quality of the anti-reflection coatings on each surface of the crystal was measured for both polarizations by observing the reflections from the crystal faces. The procedure was as follows: the output of the laser was measured by the photodetector through a filter of known attenuation (since the reflection coefficients of the crystal faces are quite small, laser power far in excess of what is necessary to saturate the photodiodes is required). This same beam was directed onto the crystal face at a slight angle from normal incidence, and the reflected power was measured. It was de-

sirable to keep the angle of incidence small as large angles degraded the measurement accuracy. The reflection measurement was then compared to the attenuated laser measurement, and the ratio of reflected power to full incident power was determined utilizing the attenuation factor.

Two reflections were to be expected, one from each face of the crystal. Hence, at small angles of incidence the reflected power was approximately twice that of the reflections at slightly higher angles of incidence, where two distinct reflections could indeed be discerned. This was observed at an angle of incidence of $\sim 10°$. Since this was a rather large value of incident angle, it was likely that the reflection coefficients for normal incidence were actually slightly smaller than those measured here. Several measurements were taken, with the average results:

$$\begin{aligned} R_x &= .08\% \text{ per surface, extraordinary (s) polarization} \\ &= .13\% \text{ per surface, ordinary (p) polarization.} \end{aligned}$$

For any of the optical components, we have the conservation relationship

$$T + R + A = 1.$$

Therefore, by measuring the transmission through the crystal, we can determine the single-pass crystal absorption A_x, given by $1 - T_x - 2R_x$. This was done in the same manner as the reflection measurements; however, because of the high expected transmission through the crystal, the laser attenuation via a filter was used for both the control and transmission measurements, making it easier to arrive at the desired transmission ratio. The average transmission measurements through the crystal were

$$\begin{aligned} T_x &= 99.81\% \text{ extraordinary (s) polarization} \\ &= 99.71\% \text{ ordinary (p) polarization} \end{aligned}$$

that yields

$$A_x = 1 - T_x - 2R_x = .03\%$$

for both polarizations. Note that there can be significant uncertainty in A_x which is determined by the uncertainty in the T_x measurements.

4.4.2 Cavity Transmission Measurements

In order to determine the mirror absorption and scattering losses and verify the crystal absorption losses, the transmission properties of the Fabry-Perot cavity [14] were utilized. The basic theory and terminology associated with a Fabry-Perot resonator were presented in Sec. 2.4. Here, we were particularly interested in measuring the finesse of both the OPO cavity containing the nonlinear crystal, and the same cavity without the crystal.

It has been shown that the finesse F of a cavity with low losses (high mirror reflectivities) may be approximated by [28]

$$F \approx \frac{2\pi}{\kappa} \tag{4.9}$$

where κ is the total round-trip loss of the resonator. By knowing the lumped transmission T_m of the cavity mirrors, we may extract the lumped mirror absorption A_m by measuring the finesse of the empty cavity, where $\kappa = T_m + A_m$. Similarly, by knowing T_m, A_m and R_x, we may extract the crystal absorption A_x by measuring the finesse of the cavity containing the crystal, where κ is then given by Eq. (4.8).

For the finesse measurements, the infrared laser source was mode matched to the optical cavity. The output of the cavity was incident on a photodetector/amplifier (YAG100). The optical cavity length was scanned by applying a ramp voltage in the form of a triangle or sawtooth wave with an amplitude of several hundred volts across

the PZT stack attached to the input coupler (recall that the response of the PZT is ~.8 nm/V). The length change had to be enough to scan at least one free spectral range ($FSR = \lambda/2$), which in this case equals to 532 nm; this implied a PZT ramp voltage on the order of 670 V. The frequency of the ramp input was ~30 Hz. Faster scan rates skewed the output waveform indicating that the PZT could not move the mass of the mirror quickly enough. The detected output waveform from the photodetector/amplifier was recorded on a LeCroy 9400 digital oscilloscope (Fig 4.5). The FSR and the full width at half maximum (FWHM) of the transmission peaks was then measured from the oscilloscope traces, and the finesse F was given by

$$F = \frac{FSR}{FWHM}.$$

In practice, due primarily to the nonlinearity of the PZT, the FWHM of each of the two peaks in the FSR were not equal. An average of the two was taken for each measurement. Also, due to various mechanical noise sources, the values of the FSR and average FWHM varied from measurement to measurement for the same cavity, resulting in finesse measurements that fluctuated by ~10%.

For the empty cavity, finesse measurements were found to be insensitive to polarization, as expected. The average finesse from a dozen or so cavity transmission measurements was $F \approx 227$, which from Eq. (4.9) implied a total round-trip loss $\kappa = 2.768\%$. Using the value of $T_m = 2.7025\%$ obtained earlier from direct measurement, this implied a lumped mirror absorption loss $A_m \approx .066\%$.

For the cavity loaded with the crystal, finesse measurements were polarization dependent, as would be expected as a result of the polarization dependent crystal surface reflection coefficients R_x. However, while from direct measurement the ordinary (p) polarization was lossier than the extraordinary (s) polarization, the average finesse measurements of the loaded cavity showed the opposite trend, where the ordinary polarization consistently gave a higher finesse (implying lower loss). It was

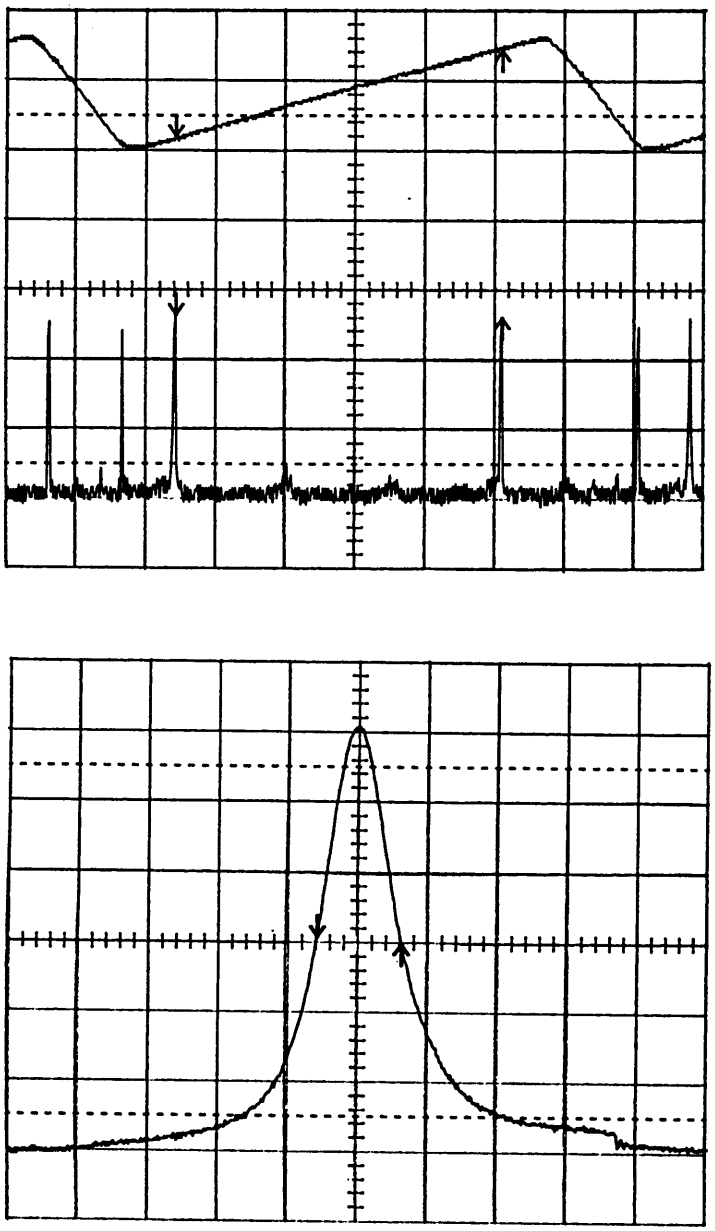

Figure 4.5: Measurements of cavity finesse. Top Graph: The top trace is the ramp voltage driving the PZT, while the bottom trace represents the output from the photodetector measuring the transmission through the OPO. The distance between consecutive peaks is the FSR (denoted by cursors). Bottom Graph: An expansion of one of the transmission peaks for measurement of the FWHM (denoted by cursors).

perhaps due to a preferential alignment of the ordinary beam which resulted in a multiple cavity effect. The average finesse for the extraordinary polarization F_s was $\sim$185 while for the ordinary polarization F_p was $\sim$191, implying total losses $\kappa_{s,p}$ of 3.396% and 3.289% respectively. Using these values to extract the crystal absorption, we found

$$\begin{aligned} A_x &= \frac{\kappa - (T_m + A_m + 4R_x)}{2} \\ &= .153\% \text{ per pass, extraordinary (s) polarization} \\ &= .00025\% \text{ per pass, ordinary (p) polarization} \end{aligned}$$

where there is a clear nonsensical discrepancy with the results from direct measurement. This may have been due to the possible 10% error of the finesse measurements combined with the unexpected change in the relative losses between the polarizations as a result of a multiple cavity effect.

4.4.3 Cavity Reflection Measurements

In order to insure that the values obtained for the losses of the mirrors and crystal were sensible and reasonably accurate, a method that removed the nonlinearity of the PZT from the measurement was used [28]. To accomplish this, the reflected rather than the transmitted light from the cavity was observed. If the ratio of the minimum to maximum reflected power from the cavity as the length is scanned is designated as P, then it was shown that [28]

$$L = \left[\frac{1 \mp \sqrt{P}}{1 \pm \sqrt{P}}\right] T_m \tag{4.10}$$

where L is the internal loss in the cavity other than the lumped mirror transmission. Hence, for the empty cavity, $L = A_m$ whereas for the cavity loaded with the crystal, $L = A_m + 2A_x + 4R_x$. From this equation one solution will either be inordinately

high or low, implying only one correct solution. This result is purely a function of the minimum to maximum reflection ratios and hence independent of PZT nonlinearity.

Because the reflection measurement technique was dependent on a power ratio, it was necessary to carefully insure optimal mode matching to the cavity such that all available power was circulated in only the fundamental cavity mode. Any power that was in modes other than the TEM_{oo} mode had to be accounted for to insure the accuracy of the measurements. Fig. 4.6 shows a typical example of a cavity scan, where both the reflection and transmission were simultaneously monitored.

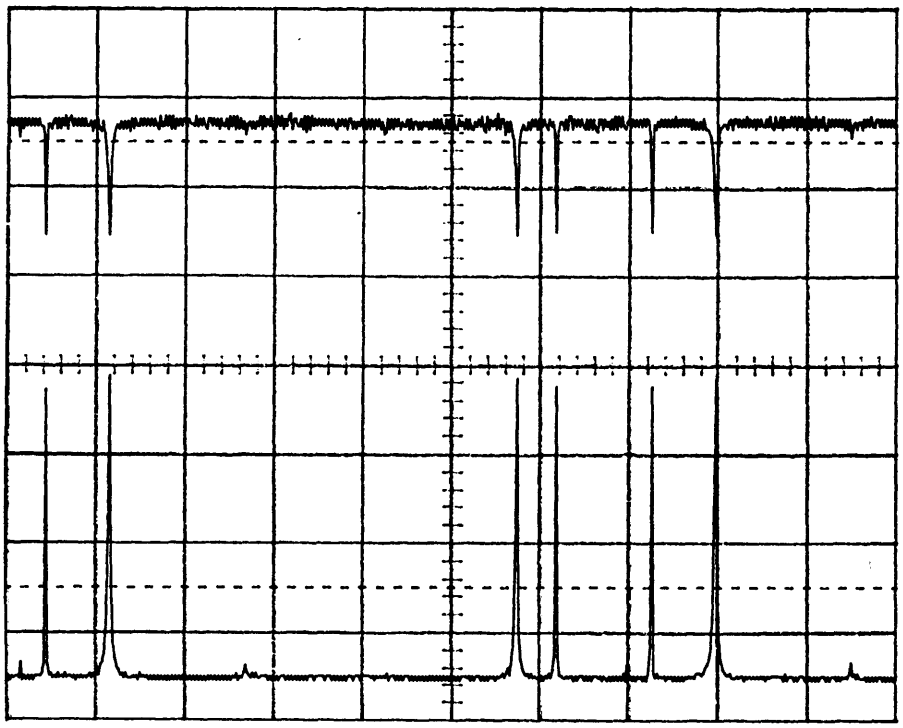

Figure 4.6: Example of cavity reflection measurements. Top trace shows reflected power, while bottom trace shows transmitted power. Note slight presence of a mode other than the fundamental, indicating less than optimal mode matching.

From reflection measurements of the empty cavity, a lumped mirror absorption $A_m \approx .06\%$ was obtained for both polarizations, in good agreement with the results obtained from the empty cavity finesse measurements (to within 10%). For the cavity

loaded with the crystal, the mirror absorption A_m and the crystal reflection R_x from direct measurement were used to extract the crystal absorption A_x. As in the transmission measurements, again the losses L measured in the ordinary (p) polarization were less than those measured in the extraordinary (s) polarization, although in repeated measurements the results did not fluctuate at the 10% level that was observed in the transmission measurements. Nevertheless, a nonsensical (negative) result was obtained for the ordinary polarization, while for the extraordinary polarization, A_x was found to be $\sim$.028%, in good agreement with the results from direct measurement of the crystal (.03%). This value was therefore used for both polarizations.

4.5 Threshold and Correlation Estimates

Table 4.2 summarizes the optical loss accounting for the OPO cavity, while Table 4.3 summarizes the other important physical parameters of the OPO. From Eq. (4.1),

Loss Source	**s(ext. polarization)**	**p(ord. polarization)**
Output Coupler, T	2.6857%	2.6857%
Extraneous Losses, μ:		
Input Coupler	0.017%	0.017%
Mirror Absorption	0.06%	0.06%
Xtal Surfaces (4 ea.)	0.32%	0.52%
Xtal Absorption (2 passes)	0.06%	0.06%
Total Round Trip Loss, κ	**3.143%**	**3.343%**
Corresponding Finesse	206.5	188
Average loss, both polarizations, κ_{avg}: 3.243%		
Average Finesse, F_{avg}: 195		

Table 4.2: Optical Loss Accounting for Three-Piece OPO Cavity.

utilizing the total round-trip losses κ from Table 4.2, the appropriate refractive in-

Physical Crystal Length	1 cm
Physical Cavity Length	1.9 cm
Optical Cavity Length, l_{cav} ($n_{avg} \approx 1.79$)	2.69 cm
Free Spectral Range ($FSR = c/2l_{cav}$)	5.58 GHz
"Cold" Cavity Bandwidth ($\Delta f = FWHM = FSR/F_{avg}$)	28 MHz
"Cold" Cavity Linewidth ($\Delta l = \Delta f \times \lambda/2FSR$)	2.67 nm
Above-Threshold Cavity Linewidth ($[\sqrt{2} - 1]^{1/2} \times \Delta l$)	1.7 nm
Above-Threshold Cavity Bandwidth	17.8 MHz
Confocal Parameter, b (in crystal)	3.22 cm
Mode matching parameters:	
Input: Effective Confocal Parameter b_{eff} Effective Beam Waist Location t_{eff}	 1.8 cm .335 cm from outer surface of input coupler 3.385 cm from outer surface of input coupler support tube
Output: Effective Confocal Parameter b_{eff} Effective Beam Waist Location t_{eff}	 1.02 cm 1.43 cm from outer surface of output coupler 4.4 cm from outer surface of output coupler support tube
Additional parameters for determining threshold:	
Nonlinear Coefficient, d_{eff}	2.178 pm/V
Reduction Factor, $\overline{h}(B, \xi)$	.31

Table 4.3: OPO Physical Parameters.

dices from Table 4.1, the parameters d_{eff} and $\overline{h}(B,\xi)$ from Table 4.3, a degenerate frequency $\omega_o = 1.775\times 10^{15}$ rad/sec, permittivity of free space $\epsilon_o = 8.854\times 10^{-12}$ F/m, and speed of light $c = 3\times 10^{8}$ m/sec, the single-pass OPO oscillation threshold pump power was estimated to be

$$P_{th}(\omega_p) \approx 660 \text{ mW}. \tag{4.11}$$

This was an optimistic value for the single-pass threshold, which assumed degenerate signal and idler frequencies; although the OPO was never operated in a single-pass pump configuration, the actual threshold power was most likely higher as a result of a detuning factor for nondegenerate outputs [6]. Nevertheless, this result served as a useful guide for developing and characterizing the OPO system design.

Likewise, the intensity correlation was estimated beginning with Eq. (4.2). This approximation assumed equivalent losses for both the signal and idler polarizations, therefore κ_{avg} from Table 4.2 was used for the quantity $(T+\mu)$. Furthermore, the spectrum was examined at DC ($f = 0$), which reduced the intensity correlation from Eq. (4.2) to the simple form

$$S_{ID}(0) = 1 - \frac{\eta T}{\kappa_{avg}} = 1 - \frac{\eta T}{T + \mu_{avg}}. \tag{4.12}$$

This result highlights the essential elements relevant to optimizing the intensity correlation; the greater T, the greater the probability the signal and idler photons will be coupled out of the cavity together, and the better the intensity correlation. Likewise, decreasing μ_{avg} reduces the number of photons "destroyed" in the cavity; since loss is a random photon depletion process, decreasing the extraneous losses increases correlation. Finally, a less than ideal detection system ($\eta < 1$) randomly deletes incoming photons and hence reduces correlation. Taking $\eta = 1$ to represent ideal detection at the OPO output, the estimated correlation at DC from Eq. (4.12) was

$$10\log S_{ID}(0) = -7.65 \text{ dB}.$$

While this estimate was illustrative, it was nevertheless again optimistic. We ignored the detection efficiency, the loss mismatch between the signal and idler polarizations, and the effect of excess pump noise, which in Ch. 3 was shown to be significant at frequencies below 3 MHz. All of these factors were shown in Ch. 2 to reduce the observable correlation. Additionally, as a practical matter the correlation spectrum should be observed at frequencies where the pump is shot noise limited, i.e. greater than ~3 MHz. As a result, the Lorentzian denominator in Eq. (4.2) additionally reduces the observable correlation from the DC value. A more detailed estimation of the correlation spectrum which includes these considerations will be utilized in Ch. 5 to compare with the experimental measurements.

4.6 The Triply Resonant OPO System

The estimate for the single-pass threshold given by (4.11) far exceeded the available pump power of ~160 mW (Table 3.3). Up to this point however, we have not considered that the output coupler was highly reflective for the pump wavelength (R = 98.7% @ 531 nm). If the output coupler pump field reflectivity coefficient is denoted by r_p, the threshold is reduced for the double-pass pump configuration by a factor of as much as $(1 + r_p)^2$ [5]. The exact reduction depends on the details of the relative phase shifts of the reflection coefficients of the three waves at the mirror, which is in turn determined by the mirror coatings. For $r_p \approx 1$, which is the case considered for this OPO design, the reduction factor has a minimum value of 2 and a maximum value of 4, where for the maximum value we assume that the phase relationships are preserved upon reflection so that the crystal interaction length is essentially doubled.

To verify this, the rear mirror of the laser was replaced to allow the maximum pump source power to be increased to ~400 mW. This alteration disabled the frequency stabilization mechanism described in Ch. 3. The OPO was mode matched

and aligned to the pump, the cavity length was scanned (via the method described in Sec. 5.4) and the outputs were monitored with a photodetector. Lasing was observed at a threshold power of between 330 to 370 mW, suggesting that the double-pass reduction factor was on the order of two.

At best however, applying this reduction factor still put the oscillation threshold well above the limit of the available pump power under conditions of frequency stabilization. To overcome this limitation, an alternative design was implemented which relied on utilizing a triply-resonant condition for the OPO, with a substantial pump cavity finesse F_p (so that essentially the pump made several passes through the crystal). Since there was already some small reflection of the pump by the input coupler of the OPO, the double-pass configuration was in fact more like a very low finesse cavity for the pump, or a "weakly" triply-resonant OPO, with an F_p on the order of 5 or less. Since the threshold pumping power scales approximately as $\kappa_s\kappa_i/F_p$ [27], holding cavity losses constant and increasing F_p by a factor of 10, for example, would result in thresholds on the order of 30-40 mW, well within the range of the available pump power. This was the premise for the three-mirror triply-resonant cavity design (Fig. 4.7).

The novel feature of implementing the triply-resonant OPO was the use of a third external mirror in tandem with the doubly-resonant cavity. A two-cavity four-piece system resulted in which both cavities shared the output coupler. The reflectivity of the third external mirror (pump resonator input coupler) determined the pump cavity finesse. However, this mirror did not affect the "inner" OPO cavity finesse or losses. Additionally, it was possible to independently tune the "outer" pump cavity and the inner signal and idler cavity using PZTs on each of the input couplers. Stabilization for continuous operation required two cavity length servo control systems, which are described in Ch. 5.

The pump cavity input coupler was supplied by Lightning Optics, Inc. It had a radius of curvature of 10 cm and a reflectivity $R = 90\%$ at the pump wavelength

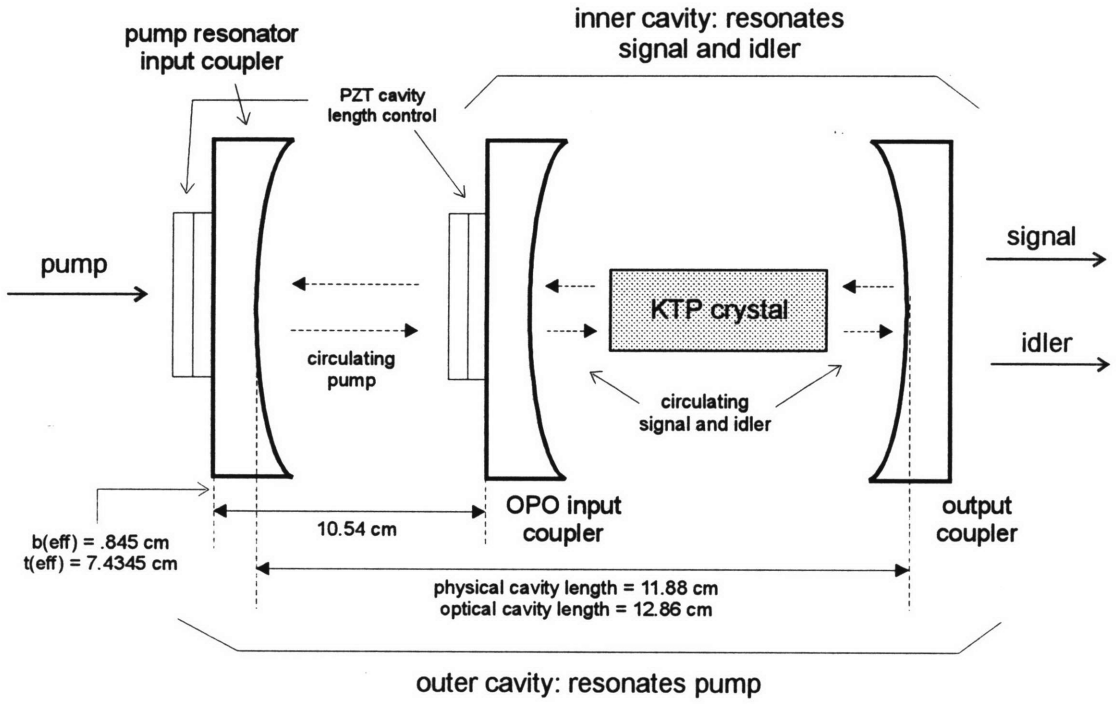

Figure 4.7: A four-element triply resonant OPO.

and was 9.5 mm thick. The mirror was epoxied to a stack of two PZTs and mounted in a Lees stand which permitted horizontal and vertical adjustment about the mirror axis. The mirror assembly was placed such that the outer flat surface was 10.54 cm from the outer flat surface of the OPO cavity's input coupler (this was the distance at which the radius of curvature of the circulating Gaussian pump beam in the cavity matched the mirror radius of 10 cm). Once the system was successfully aligned to allow resonance, transmission measurements of finesse were performed where an $F_p = 55$ was observed. Table 4.4 summarizes the physical parameters of the pump resonator cavity.

Another point of consideration for the higher finesse pump cavity was to insure that the resulting linewidth was larger than the OPO cavity linewidth in order to facilitate the observation of oscillation modes while the pump cavity length was scanned. This enabled optimization of cavity alignment and threshold estimates without the

Physical Cavity Length	11.88 cm
Optical Cavity Length	12.86 cm
Free Spectral Range (FSR)	1.2 GHz
Finesse (F)	55
Cavity Bandwidth (Δf =FWHM)	21 MHz
Cavity Linewidth ($\Delta f \times \lambda/2FSR$)	4.75 nm
Input mode matching parameters:	
Effective Confocal Parameter b_{eff}	.845 cm
Effective Beam Waist Location t_{eff}	7.4345 cm

Table 4.4: Physical Parameters of Pump Resonator Cavity.

need to stabilize either of the cavities for continuous operation. From Tables 4.3 and 4.4, the pump cavity and OPO cold-cavity IR linewidths were 4.75 nm and 2.67 nm respectively. Above oscillation threshold however, the double-resonance condition is satisfied, and the OPO cavity can be thought of as two cavities in series, so that it has a double Lorentzian line shape [21]. This led to an OPO IR linewidth equal to $(\sqrt{2}-1)^{1/2}$ times the cold-cavity linewidth, or 1.7 nm, which was sufficiently less than the pump linewidth. Upon scanning the pump cavity with a ramp voltage applied to the input coupler PZT, lasing of the inner OPO cavity was observed (by monitoring the OPO output with a photodetector) at thresholds between 40 and 60 mW. Qualitatively, this was in good agreement with the estimated predictions and well below the limits of the pump laser system.

4.7 Summary

In this chapter, we have discussed in detail the design of the OPO cavity, and the methodology used to determine estimates for the oscillation threshold and intensity correlation spectrum based on a thorough characterization of the optical losses. A

novel triply-resonant three mirror two cavity system was introduced which substantially reduced the demands on the pump system for achieving oscillation threshold. The oscillation threshold of the triply-resonant system was observed to be on the order of 40 to 60 mW, in good agreement with the estimated predictions.

Chapter 5
Experiment

5.1 Introduction

In this chapter we outline the experiment for measuring the intensity correlation between the twin beam outputs of the OPO. Following the general description of the experiment, the cavity stabilization techniques utilized for achieving continuous-wave operation of the triply-resonant OPO are discussed in detail. We then turn to the determination of the detection efficiency η which takes into consideration all optical components in the beam path from the OPO output to the photodetector amplifier, and includes the photodetector efficiency. The detection and signal amplification circuitry are discussed briefly. Finally, the experimental results are presented and compared to the theoretical model.

5.2 Experimental Outline

Figure 5.1 shows the basic experimental arrangement. The OPO was pumped by a single-mode Kr^+ laser, whose properties are summarized in Table 3.1. The pump beam passed first through a quarter-wave ($\lambda/4$) plate oriented so as to remove any ellipticity imparted to the beam after several reflections from mirrors in the pump system. The resulting beam was 45° linearly polarized. The pump beam was then mode matched to the pump resonator cavity using the parameters given in Table 4.4. A half-wave ($\lambda/2$) provided polarization rotation so that the pump beam was horizontally (p) polarized as required by the phase matching conditions (Fig. 4.3).

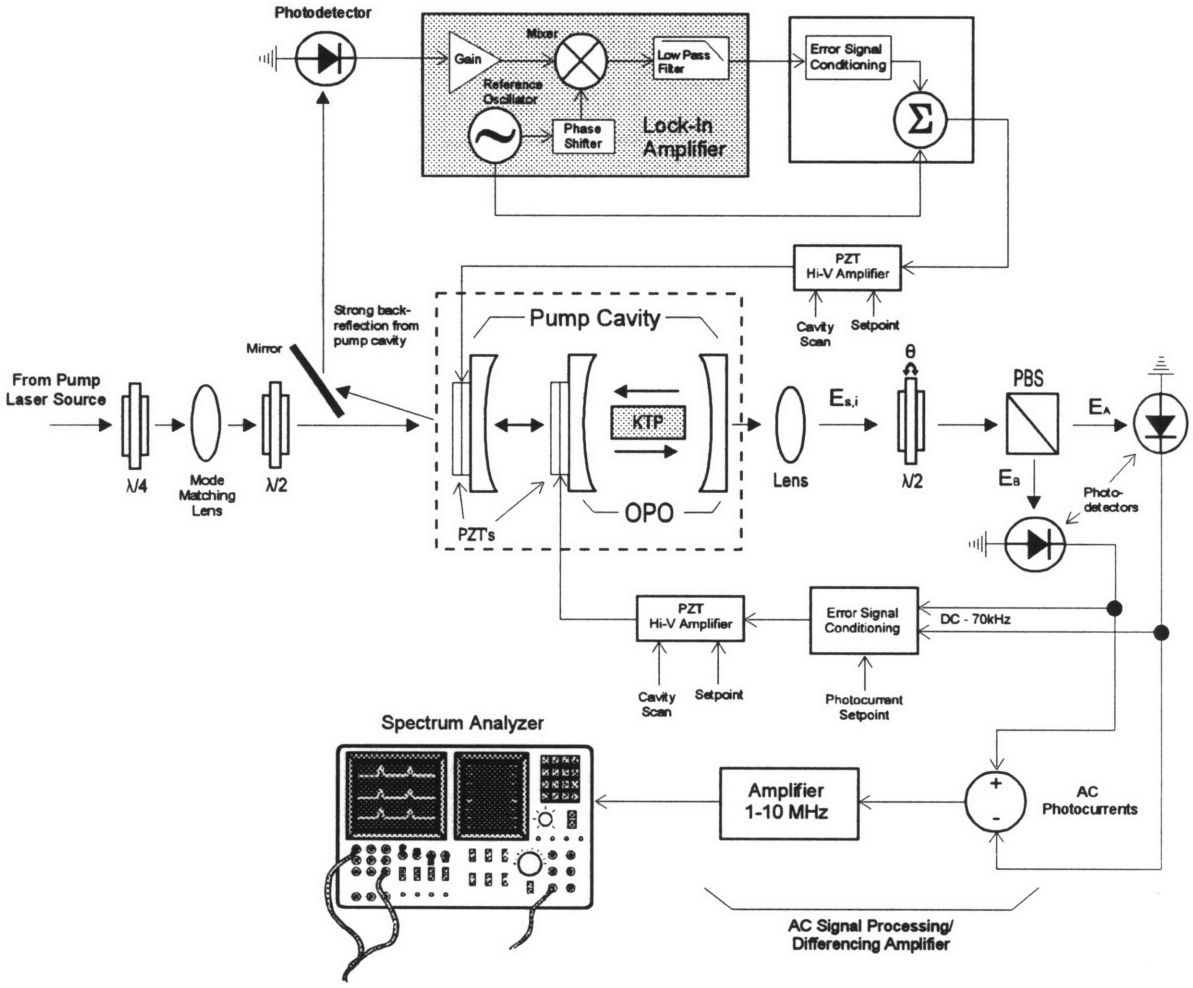

Figure 5.1: Overview of experimental setup.

After stabilization of the pump resonator and OPO cavities, the signal and idler beams exiting the OPO first passed through a lens which focused the outputs onto the photodetectors. The signal and idler beams were separated after the cavity by means of a polarizing beam splitter (PBS). Each of these beams was monitored by a photodiode, whose output went to a DC servo amplifier (error signal conditioning) for OPO cavity stabilization as well as an AC differencing amplifier. The low frequency outputs of the photodetectors (DC to 70 kHz) were added together and used to actively stabilize the intensity of the twin beams, each held at about 1 mW by means of a servo piezoelectric control of the cavity length. The AC portions of the photodiode signals (1 to 10 MHz) were subtracted and the resultant AC intensity difference was recorded on a spectrum analyzer. The balance of the AC differencing network was critical to the observable degree of correlation, and was verified by modulating the twin beam intensities (via the pump intensity servo auxiliary input, Fig. 3.1) and observing the reduction in the modulation peak when the intensities were subtracted. The total optical and electrical common-mode rejection was typically up to -30 dB across the bandwidth of the differencing amplifier.

A key point for the reliability of this experiment was the calibration of the shot noise level. A novel method employed by Mertz et al. [27] used a rotating half-wave plate ($\lambda/2$) inserted in front of the polarizing beamsplitter. The two fields E_s (signal) and E_i (idler) emitted by the OPO undergo a polarization rotation of 2θ in the half-wave plate, where θ is the angle between the axes of the plate and the polarizer. The two fields E_A and E_B, respectively transmitted and reflected by the polarizing beam splitter, are [15]

$$\begin{aligned} E_A &= E_s \cos(2\theta) - E_i \sin(2\theta) \ , \\ E_B &= E_s \sin(2\theta) + E_i \cos(2\theta) \ . \end{aligned} \tag{5.1}$$

When $\theta = 0°$ (modulo 45°) relative to the vertically polarized OPO output, the half-

wave plate played no role and the measured signal was the difference between the twin beam intensities. When $\theta = 22.5°$ (modulo 45°), the system of half-wave plate and polarizing beam splitter acted like a usual 50% beam splitter; essentially, the signal and idler beams were "mixed" by the half-wave plate, and the photons impinging on the beam splitter appeared to randomly select reflection or transmission by the beam splitter. In this manner, all correlation was effectively removed from the two detected beams with the result that the respective noise powers of the mixed uncorrelated beams A and B *added together* when the intensities were subtracted. The rejection of the common-mode pump induced excess noise was intact. Consequently, the measured signal gave the corresponding shot noise level for a beam of intensity $I_s + I_i$. It can be shown from Eq. (5.1) that the noise power spectrum $S_\theta(f)$ for the difference signal $I_A - I_B$ varies sinusoidally as a function of the angle θ

$$S_\theta(f) = S_{ID}(f)\cos^2(4\theta) + S_{SNL}\sin^2(4\theta) \tag{5.2}$$

where Eq. (4.2) has been used. Figure 5.2 shows this relation for a single frequency f=8 MHz, where a strong modulation of the noise level was observed with the expected periodicity of 45°. For the experiment in [15], the noise level at 0° which corresponds to no mixing (correlated outputs) was about 30% lower than that at 22.5°, which corresponds to mixed signal and idler beams (no correlation).

5.3 Pump Resonator Cavity Stabilization

A "dithering" technique was used to stabilize the cavity length of the pump resonator. A desirable characteristic of this scheme was that it locked the cavity to a resonance peak (as opposed to the "side-locking" technique used for the OPO, to be described later). Referring to Fig. 5.1, the major components of the stabilization scheme included a photodetector, a lock-in amplifier, error signal conditioning electronics

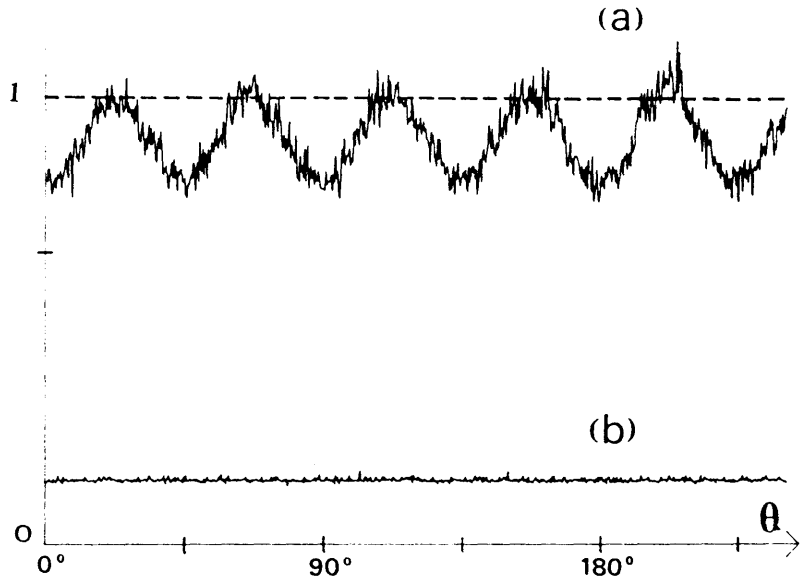

Figure 5.2: Trace (a), variation of the normalized noise power $S_\theta(f)$ as a function of $\lambda/2$ plate rotation θ for f=8 MHz (measured as noise spectrum of the photodiode currents). Trace (b), input noise level equivalent to the electronic noise of the associated circuitry. The dashed line shows the shot noise level measured on a YAG laser having the same intensity. The modulation of the noise level has the expected periodicity of 45°. From [15].

and a PZT high voltage driver.

A general description of the stabilization scheme is as follows: a small modulation (dither) was applied to the pump resonator input coupler PZT. Reflection from the pump cavity was monitored by a photodetector. As the cavity mode drifted slightly off the center of a resonance, the reflected intensity was modulated at the frequency of the dither as the slope of the resonance moved over the mode. The phase of this intensity modulation was dependent on the direction of drift and the magnitude was related to the magnitude of the resonance shift. The intensity modulation at the dither frequency was detected with a phase-sensitive amplifier and used as an error signal to lock to the peak of a cavity resonance.

The key component of the dithering method was a Stanford Research Systems SR830 lock-in amplifier. This provided the reference oscillator, phase-sensitive amplifier and part of the error signal conditioning. The major functional elements of

the lock-in amplifier consist of a variable gain amplifier, a local reference oscillator, a phase shifter, a mixer (phase sensitive detector) and a parametric low-pass filter.

The reference oscillator was taken directly from an auxiliary output of the lock-in amplifier, and for illustrative purposes we will use this as the "zero-phase" reference; i.e., the dither signal was given by $V_{dith} = A\cos(2\pi ft)$, where the amplitude A was chosen to be 2 mV_{rms} and the dither frequency f was chosen to be 10 kHz (the choice of these parameters will be explained shortly). Upon reflection, the magnitude and phase of the dither signal is dependent on the magnitude and direction of the cavity length drift from resonance. The detected dither signal was then given by $V_{det} = B\cos(2\pi ft + \theta_{det}(t))$ where B includes the gain of the photodetector amplifier. This was the input signal to the lock-in amplifier, which, following an adjustable gain stage, was demodulated with a phase-shifted version of the reference oscillator, given by $V_{ref} = C\cos(2\pi ft + \theta_{ref})$. Using the appropriate trigonometric identities, after demodulation and low-pass filtering we obtain the error signal

$$e(t) = \frac{1}{2}BC[\cos(\theta_{ref} - \theta_{det}(t))]. \tag{5.3}$$

The necessary property of the error signal is that it be a zero-crossing signal, where the zero-crossing indicates a resonance peak. Additionally, the error signal must satisfy the condition of negative feedback for the closed loop system, i.e., a positive error signal drives the PZT movement such that a more negative error signal results, and vice-versa. This was accomplished as follows: from Eq. (5.3), $e(t)$ will be zero when $[\theta_{ref} - \theta_{det}(t)] \approx 90°$. Although $\theta_{det}(t)$ is a function of time due to fluctuations from atmospheric disturbances, the DC bias of the PZT may be manually adjusted (with the loop "open") such that the cavity is as close as possible to resonance (this can easily be monitored from the photodetector output). At this point, while observing the error signal output from the lock-in, θ_{ref} was adjusted to minimize the amplitude of the random fluctuations of the error signal, indicating that

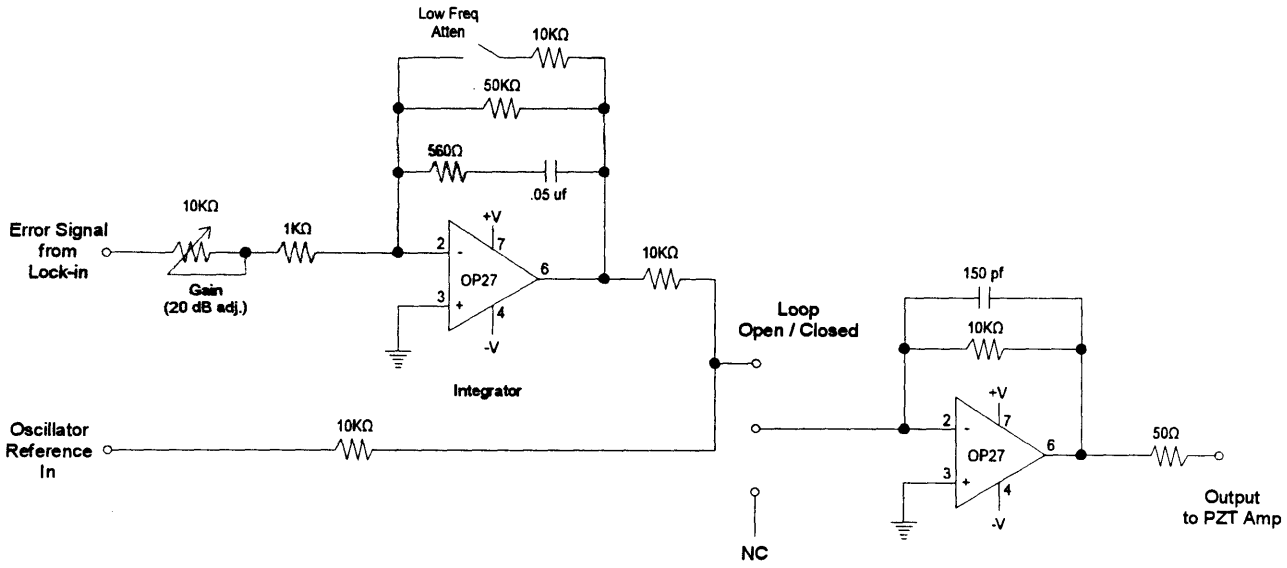

Figure 5.3: Supplemental electronics for dither error signal conditioning.

the condition $[\theta_{ref} - \theta_{det}(t)] \approx 90°$ was satisfied. In this experiment, typical values of θ_{ref} which minimized the error signal were from $\sim+50$ to $+60°$.

The signal that was really desired for a zero-crossing phase discriminator was $\sin((\theta_{ref} - \theta_{sig}(t))$, which was accomplished by adding or subtracting an additional 90° to θ_{ref}. Adding or subtracting resulted in either positive or negative feedback, hence this was decided empirically during the course of the experiment.

The low-pass filter in the lock-in amplifier additionally served as a first stage of error signal conditioning. The error signal output of the lock-in was subsequently passed to the circuit of Fig. 5.3 which shows an integration stage with a 20 dB variable gain. The combined effect of the variable gain amplifier and low-pass filter of the lock-in and this additional variable gain integration stage was to provide the appropriate high gain at low frequencies and quick roll-off necessary for closed loop stability.

Fig. 5.4 shows the combined frequency response of the amplifier and two integration stages. The supplemental circuitry also summed the conditioned error signal with the reference oscillator signal. These combined signals were sent to a Burleigh RC-43 high voltage amplifier used to drive the PZT, which had an adjustable gain from 9 to 100 V/V.

The cavity was stabilized as follows: the loop was first "opened" via a switch in the supplemental electronics which disconnected the summed error signal and reference oscillator from the PZT amplifier. A ramp voltage from the PZT amplifier (0-500V @ 50 Hz) was applied to the PZT so that the cavity resonances were observed by monitoring the photodetector output, noting the bias voltage at which the resonance occurred. The ramp was turned off, and the PZT amplifier output was adjusted to a DC bias voltage close to resonance. While monitoring the error signal and the photodetector output, the loop was closed, and the PZT bias was adjusted slightly until the system was locked to a resonance peak. The loop gain was adjusted through the lock-in sensitivity, the gain of the supplemental electronics and the PZT amplifier so that a minimum fluctuation resulted around the peak resonance. The error signal should be a zero-mean signal, and this was accomplished by further fine-tuning of the PZT DC bias.

The pump cavity was successfully locked to a resonance peak with residual peak to peak fluctuations equal to ~4% of the resonance peak. The lock was quite robust and resisted common ambient disturbances. A major component of the residual fluctuations was between 200-400 Hz, due to water cooling of the laser pump source as discussed in Ch. 3. Another detectable component was at 20 kHz, which was twice the dithering frequency. The source of this fluctuation was a result of locking as close as possible to the peak resonance, where the dither underwent a phase (sign) change; in essence, half of a cycle of the dither got "cut-off" as the peak was traversed back and forth due to error correction, and appeared as a residual fluctuation at twice the dither frequency. This frequency was well beyond the response of the error

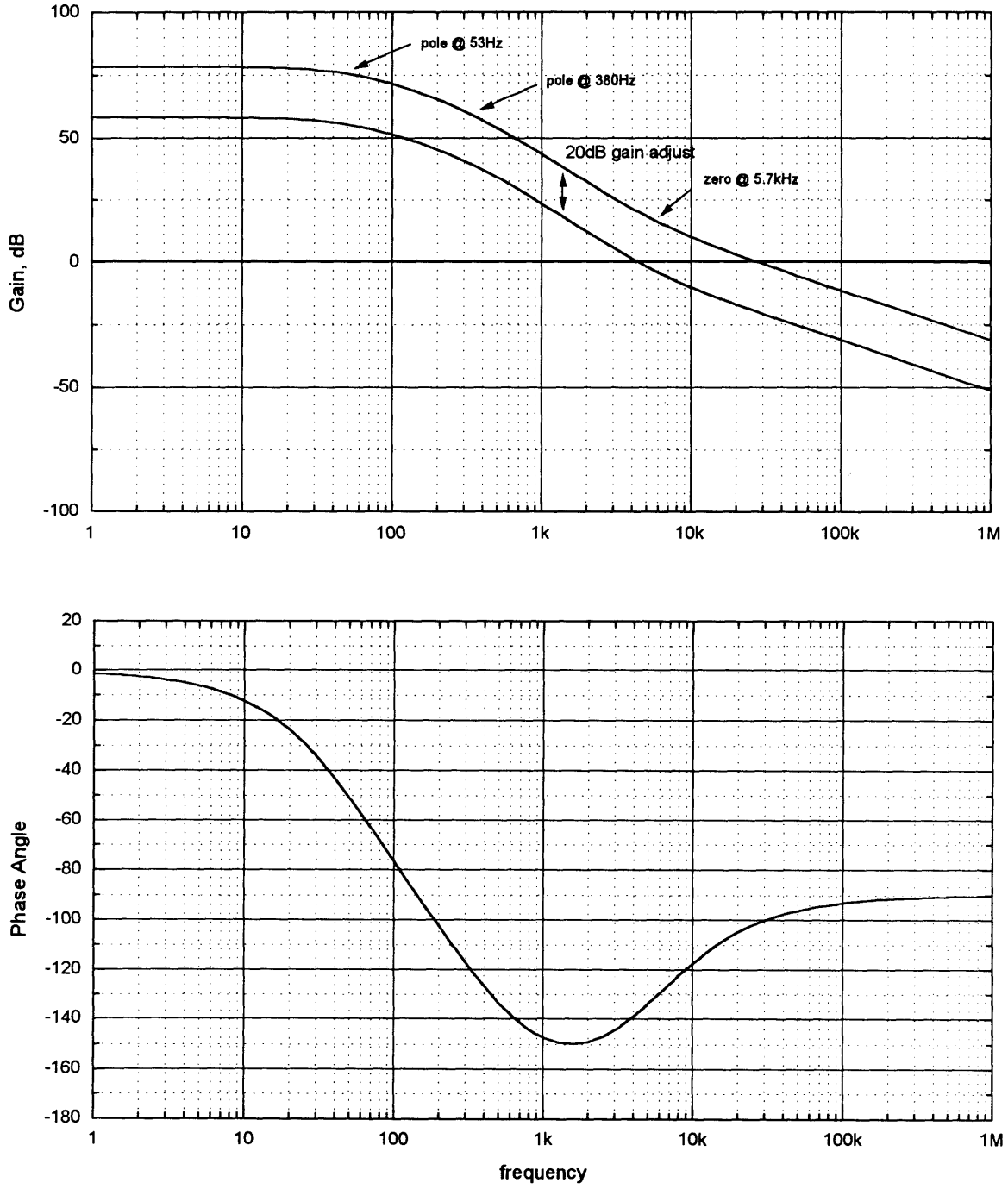

Figure 5.4: Frequency response of dither error signal conditioning electronics.

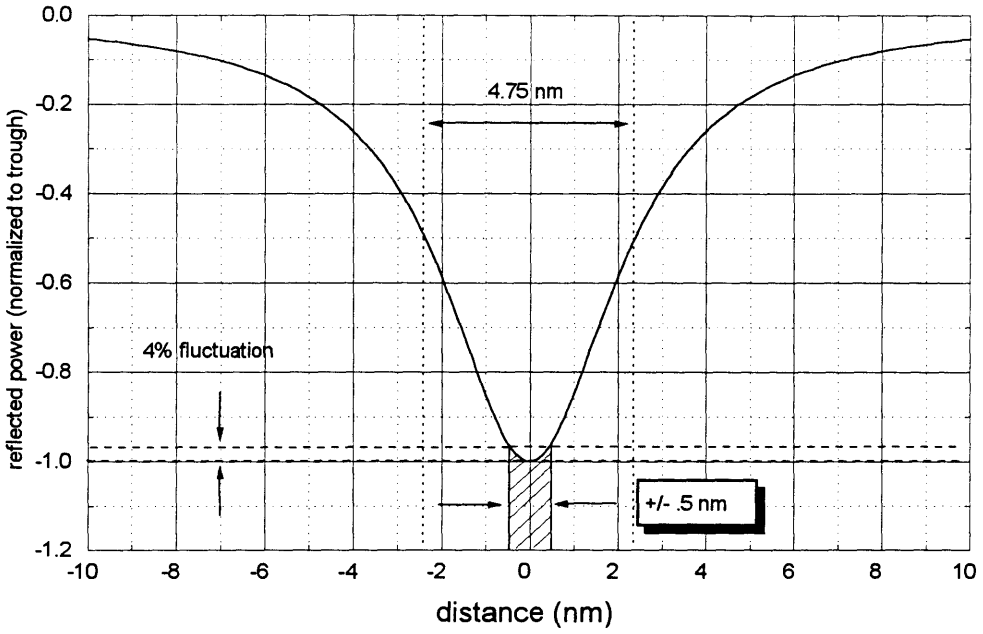

Figure 5.5: Lorentzian profile of cavity resonance (reflection measurement). A 4% fluctuation around the trough corresponds to $\sim \pm .5$ nm fluctuation for a pump cavity linewidth of 4.75 nm.

conditioning electronics (but not beyond the PZT bandwidth of ~30 kHz). As a result, the amplitude of the dither signal was kept as low as possible to still allow a robust lock while minimizing the residual fluctuation at twice the dither frequency.

Using a straight-line (triangular) approximation for the Lorentzian resonance profile, and the pump resonator cavity linewidth of 4.75 nm (Table 4.4), the 4% residual intensity fluctuations conservatively corresponded to a $\sim \pm .18$ nm fluctuation. In actuality, for the Lorentzian profile this fluctuation was greater by a factor of almost three, as shown in Fig. 5.5, where we see a 4% fluctuation for a linewidth of 4.75 nm corresponds to $\sim \pm .5$ nm.

This fluctuation was potentially problematic for the stabilization of the OPO cavity. Due to its smaller oscillating mode linewidth of 1.7 nm (Table 4.3), a $\pm .5$ nm fluctuation of the pump translated to almost a $\pm 30\%$ (60% peak-to-peak) fluctuation around the OPO cavity lock-point. The selection of a 10 kHz dither was also pre-

Lock-in Amplifier Parameters:	
Reference Oscillator Frequency	10 kHz
Reference Oscillator Amplitude	2 mV_{rms} (set to 4 mV_{rms} with 3 dB attenuation pad on output)
Reference Oscillator Phase (typical)	~-35° (+55°- 90°, determined empirically)
Input Gain Sensitivity	10 mV
Filter Time Constant τ	30 ms, 6 dB/octave
Filter Pole ($1/2\pi\tau$)	53 Hz
Overall Gain (10 V/sensitivity)	1000 (60 dB)
Residual Fluctuations in locked state	4% of resonance peak

Table 5.1: Important parameters and results of pump resonator cavity stabilization.

cipitated by the effect that the residual 20 kHz fluctuation would have on the OPO stabilization and measurement electronics. These considerations will be discussed in the next section. Table 5.1 summarizes the important results of the pump resonator cavity stabilization, including parameters of the lock-in amplifier.

5.4 OPO Cavity Stabilization

Once the pump cavity was stabilized and locked onto a resonance peak, the OPO cavity length could be scanned (by applying a ramp voltage to the input coupler PZT) to observe a set of resonant mode clusters (Fig. 5.6). This required that the OPO cavity was properly aligned and that the circulating pump power in the pump resonator cavity was above the oscillation threshold of the OPO. To facilitate the observation of the mode clusters, the PZT ramp voltage should be sufficient to scan at least one full free spectral range (FSR) of the cavity, which in this case was 532 nm. Using the PZT response of 0.8 nm/V, this implied a ramp voltage of ~670 V. For the experiment, available equipment limited the scanning voltage to ~330 V, which was

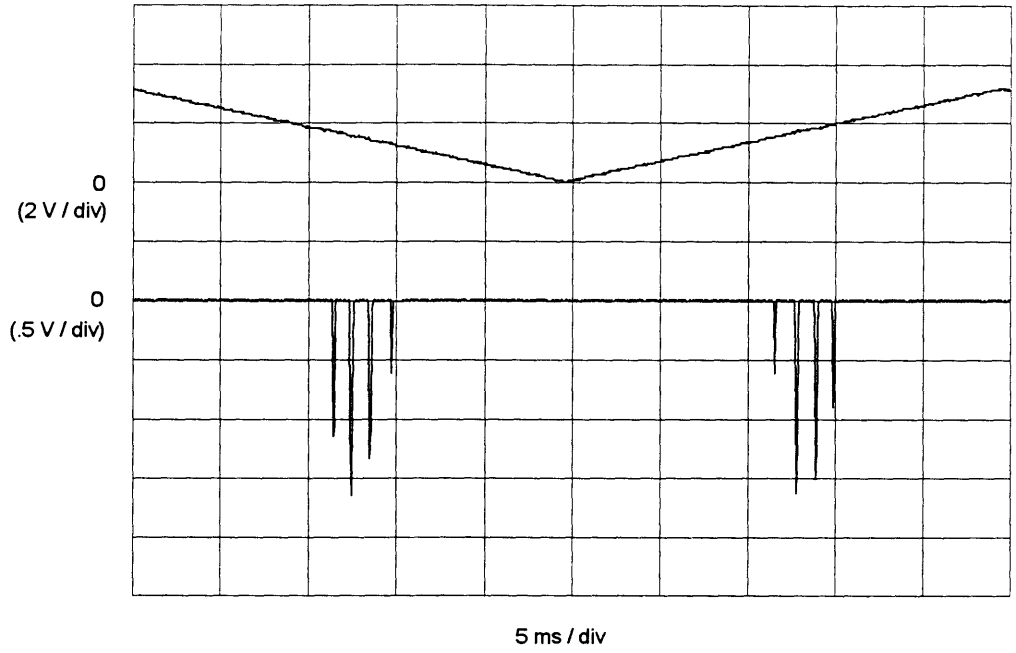

Figure 5.6: Trace of mode clusters from the OPO. The top trace represents the PZT scanning ramp voltage divided by 100 (triangle wave, 20 Hz scanning rate).

nonetheless sufficient to observe the mode clusters.

In theory, scanning the OPO cavity input coupler should have little or no effect on the pump resonator cavity (Fig. 4.7). This mirror was anti-reflective (AR) coated for the pump wavelength on its outer surface, and minimally reflective on its curved surface. Its thickness (4 mm) and refractive index (n = 1.468) were taken into consideration for the pump cavity resonance and mode matching calculations; therefore, regardless of where it was located within the pump cavity, it should not change the resonance condition. In practice, however, scanning the OPO input coupler slightly altered the beam path within the pump resonator cavity, probably due to a slight horizontal displacement of the curved mirror. Hence, under locked conditions for the pump cavity, it was observed that although it remained locked, the power level fluctuated by as much as 25% as a function of the OPO input coupler position during a scan, as shown in Fig. 5.7. This was not problematic however regarding

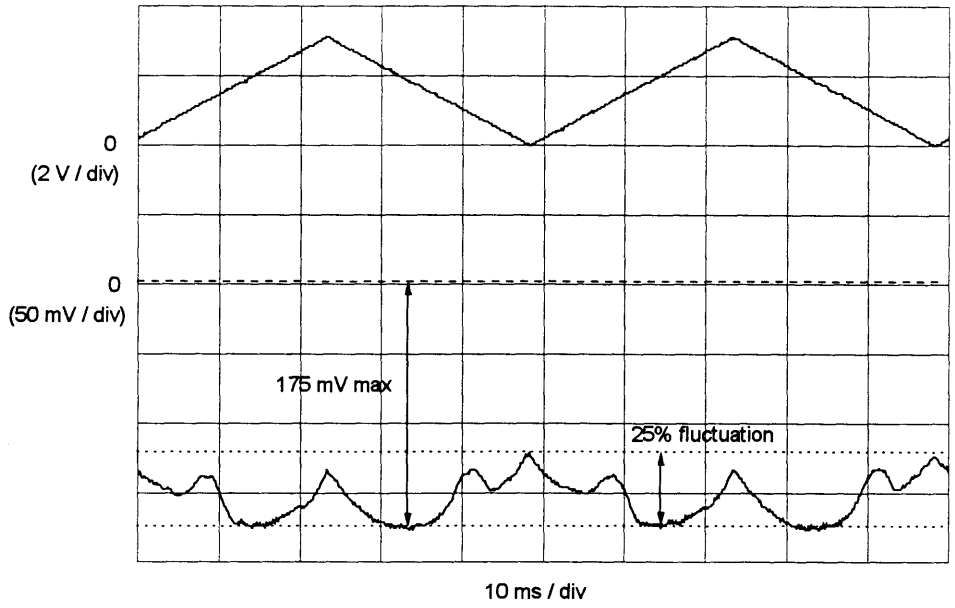

Figure 5.7: Reflected power from locked pump resonator cavity during OPO cavity scan below threshold. Top trace (2 V/div), ramp voltage applied to OPO input coupler PZT. Bottom trace (50 mV/div, zero at center grid), reflected power from pump cavity. As the OPO input coupler is displaced, the beam path within the pump cavity is altered and hence the resonant power fluctuates by 25%.

the observation of OPO output mode clusters, and was not a concern for continuous operation when the OPO cavity length was locked and stabilized.

A "side-lock" technique was used to stabilize the cavity length of the OPO. Generally speaking, the side-lock technique has the potential of providing a "tighter" lock than the dithering technique, for it eliminates the consequence of residual fluctuations at twice the dither frequency when locking on a resonance peak. This however comes at the expense of locking the cavity at less than the full resonant power output. Since the intensity correlation measurement had no strict power requirements for the signal and idler outputs, operation of the OPO at less than full resonant output power was not a big disadvantage. Fig. 5.8 illustrates the side-lock technique for the OPO double Lorentzian line.

Referring to Fig. 5.9, the major components of the OPO stabilization scheme included the signal and idler photodetector/amplifiers, error signal conditioning elec-

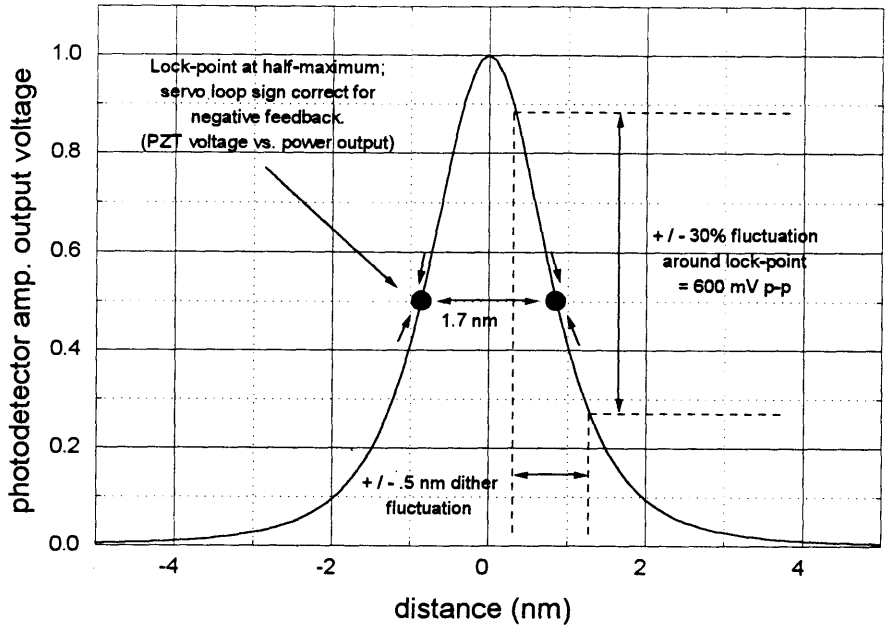

Figure 5.8: Illustration of side-lock technique for OPO double Lorentzian line. Lock-point fluctuations due to pump cavity dither are shown.

tronics, a PZT high voltage driver and a function generator which provided the ramp signal to sweep (scan) the cavity length. Fig. 5.10 shows the photodetector/amplifier circuit, Fig. 5.11 shows the error conditioning electronics and Fig. 5.12 shows the PZT high voltage driver electronics.

The generation of an error signal for the servo loop was accomplished as follows: Referring to Fig. 5.10, the signal and idler outputs of the OPO were incident on the photodetectors, and the DC portion of the amplification circuitry passed signals from DC to $\sim$70 kHz with a gain of $\pm$.5V/mA, and then dropped off at -40 dB/decade thereafter. The gains of the respective amplifiers were opposite in sign so that the AC signals could be subtracted via a summing amplifier, to be explained later.

The electronic signal from either of the photodetector/amplifier DC outputs was selectable as an input to the servo loop conditioning electronics (Fig. 5.11). This input was summed with a stable DC voltage reference setpoint which was the voltage

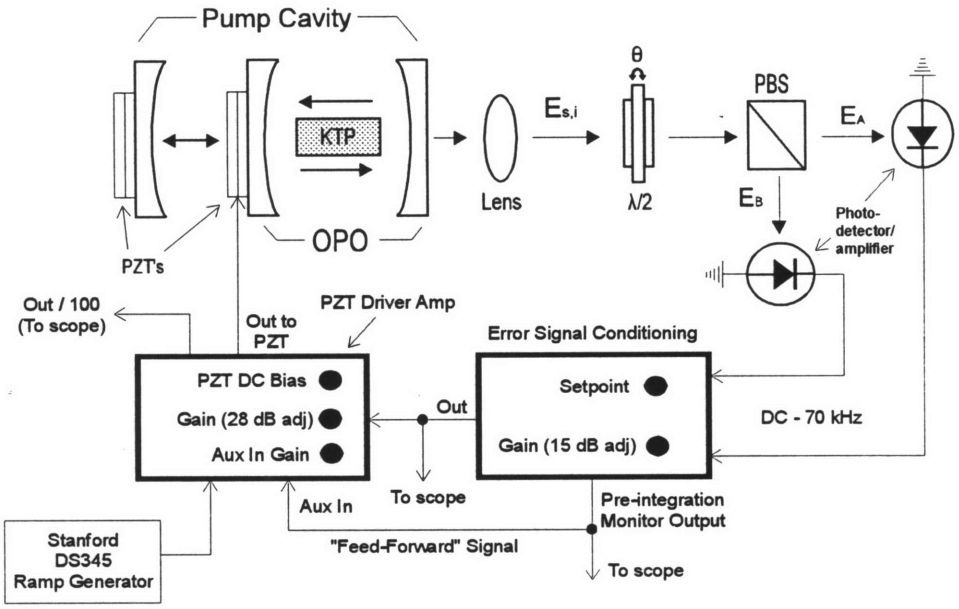

Figure 5.9: Detail of OPO cavity stabilization scheme.

equivalent of the lock-point on a resonance peak. Typically, the pump power was adjusted such that the signal and idler resonance peaks generated a photocurrent of 2 mA per detector (each slightly greater than ~2 mW). The desired lock-point was at the resonance half-maximum or 1 mA, corresponding to a DC reference setpoint voltage of .5 V. The output of this first comparator stage of the electronics served as the error signal; if the cavity length was such that the signal or idler output generated a photocurrent of 1 mA, the error signal would be zero.

The error signal was then passed to a sign-selection stage, which could invert the signal via a switch. This allowed empirically selecting the sign of the error signal such that negative feedback resulted for the closed loop. Essentially, this determined the side of the resonance peak that would be locked to (in practice, a thermal hysteresis induced asymmetry in the resonance peaks made it easier to lock to a leading edge [28]). The output of the sign-selection stage could be monitored by means of an external BNC connector ("pre-integration" monitor).

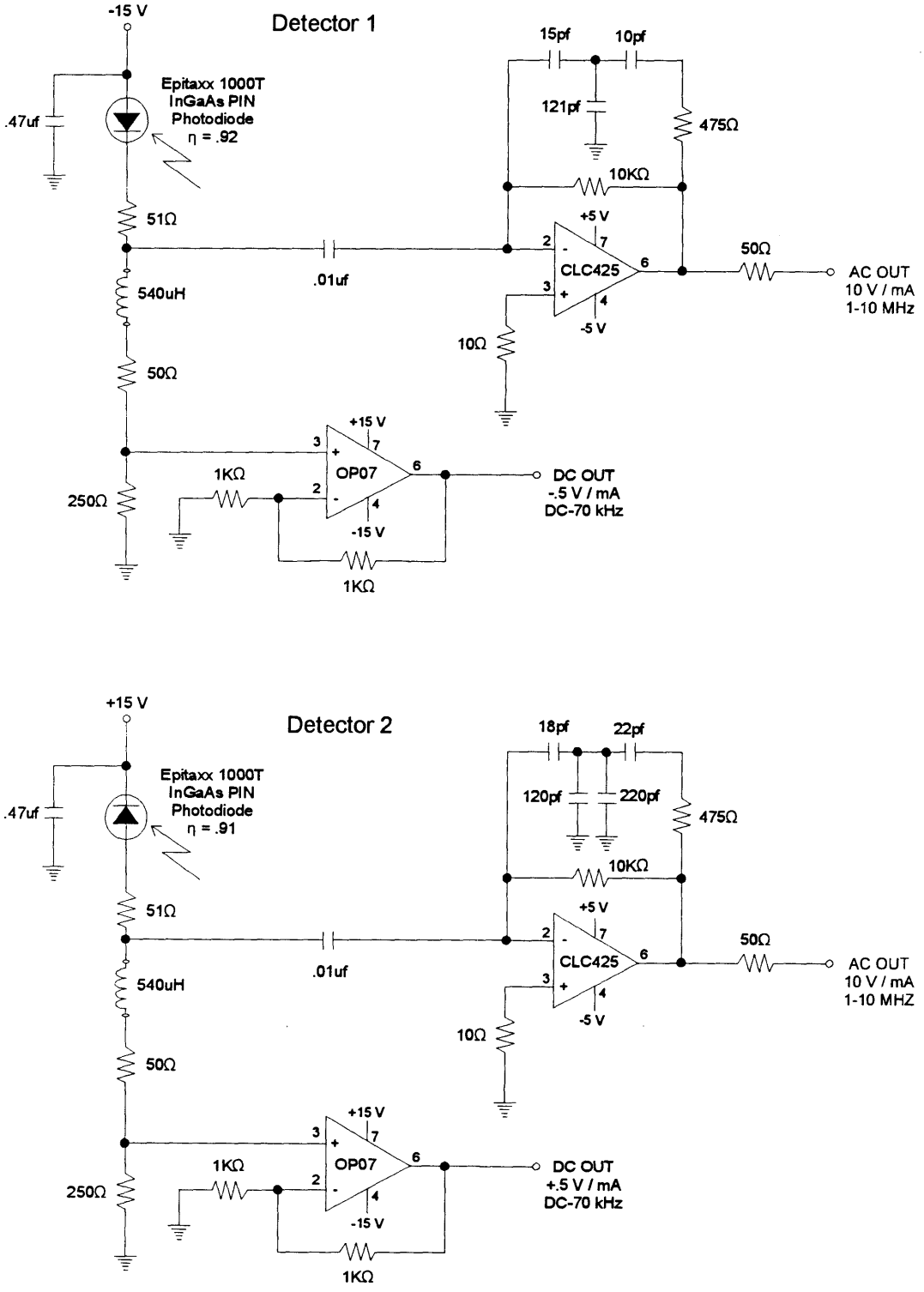

Figure 5.10: Schematic of photodetector/amplifier circuits for OPO outputs.

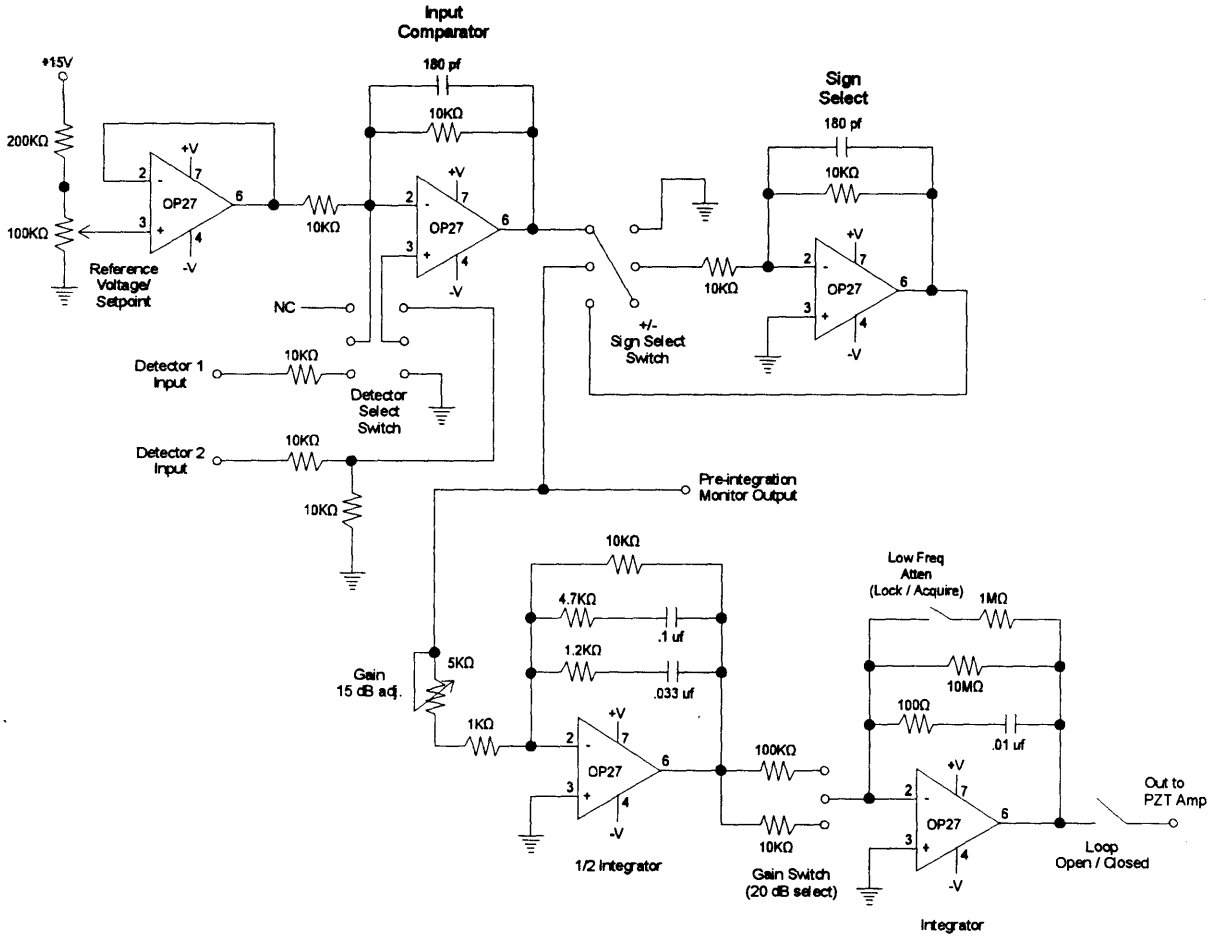

Figure 5.11: Schematic of error signal conditioning electronics for OPO cavity stabilization.

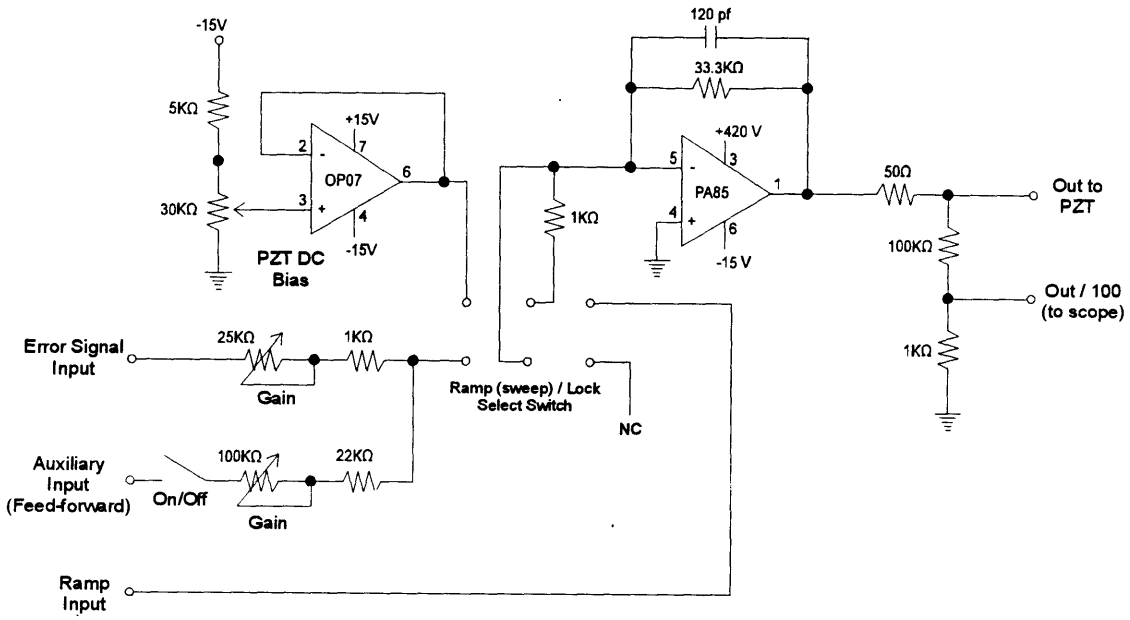

Figure 5.12: Schematic of PZT driver electronics for OPO cavity.

The next stage of signal conditioning consisted of a variable gain half-integrator followed by an integrator, which provided high gain at low frequencies and the frequency roll-off profile necessary for closed loop stability. The half-integrator had an adjustable gain of 15 dB, while the integrator gain could be selected via a switch for a 20 dB "boost". Additionally, the integrator stage contained a switch for low frequency attenuation to provide for easier "acquiring" of a lock. Fig. 5.13 shows the frequency response of the error signal conditioning electronics. The output of the error signal conditioning electronics was passed to the PZT driver (Fig. 5.12), which had an adjustable gain from 1.3 to 33.3 V/V (28 db of adjustment) for this input. This provided a total of ~60 dB of adjustment for the error signal gain. The error signal was summed with a DC bias which was used to locate the cavity modes, as well as an auxiliary input for additional "feed-forward" cavity stabilization, to be explained shortly.

The cavity was locked as follows: the cavity was first scanned to identify the positions of the mode clusters and the corresponding PZT bias voltage. A Stanford Research Systems DS345 function generator was used with a 10 V_{p-p} zero-mean triangular wave output at 20 Hz, offset by -5 V, so that the resulting ramp was from 0 to -10 V. This was input to the PZT amplifier (Fig. 5.12), which provided a gain of -33 V/V for this input, resulting in a scanning ramp voltage of 0 to 330 V, corresponding to a sweep range of 265 nm (as mentioned earlier, this was sufficient to observe mode clusters). The pump power was adjusted to achieve the desired resonance peak power of the OPO modes. Once the PZT DC voltage corresponding to a mode was identified, the PZT amplifier was switched to "lock" mode, where the conditioned error signal was summed with a DC bias which was adjustable from 0 to 420 V. While monitoring the selected photodetector output (via the "pre-integration" monitor) as well as the output of the error signal conditioning electronics, the PZT DC bias was adjusted approximately to a resonance, where the closed loop system locked to the setpoint (typically at half-max of the resonance peak) on the appropriately

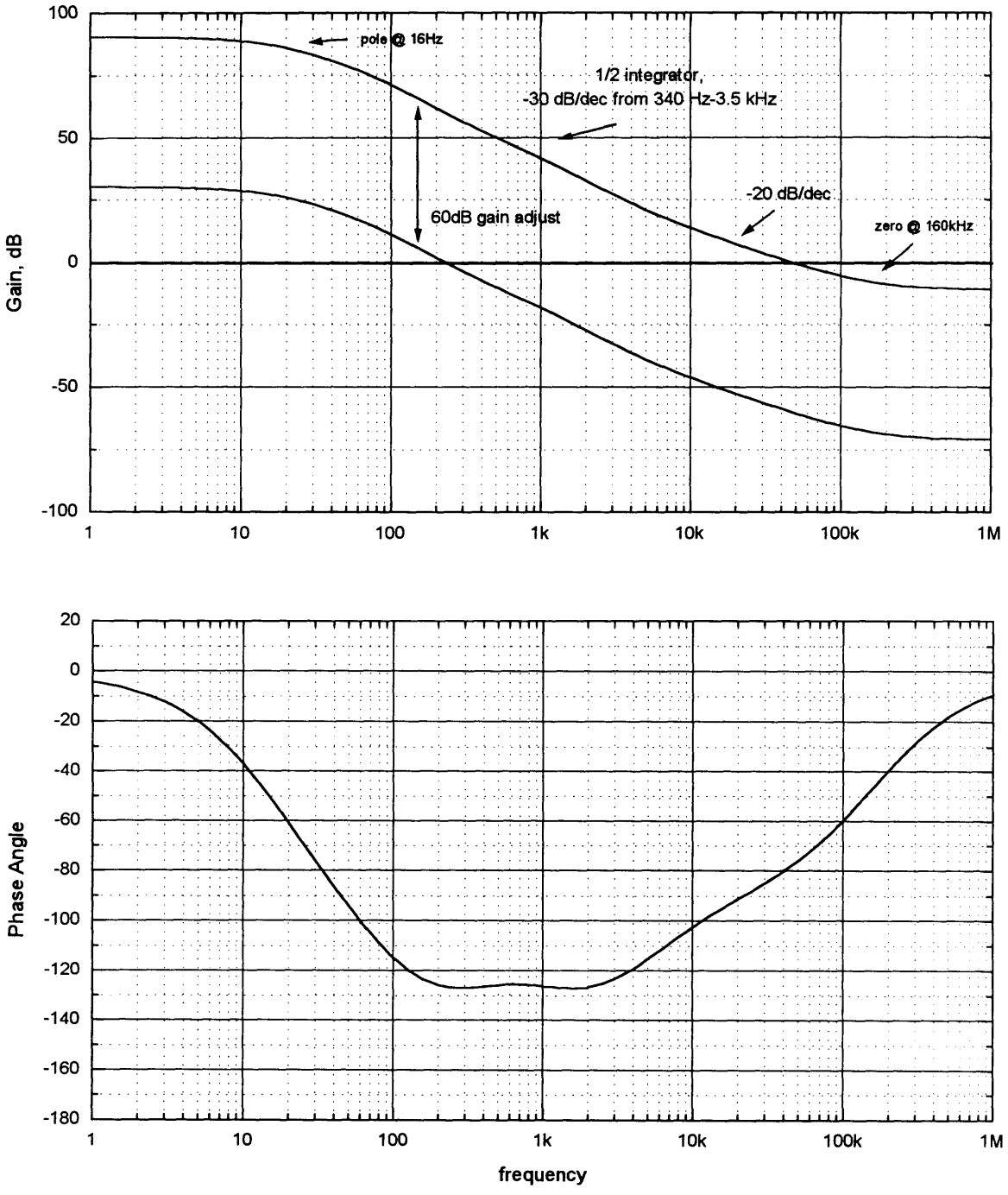

Figure 5.13: Frequency response of OPO stabilization error signal conditioning electronics (including PZT driver amplifier gain).

sloped side of the peak that resulted in negative feedback for the loop. The PZT DC bias was further fine-tuned to insure a zero mean output error signal from the conditioning electronics. The loop gain was increased using either the adjustment on the conditioning electronics or the PZT amplifier to minimize the residual fluctuations of the photodetector output. The DC photodetector output was fine-tuned (typically to .5 V, or 1 mA of photocurrent) by adjustment of the reference setpoint for the lock.

One anomaly became immediately apparent on locking the OPO cavity. As discussed earlier, the pump resonator cavity lock resulted in a $\pm .5$ nm fluctuation at predominantly twice the dither frequency (20 kHz). Given the OPO oscillation mode linewidth of 1.7 nm, this constituted a $\pm 30\%$ fluctuation around the OPO cavity lock-point (Fig. 5.8). Using an OPO resonance peak of 1 V (2 mA) and a straight-line (triangular) approximation for the cavity mode, a 60% peak-to-peak fluctuation resulted in a 600 mV peak-to-peak 20 kHz fluctuation around the lock-point, which was indeed observed on the photodetector output. These fluctuations were exactly in phase for both the signal and idler outputs, so in theory they would be eliminated by the common mode rejection of the AC differencing amplifier used for the measurement of intensity correlation (to be explained later). However, due to the frequency response of the AC portion of the photodetector circuit (Fig. 5.14, 12 dB gain at 20 kHz) these signals were nearly saturating the amplifiers in the respective photodetector circuits (± 5 V max output). The 20 dB/decade roll-off of the AC amplifiers below ~ 30 kHz suggested that this problem might be circumvented by choosing a lower dithering frequency. While this was investigated, the 10 kHz dither proved to be the optimal compromise between a modulation frequency low enough for the PZT to respond to, yet high enough so as not to be inadvertently conditioned by the dither error signal electronics.

A "bypass" technique was therefore employed to reduce the residual fluctuations of the photodetector signal. The "pre-integration" monitor output of the

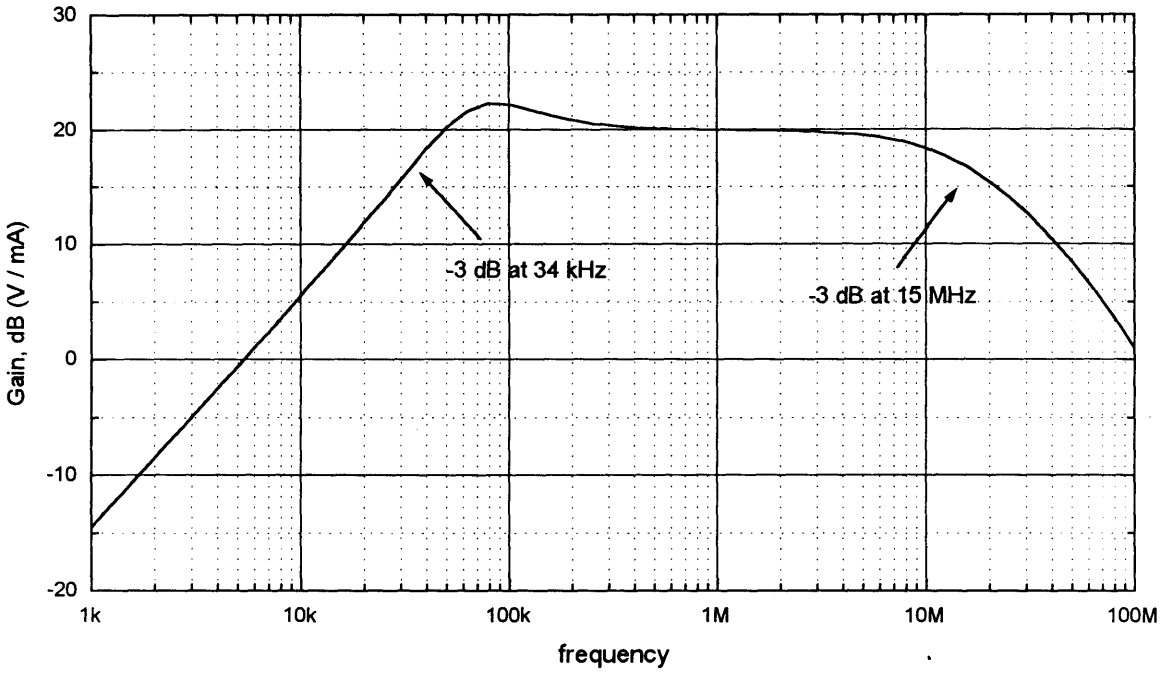

Figure 5.14: Photodetector amplifier AC circuit frequency response.

conditioning electronics, which essentially was the photodetector output minus the DC component, was fed directly to the PZT amplifier (Fig. 5.12) via the auxiliary input which had an adjustable gain from .3 to 1.5 V/V (a gain of 1 implied 600 $mV_{p-p} \times .8$ nm/V = .48 nm PZT movement). The sign of the signal was 180° out of phase with the photodetector output. In this manner, the PZT directly responded to the 20 kHz residual fluctuations in a nearly negative feedback manner (taking into consideration the propagation and actuation delays of the loop), and the residual fluctuations were substantially reduced. Fig. 5.15 shows the resulting photodetector output and conditioned error signal for the locked OPO, where it can be seen that the 20 kHz fluctuations were reduced to $\sim$200 mV_{p-p}, thereby avoiding saturation of the AC photodetector amplifier.

While the OPO cavity lock was not as robust as the pump resonator lock, the OPO could be stabilized for several minutes provided that ambient disturbances were kept to a minimum. Low pass filtering (BW < 10 kHz) of the photodetector output to

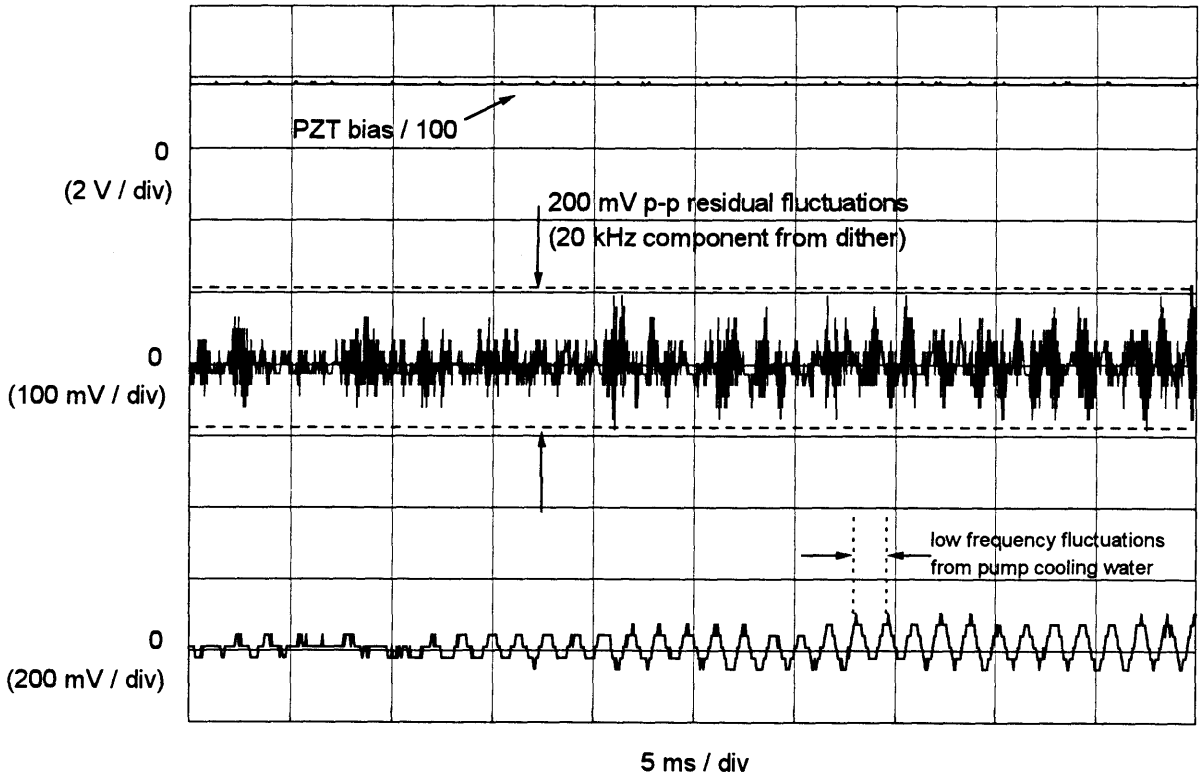

Figure 5.15: Monitoring the locked OPO cavity. Top trace (2 V/div) shows PZT bias voltage divided by 100 (bias set at ~175 V). Middle trace (100 mV/div) shows pre-integration monitor output. This is the zero-mean photodetector output signal after comparison with the reference voltage setpoint (lock-point). Residual 20 kHz fluctuations due to pump resonator cavity dither are reduced to ~200 mV peak-to-peak by a feed-forward technique. Bottom trace (200 mV/div) shows conditioned error signal which drives PZT amplifier. Fluctuations are on the order of 500 Hz, primarily due to water cooling of the pump source.

remove the residual dither fluctuation showed that within the servo loop bandwidth (unity gain frequency on the order of 5 kHz, from Fig. 5.13), the system could be stabilized to within 1.5% of the lock-point (7 mV_{rms} fluctuations at ~500 Hz with a .5 VDC photodetector output).

5.5 Detection Efficiency

All of the elements in the optical beam path from the OPO output to the photodetector amplifier were characterized for loss in order to accurately determine the detection efficiency η which appears in Eq. (4.2) for the intensity correlation spectrum. Much in the same manner as the direct component measurements outlined in Ch. 4, an Amoco Nd:YAG laser at $\lambda = 1.064\mu$m was used as a source to measure the reflected and/or transmitted light from or through a component to determine its loss. Fig. 5.16 shows a detail of the OPO output detection scheme used in the experiment.

All optical components were anti-reflective (AR) coated at $\lambda = 1.064$ μm. The components common to both horizontal (p) and vertical (s) output polarizations were a half-wave plate ($\lambda/2$), a focusing lens and a polarizing beam-splitter (PBS). The transmitted p-wave through the PBS was incident on a highly reflective mirror coated to optimize reflection of the p-polarization at a 45° incident angle. The p-wave was then incident on the photodetector, which was oriented at Brewster's angle to minimize reflection (for glass, at normal incidence the reflected power is ~5% [14, pg. 34]). While this should essentially eliminate reflection, in practice two reflections were observed, one from the glass cover of the photodetector and another from the photodetector surface. An optimal angle of incidence in the vicinity of Brewster's angle was therefore empirically determined, which reduced the reflected power by ~4% from normal incidence. In a similar fashion, the reflected s-wave from the PBS was incident on a highly reflective mirror coated to optimize reflection of the s-polarization at a 45° incident angle. The s-wave subsequently passed through

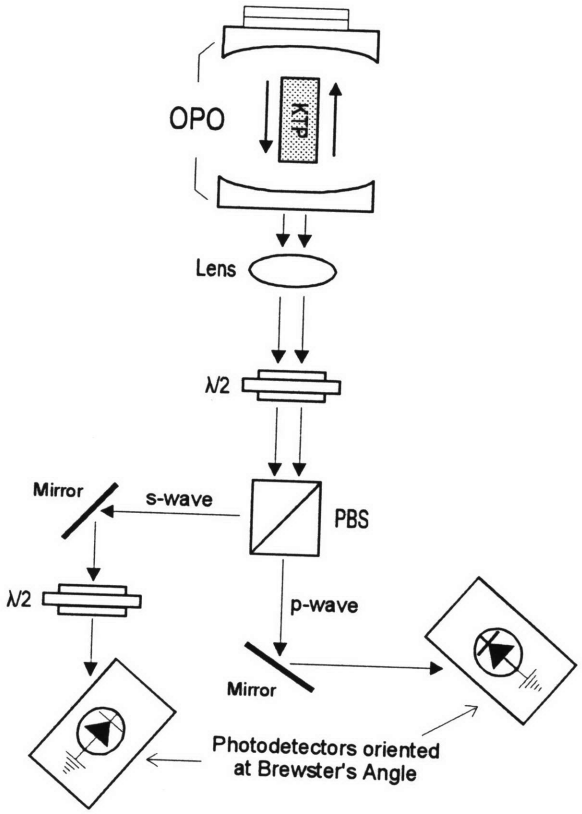

Figure 5.16: Detail of the OPO output detection scheme.

another half-wave plate ($\lambda/2$) such that its polarization was rotated 90°, resulting in a p-polarization. Thus the detector for this output could also be oriented near Brewster's angle to minimize reflection.

The photodetector efficiencies were measured as follows: for perfect (100%) efficiency, the photodetector efficiency in A/W is given by

$$\text{Energy of photon} = \frac{hc}{\lambda} = \frac{(6.632 \times 10^{-34}\ \text{J} \cdot \text{s})(3 \times 10^{8}\ \text{m/sec})}{1.064 \times 10^{-6}\ \text{m}} = 1.87 \times 10^{-19}\ \text{J}$$

$$\frac{1\ \text{photon}}{1.87 \times 10^{-19}\ \text{J}} \times \frac{1\ \text{electron}}{1\ \text{photon}} \times \frac{1.6 \times 10^{-19}\ \text{Coulombs}}{1\ \text{electron}} = .8556\ \text{A/W},$$

where h is Planck's constant. Power from the Nd:YAG source was measured with a Newport model 818-IR detector attached to a Newport model 835 power meter. This instrumentation comprised a wavelength selectable matched calibrated pair for sensitive reliable low power readings. The linearly p-polarized source was then focused directly onto the photodetectors positioned at approximately Brewster's angle. The DC output of the photodetector transimpedance amplifier (±.5 V/mA) was measured, and the photodetector efficiency determined in units of A/W was compared to the unity quantum efficiency value of .8556 A/W. Several measurements were taken for each detector while optimizing the angle of incidence, with the average value of the detector to be used for the p-polarization equal to .7836 A/W and the detector to be used for the s-polarization equal to .7776 A/W, corresponding to 91.6% and 90.9% efficiency, respectively.

Table 5.2 summarizes the results of the optical detection chain efficiency η in terms of fractional transmission through optical components and photodetector efficiency. The average efficiency of the s-polarization and p-polarization values was used in the theoretical determination of intensity correlation.

Component	**Efficiency**	
	s-polarization	p-polarization
Half-wave Plate (at 0°)	.999	.9998
Focusing Lens	.9994	.9994
Polarizing Beam Splitter	.988	.977
45° Mirror	.99998	—
	—	.9999965
Half-wave Plate (s-wave)	.999	—
Detectors	.909	—
	—	.916
Total Detection Efficiency, η	**.89574**	**.89421**
Average of both polarizations: η_{avg} = .89498		

Table 5.2: Summary of optical detection chain efficiency.

5.6 AC Signal Processing

The AC signal processing for the measurement of intensity correlation consisted of the photodetector AC amplifiers and a differencing amplifier (Fig. 5.1). The photodetector AC amplifier circuitry has already been shown in Fig. 5.10 and its frequency response shown in Fig. 5.14. One of the primary considerations for the AC detection circuitry was to keep the electronic noise as low as possible to get the best dynamic range; particularly, the electronic noise had to be sufficiently below the expected shot noise level from the combined photodetector currents so that intensity correlation could be accurately observed. The reader is referred to [28, 16] for a detailed study of noise calculations for the types of detection circuits used in this experiment, including the implications of specific photodiode properties. Here we summarize the important results.

The photodiode chosen was an Epitaxx 1000T InGaAs PIN photodiode, whose

Quantum Efficiency, η	$> 90\%$
Power Dissipation	100 mW
Bandwidth	70 MHz into a 50Ω load
Active Diameter	1 mm
Junction Capacitance	120-130 pf, unbiased 30 pf, reverse biased in excess of 15 V

Table 5.3: Properties of Epitaxx 1000T photodiode.

properties are given in Table 5.3. The large active area of the photodiode allowed high optical power absorption with little concern for local saturation. The operational amplifier selected for the AC circuitry was the Comlinear CLC425, chosen for its high gain-bandwidth product (1.7 GHz) and low noise characteristics. This amplifier was extremely sensitive to stray capacitances for high frequency operation however, and great care was taken in circuit design and assembly to minimize any adverse effects while maximizing circuit bandwidth.

In order to match the frequency characteristics of the CLC425 amplifiers used in the photodetection amplification circuitry, this same chip was used to perform the differencing operation used for the measurement of intensity correlation. Fig. 5.17 shows the schematic of the differencing amplifier used to subtract the two AC photodetector signals. This circuit was essentially an inverting summing amplifier, where the photodetector inputs were 180° out of phase due to the inverted polarity of the photodetector transimpedance amplifiers. One of the detector input channels was equipped with a 4 dB gain adjustment pot to allow for equalizing the channel signals to obtain the maximum common mode rejection. The common mode rejection was frequency sensitive, and therefore this "channel balance" adjustment was optimized for the measurement frequency of interest, as explained in the next section. Each input channel also contained a passive high-pass filter circuit to attenuate the excess

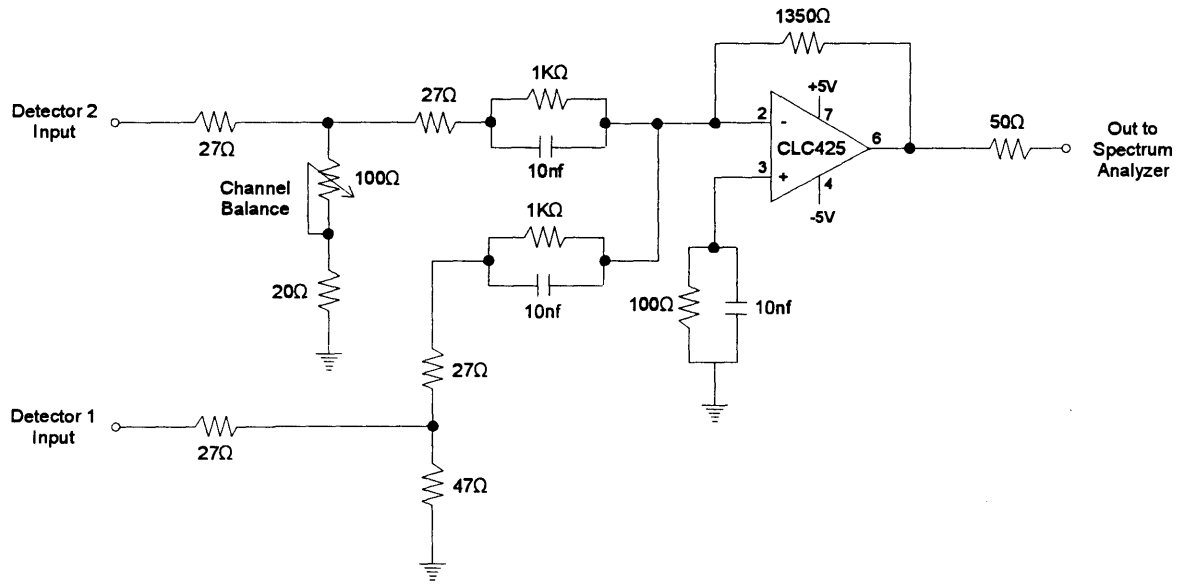

Figure 5.17: Schematic of differencing amplifier circuit.

low frequency pump laser noise (Ch. 3) below 200 kHz. The in-band nominal amplifier gain (including impedance matching from the photodetector amplifiers) was 9.1 V/V (19.2 dB) from 1 to 10 MHz. Fig. 5.18 shows the frequency response of the differencing amp circuitry.

Fig. 5.19 shows the electronic noise floor of the combined AC photodetector and difference amplifier circuits for each detector. All noise measurements were made with a Hewlett-Packard model HP8563E spectrum analyzer with a resolution bandwidth of 10 kHz. The noise floors were compared to a white-light generated shot noise power with 2 mA of DC photocurrent, which was equivalent to the maximum total photocurrent expected from the OPO outputs. The theoretical shot noise level was calculated as follows; the rms shot noise photocurrent from 2 mA of DC photocurrent is given by

$$i_{sn} = (2eI_{DC})^{1/2}$$

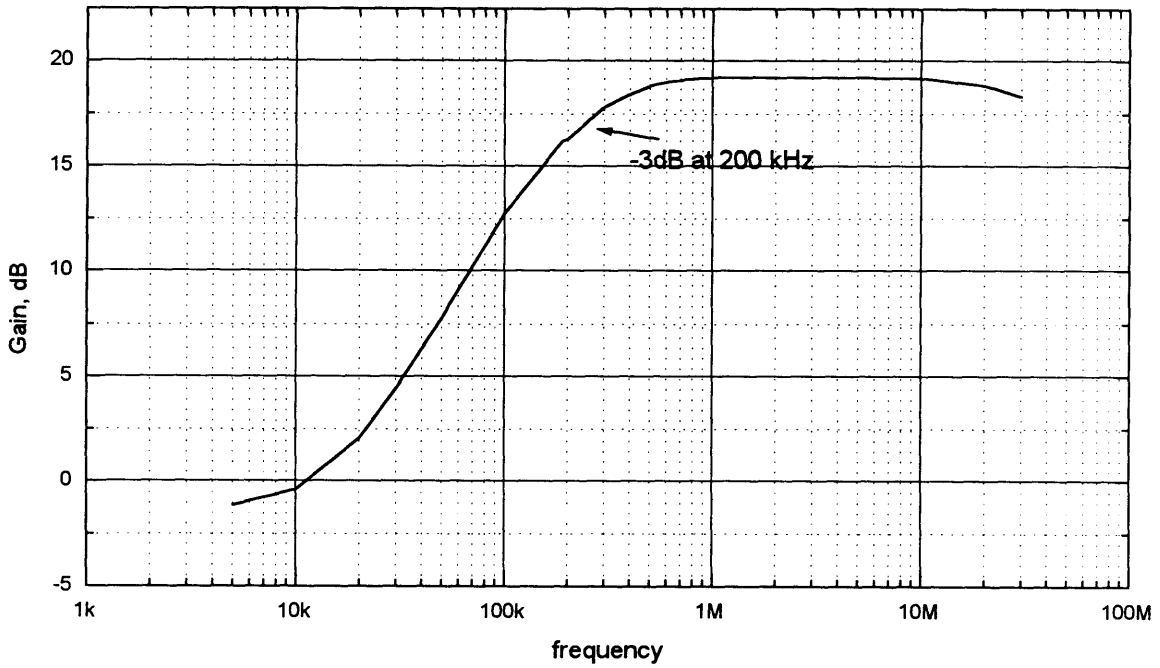

Figure 5.18: Frequency response of differencing amplifier circuitry.

$$= [(2)(1.6 \times 10^{-19})(2 \times 10^{-3})]^{1/2}$$
$$= 2.53 \times 10^{-11} \frac{A_{rms}}{\sqrt{Hz}}.$$

This rms shot noise current flowed to a transimpedance amplifier with a gain of 10 V/mA (Fig. 5.10), then to the differencing amplifier which had a per channel gain of 9.1 V/V. The output was monitored by a spectrum analyzer with a 50Ω input impedance, hence an impedance matching factor of .5 V/V:

$$2.53 \times 10^{-11} \frac{A_{rms}}{\sqrt{Hz}} \times 10 \frac{kV}{A_{rms}} \times 9.1 \frac{V}{V} \times .5 \frac{V}{V} = 1.1512 \times 10^{-6} \frac{V_{rms}}{\sqrt{Hz}}.$$

This was converted to milliwatts across the 50Ω input load of the spectrum analyzer:

$$P\ (mW/Hz) = \frac{(V_{rms}/\sqrt{Hz})^2}{50\Omega} \times 1000$$
$$= 2.65 \times 10^{-11}\ mW/Hz.$$

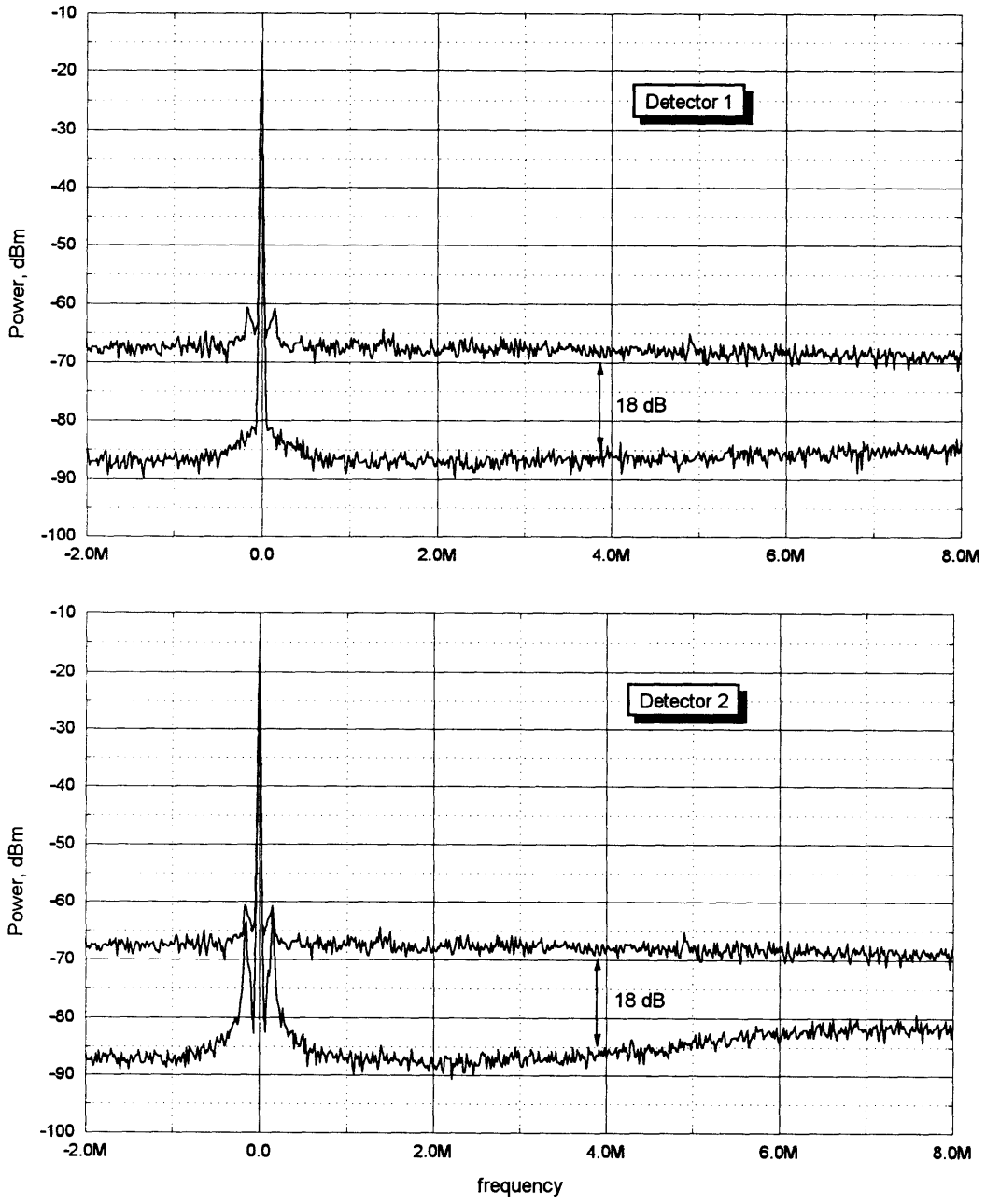

Figure 5.19: Electronic noise floor of AC signal processing circuitry compared to white light generated shot noise power for total DC photocurrent of 2 mA.

The power spectral density in dBm/Hz is then given by

$$\begin{aligned} PSD &= 10\log(\mathrm{mW/Hz}) \\ &= -105.77\ \mathrm{dBm/Hz}. \end{aligned}$$

From Fig. 5.19, it can be seen that the white light shot noise level was observed to be -105.8 dBm/Hz at 4 MHz, in excellent agreement with the calculated value. With a spectrum analyzer resolution bandwidth of 10 kHz, this is equivalent to a noise power of -65.8 dBm. The actual noise power reading for the shot noise was -66.3 dBm. The spectrum analyzer had the capability of reporting the noise power either in terms of the power spectral density or power; power spectral density was calculated based on an average of points around the measurement frequency of interest, while power was displayed with a quoted accuracy of ± 0.5 dB. It can also be seen that for both detectors, while the respective electronic noise signatures differed, the shot noise level was 18 dB above the electronic noise floor at 4 MHz, affording good dynamic range for the intensity correlation measurement.

Linearity and saturation of the photodetectors and associated AC electronics was additionally examined using both a white-light and Nd:YAG laser source. Through shot noise measurements, both detectors and electronics were found to be linear up through DC photocurrents of 8 mA per detector, well beyond the expected levels of operation for the experiment. The saturation power level could not be determined due to the limited power of the test sources.

5.7 Intensity Correlation Measurement

As mentioned earlier, the balance of the AC differencing network was critical to the observable degree of correlation, and the common-mode rejection of the electronics was observed to be frequency dependent. Therefore, once a stable continuous-wave

OPO output was obtained, the signal and idler balance was initially adjusted using amplitude modulation of the pump source. The measurement frequency range of interest was from 3 to 5 MHz; this was well within the cavity bandwidth (17.8 MHz, Table 4.3), the electronic circuitry bandwidth (flat from 1 to 5 MHz, Fig. 5.14) and just above where the excess pump noise approached the shot noise limit. Sinewave test signals from a signal generator from 3 to 5 MHz (on the order of -30 dBm) were input to the auxiliary input of the pump intensity servo signal conditioning electronics (Fig. 3.1). With one detector blocked, the OPO cavity was locked to the unblocked detector output, and the lock-point was adjusted for 2 mA of DC photocurrent. The power level of the amplitude modulation for the frequency of interest was noted by observing the output of the differencing network on the spectrum analyzer. Subsequently, the other detector was unblocked and the lock-point readjusted for a *total* DC photocurrent of 2 mA (1 mA per detector). Again, the modulation frequency power was observed and the channel balance adjusted to minimize this power (maximize the common-mode rejection). While the exact positioning of the adjustment pot differed for different frequencies, 33 dB of suppression was observed for 3 MHz modulation, while 31 dB of suppression was observed for 5 MHz modulation. The channel balance was further fine-tuned during the intensity correlation measurement by maximizing the observed reduction at the frequency of interest, typically 4 MHz.

A subtle consequence of the channel balance adjustment was to alter the expected shot noise power from the summed AC photocurrents. As shown earlier, a "baseline" expected value for the shot noise from 2 mA total DC photocurrent using a fixed gain for both channels of the differencing amplifier was -105.77 dBm/Hz. As a system check, once an initial optimization of channel balance was completed, white-light sources as well as the Nd:YAG laser were used to verify the shot noise level for 2 mA total photocurrent. Both of these measurements compared to within ~0.5 dB of the theoretical value at 4 MHz.

Ultimately however, the intensity correlation measurement was compared to

the shot noise level generated by "mixing" the signal and idler outputs via a half-wave plate as described in Sec. 5.2. This shot noise level also compared to within ~0.5 dB of the theoretical value at 4 MHz. The primary difference amongst the three comparative shot noise measurements was the low frequency noise. While the white-light measurement was essentially flat across the spectrum from 1 to 10 MHz (with the exception of a subtle downward slope due to the roll-off of the electronics), the low frequency noise signature of the Nd:YAG was substantially different than that of the pump laser source. These differences were exacerbated by the frequency dependent common-mode rejection of the differencing amplifier, resulting in incomplete cancellation of the laser noise. All sources agreed well for frequencies above 3 MHz.

Fig. 5.20 shows a broadband intensity correlation measurement compared to the "mixed" signal and idler shot noise level, which was achieved by rotation of the half-wave plate in the output path. The channel balance was optimized for maximum correlation at 4 MHz. At this frequency, the shot noise was measured to be -105.5 dBm/Hz while the correlation spectrum yielded -110.5 dBm/Hz, indicating a 5 dB reduction below the shot noise level (~70% correlation). Several measurements of this type were made, with reductions ranging from 4.5 to 5.5 dB, depending on the particular cavity mode that was locked to. This suggested that the cavity losses were sensitive to mode position and beam path, which was not unreasonable. In addition, thresholds were periodically monitored and varied between approximately 50 and 70 mW. The cavity was pumped at approximately 80 to 100 mW. Fig. 5.21 shows another measurement with both the vertical and horizontal scales expanded. For this measurement, the channel balance was fine-tuned for maximum reduction at 3 MHz, which in turn slightly altered the shot noise level by ~0.5 dB. The observed reduction was 5.5 dB at 3 MHz and 4.9 dB at 4 MHz.

Fig. 5.22 compares the broadband results to the theoretical predicitions. Appendix F shows a Mathcad [1] program for the model used to generate the the-

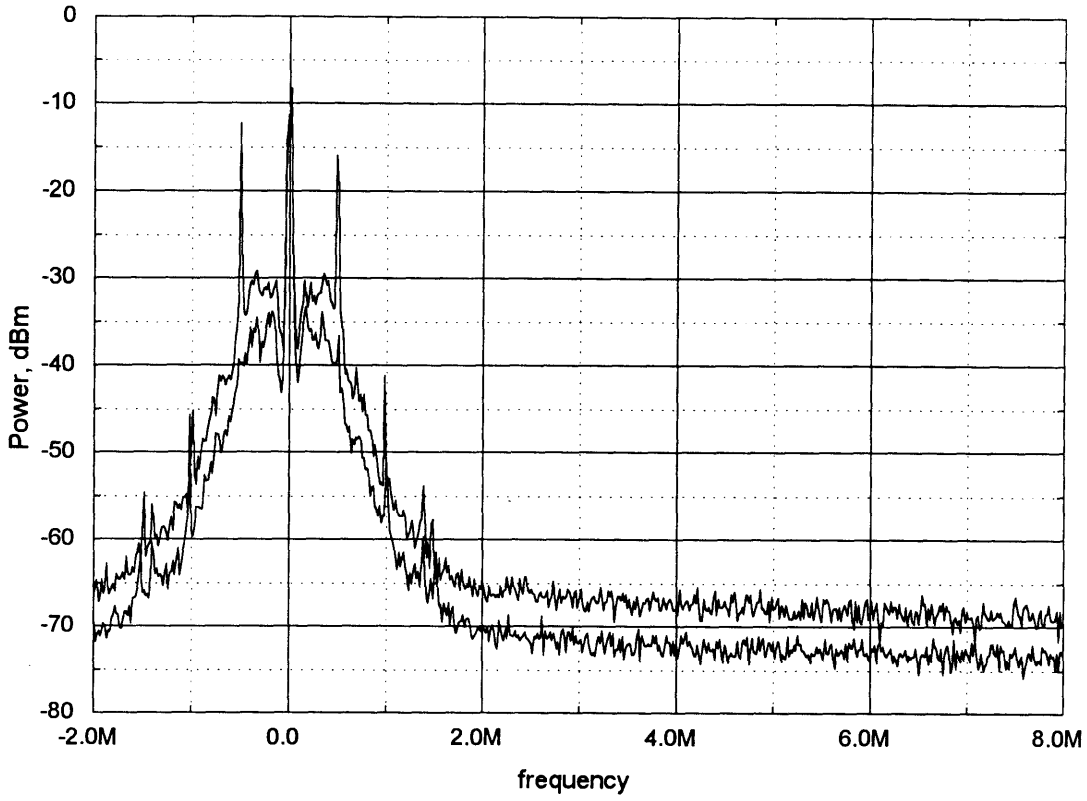

Figure 5.20: Intensity correlation spectrum compared to "mixed" signal and idler generated shot noise. Top trace: shot noise, -105.5 dBm/Hz at 4 MHz. Bottom trace: correlation spectrum, -110.5 dBm/Hz at 4 MHz, indicating 5 dB of reduction ($\sim$70% correlation). Total DC photocurrent = 2.024 mA. OPO threshold was $\sim$60 mW and pumped at $\sim$80 mW. Resolution bandwidth of spectrum analyzer was 10 kHz.

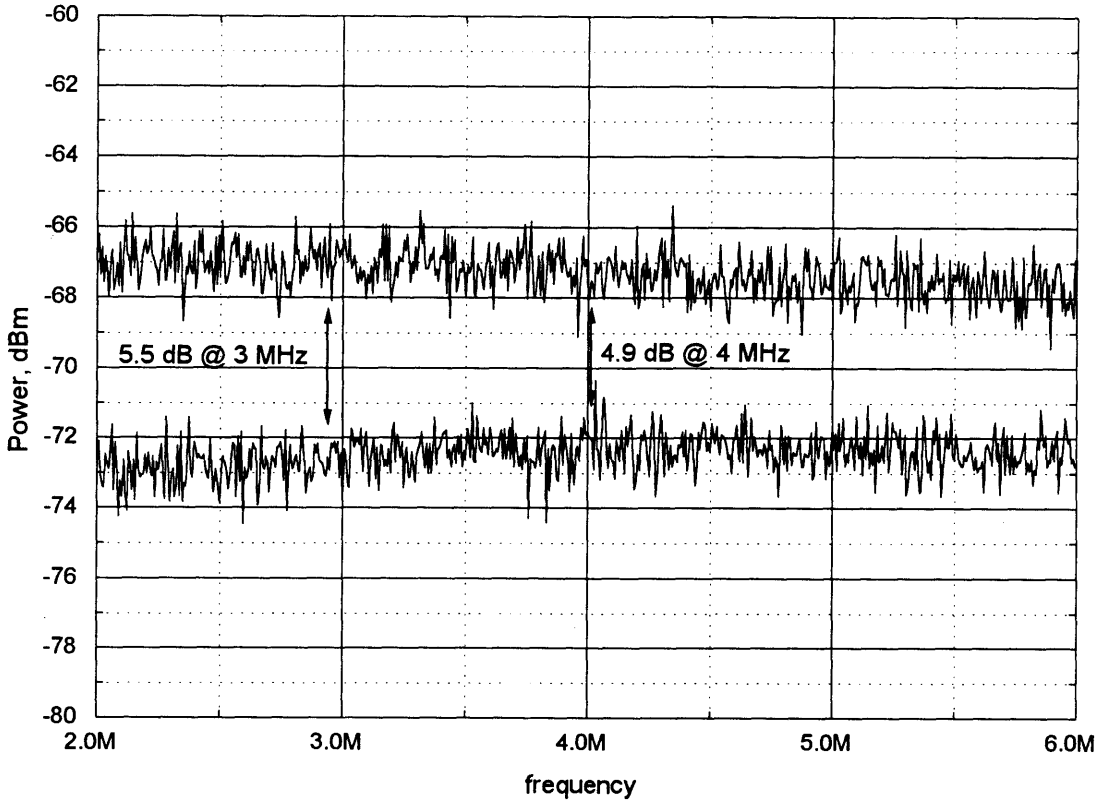

Figure 5.21: Intensity correlation spectrum, expanded scale. Top trace: shot noise from "mixed" signal and idler. Bottom trace: intensity correlation spectrum, 5.5 dB below shot noise at 3 MHz, 4.9 dB below shot noise at 4 MHz.

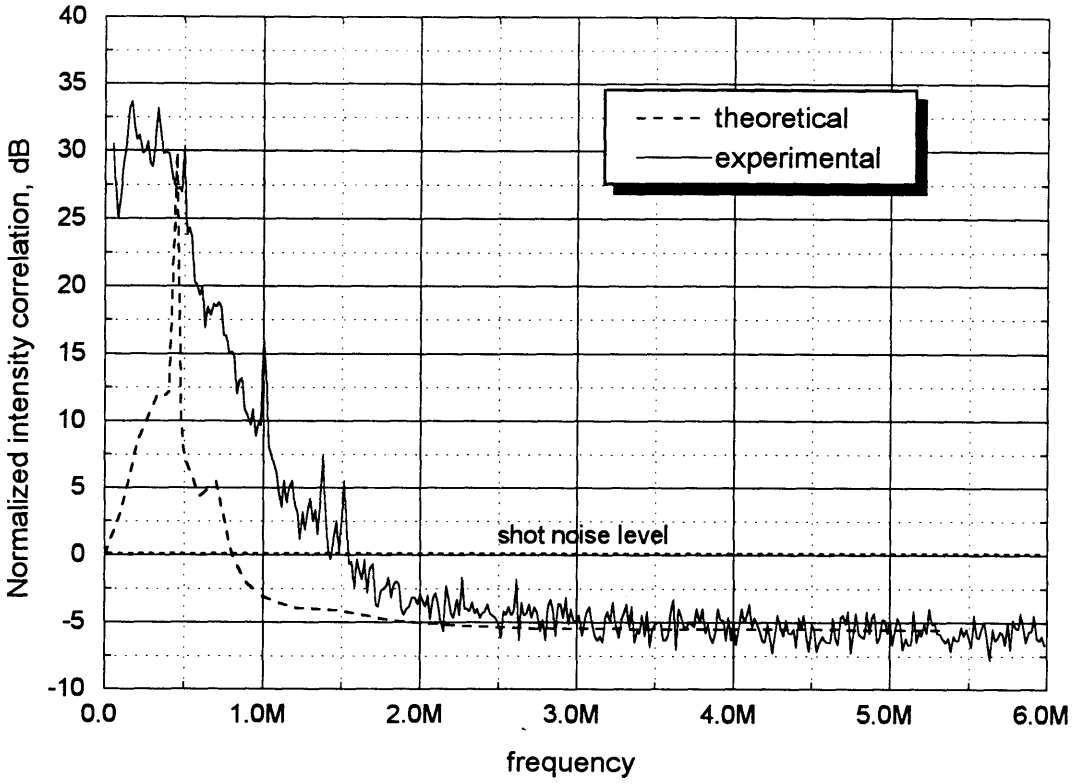

Figure 5.22: Comparison of theoretical model to experimental results for intensity correlation spectrum, normalized to shot noise level. Model predicts 5.49 dB of reduction at 4 MHz. Excess low frequency noise of experimental results is due to imbalance of differencing amplifier at those frequencies (balance was optimized for 4 MHz).

oretical benchmark data. This model is from the treatment in [39] (as discussed in Sec. 2.7), which takes into consideration both the presence of the excess pump noise (Fig. 3.15) as well as the cavity loss mismatches between the signal and idler beams (Table 4.2). Other parameters of consideration included the cavity loss for the pump, the total detection efficiency and the ratio of pumping power to oscillation threshold. The model generated the intensity correlation spectrum normalized to the shot noise. A reduction of 5.49 dB below shot noise was predicted at 4 MHz.

In order to obtain normalized experimental data, the theoretical shot noise was subtracted from the broadband spectrum. This tended to induce a small error (less than 0.5 dB from 3 to 5 MHz) in the normalized result due to the subtle roll-off at high frequencies of the experimental shot noise level. Nevertheless, this method served well for illustrative purposes. Excellent agreement between the theoretical and experimental data was observed at frequencies above 3 MHz. Below 3 MHz, the excess low frequency noise of the experimental results was due to the imbalance of the differencing amplifier at those frequencies, as a result of the common-mode rejection being optimized for a measurement at 4 MHz. Despite this, one could still observe a similar profile to that of the theoretical prediction at low frequencies, including a large spike of excess pump noise at ~400 kHz.

5.8 Summary

In this chapter, we have discussed the details of stabilizing the triply-resonant OPO system in order to achieve continuous-wave output, with particular emphasis on the supporting electronic circuitry. The detection efficiency of all optics in the output beam path, including the photodetector, was accurately determined. The detection and signal amplification circuitry were characterized for noise and frequency response, and the theoretical value for shot noise was verified experimentally using both white-

[1] Mathcad is a registered trademark of MathSoft, Inc., Cambridge, MA.

light and Nd:YAG laser sources. Finally, several intensity correlation measurements were performed and compared to the theoretical model. Intensity noise reduction on the order of 5 dB below the shot noise level was observed at 4 MHz, in excellent agreement with the theoretical prediction.

Chapter 6
Conclusion

6.1 Summary

A four-piece three-mirror triply-resonant OPO was designed, constructed, characterized and used to generate intensity correlated twin beams. The pump laser was intensity and frequency stabilized and the excess pump noise spectrum was characterized. The lengths of the two cavities comprising the OPO system were stabilized to provide stable continuous-wave outputs. The photodetection and signal processing electronics had a bandwidth of 10 MHz, low electronic noise and demonstrated linearity up to 8 mA of white-light generated photocurrent were obtained. This system was used to generate an intensity correlation spectrum which revealed $\sim$5 dB reduction below the shot noise level at 4 MHz. The experimental results were in excellent agreement with the calculated value from a rigorous theoretical model using the measured system parameters.

6.2 Future Work

The current experimental benchmark for intensity correlation is given by Mertz, *et. al.* [27] where a quantum noise reduction of 8.5 dB (86% correlation) was observed near 3 MHz in a doubly-resonant OPO with a double-pass pump and an output coupler of $T = 6.8\%$. Several improvements can be made to the research herein to approach and perhaps exceed this benchmark.

The primary limiting factor toward observing increased correlation are the cav-

ity losses due to the crystal. The crystal may undergo several aging effects with use, including deterioration of the anti-reflective coatings on the end-faces, and internal damage due to the concentration of power in the small area of a beam path. It is recommended therefore that the crystal be displaced laterally in the cavity and the system realigned so that an "unused" portion of the crystal may be used for further measurements. Also, significant heating of the crystal (up to 150°C) may repair any photorefractive damage incurred by the crystal. Any improvements in the crystal losses will reduce the oscillation threshold while increasing correlation.

While many of the elements in the OPO output beam path have superior transmission qualities, two improvements are possible that would increase the detection efficiency. First, the polarizing beam splitter used to separate the signal and idler outputs may be replaced with one having lower losses for both the p (transmitted) and s (reflected) polarizations. Second, while the photodetector angles have been optimized for minimal reflection near Brewster's angle, there is nonetheless some reflection from both the glass cover of the photodetector and the photodetector surface. This light may be re-reflected and focused back onto the photodetectors via highly reflective mirrors.

Additionally, pumping the OPO at a higher power will reduce the effects of signal and idler loss mismatches and excess pump noise. If the present output coupler of $T = 2.7\%$ is maintained, and we assume a decrease in extraneous cavity losses to $\sim 0.3\%$, a decrease in polarizing beam splitter losses and photodetector losses from reflection such that the total detection efficiency is increased to 95%, and pumping at 2 times above threshold, noise reduction in excess of 8 dB below shot noise may be observed. Appendix F shows theoretical correlation spectra using the above values, where a slight signal/idler loss mismatch is represented (3% total losses for p-polarization, 2.9% total losses for s-polarization). The resulting simulation indicates 8.6 dB of reduction at 3 MHz. Of course, another possibility is to replace the output coupler with a more highly transmissive mirror, at the expense of a higher oscillation

threshold.

The development of such a twin-beam generator allows the study of a wide variety of quantum noise phenomena, such as an injection-seeded optical parametric amplifier operating in the saturated gain regime [38]. An additional area for future work is given by applications based on precision optical absorption spectroscopy [39].

Appendix A

The Nonlinear Wave Equation

In this appendix, the classical nonlinear wave equation is derived in terms of a general nonlinear polarization for nonmagnetic materials. The fields will be assumed to be quasi-monochromatic plane waves. When solved using suitable approximations and appropriate boundary conditions, an equation is obtained that is applicable to a variety of nonlinear interactions. We are particularly interested in second order nonlinear processes, namely parametric down-conversion, which is developed in Ch. 2 using the results here. The developments of this appendix follow closely those given in reference [17].

Maxwell's equations in mks units are given by

$$\nabla \times \mathbf{E} = -\frac{\partial \mathbf{B}}{\partial t} \tag{A.1}$$

$$\nabla \times \mathbf{H} = \frac{\partial \mathbf{D}}{\partial t} + \mathbf{J} \tag{A.2}$$

$$\nabla \cdot \mathbf{D} = \rho \tag{A.3}$$

$$\nabla \cdot \mathbf{B} = 0 \tag{A.4}$$

with the constitutive relationships

$$\mathbf{B} = \mu_o \mathbf{H} \tag{A.5}$$

$$\mathbf{J} = \sigma \mathbf{E} \tag{A.6}$$

$$\mathbf{D} = \epsilon \mathbf{E}$$

$$= \epsilon_o (1 + \chi) \mathbf{E}$$

$$= \epsilon_o \mathbf{E} + \mathbf{P} \tag{A.7}$$

where in general ϵ, μ, σ, and χ are tensor quantities.

The simplest picture of an electromagnetic field interacting with an atom consists of an electron being pulled away from the nucleus by the force generated from the **E**-field's interaction with the charged electron, thus generating the polarization term **P** in Eq. (A.7). This force is oppositely directed to that of the (assumed to be linear) restoring force provided by the nucleus. Solution of the classical equations would yeild simple harmonic motion resulting in re-radiation at the same frequency as the driving field. If however the electric field is quite strong, as might be generated by a laser, then the excursions of the electrons from their equilibrium positions would be comparably large, and the restoring force would no longer be considered linear. In this case, one would expand the polarization term as a power series in **E**:

$$\mathbf{P} = \epsilon_o \mathbf{E}(\chi^{(1)} + \chi^{(2)}\mathbf{E} + \chi^{(3)}\mathbf{E} \cdot \mathbf{E} + \text{higher order terms}). \tag{A.8}$$

The first term in this expansion is linear and gives rise to the commonly known dielectric constant. It is the second term with nonlinear susceptibility $\chi^{(2)}$ that is of interest in the process of down-conversion. Higher order terms are always present but significantly weaker than the second order term. In general though, we may define a nonlinear polarization term which includes all higher order terms such that Eq. (A.7) may be expressed as

$$\mathbf{D} = \epsilon \mathbf{E} + \mathbf{P_{NL}} \tag{A.9}$$

where, for second order $\chi^{(2)}$ processes in particular

$$\mathbf{P_i^{(2)}} = \hat{\mathbf{p}}_\mathbf{i}\ \epsilon_o \sum_{jk} \chi_{ijk}^{(2)} \mathbf{E_j E_k}. \tag{A.10}$$

In practice, the tensor quantity $\chi^{(2)}$ is replaced by the *effective nonlinear coefficient*,

d_{eff}. This is discussed in Appendix B.

Proceeding in the development of the wave equation, the curl of Eq. (A.1) is taken, with the substitution of Eq. (A.5)

$$\nabla \times \nabla \times \mathbf{E} = -\mu_\circ \frac{\partial(\nabla \times \mathbf{H})}{\partial t}. \tag{A.11}$$

Using the vector identity $\nabla \times \nabla \times \mathbf{E} = \nabla(\nabla \cdot \mathbf{E}) - \nabla^2\mathbf{E}$ and substituting Eqs. (A.2) and (A.6) yeilds

$$\nabla(\nabla \cdot \mathbf{E}) - \nabla^2\mathbf{E} = -\mu_\circ \frac{\partial^2\mathbf{D}}{\partial t^2} - \mu_\circ\sigma\frac{\partial\mathbf{E}}{\partial t} \tag{A.12}$$

We assume no polarization charge density ($\rho = 0$), so that $\nabla \cdot \mathbf{E} = 0$ from Eq. (A.3). Introducing Eq. (A.9) and regrouping yields

$$\nabla^2\mathbf{E} - \mu_\circ\sigma\frac{\partial\mathbf{E}}{\partial t} - \mu_\circ\epsilon\frac{\partial^2\mathbf{E}}{\partial t^2} = \mu_\circ\frac{\partial^2\mathbf{P_{NL}}}{\partial t^2} \tag{A.13}$$

where each component of $\mathbf{P_{NL}}$ is given by Eq. (A.10) for second order processes. This is the nonlinear wave equation in terms of the real time-dependent quantities $\mathbf{E}$ and $\mathbf{P_{NL}}$. On the left hand side of Eq. (A.13) we see a freely propagating field being "driven" on the right by a time-varying nonlinear polarization. In the general tensorial case, this equation is quite difficult to solve. With suitable approximations a useful result is obtained while retaining the essential physics.

We assume non-tensor quantities, and make the slowly varying envelope approximation, writing the nonlinear wave equation in terms of the complex field envelopes, i.e., we write the time-dependent quantities as the product of a monochromatic plane wave (with propagation constant k and phase ϕ) and a slowly varying envelope:

$$\mathbf{E}(z,\omega,t) = \hat{\mathbf{e}}\, E(z,t)e^{-j(kz-\omega t+\phi)} \tag{A.14}$$

$$\mathbf{P_{NL}}(z,\omega_p,t) = \hat{\mathbf{p}}\, P_{NL}(z,t)e^{-j(k_pz-\omega_p t+\phi_p)} \tag{A.15}$$

where E and P_{NL} have a "slow" z and t dependence. Substitution of this approximation into Eq. (A.13) yields

$$\left[\frac{\partial^2}{\partial z^2} - 2jk\frac{\partial}{\partial z} - k^2 - \mu_o\sigma(\frac{\partial}{\partial t} + j\omega) - \mu_o\epsilon(\frac{\partial^2}{\partial t^2} + 2j\omega\frac{\partial}{\partial t} - \omega^2)\right] E(z,t)e^{-j(kz-\omega t+\phi)}$$
$$= (\hat{\mathbf{e}}\cdot\hat{\mathbf{p}})\mu_o(\frac{\partial^2}{\partial t^2} + 2j\omega\frac{\partial}{\partial t} - \omega^2)P_{NL}(z,t)e^{-j(k_pz-\omega_pt+\phi_p)}.$$

Recalling the dispersion relationship $k^2 = \mu_o\epsilon\omega^2$ and making the further approximations (under the slowly varying envelope approximation)

$$\begin{aligned}
\frac{\partial^2 E}{\partial z^2} &\ll k\frac{\partial E}{\partial z} \\
\frac{\partial^2 E}{\partial t^2} &\ll \omega\frac{\partial E}{\partial t} \ll \omega^2 E \\
\frac{\partial^2 P_{NL}}{\partial t^2} &\ll \omega_p\frac{\partial P_{NL}}{\partial t} \ll \omega_p^2 P_{NL}
\end{aligned}$$

yields

$$2jk\frac{\partial E}{\partial z} + j\mu_o\sigma\omega E + 2j\mu_o\epsilon\omega\frac{\partial E}{\partial t} = (\hat{\mathbf{e}}\cdot\hat{\mathbf{p}})\,\mu_o\omega^2 P_{NL}e^{j(\Delta kz+\Delta\phi)}$$

where $\Delta k = k - k_p$ and $\Delta\phi = \phi - \phi_p$. We will only be interested in cases where the field and the polarization have the same frequency ($\omega = \omega_p$) such that energy is conserved. Finally, we arrive at the complex amplitude nonlinear wave equation

$$\left(\frac{\partial}{\partial z} + \frac{n}{c}\frac{\partial}{\partial t}\right) E + \alpha E = -j\frac{\omega\mu_o c}{2n}(\hat{\mathbf{e}}\cdot\hat{\mathbf{p}})\,P_{NL}e^{j(\Delta kz+\Delta\phi)} \qquad \text{(A.16)}$$

where we have made the substitutions $n = \sqrt{\epsilon/\epsilon_o}$, $c = 1/\sqrt{\mu_o\epsilon_o}$ and $\alpha = \sigma\mu_o c/2n$ which represents the loss in the medium. The time derivative can be neglected in the steady state continuous wave analysis. For a particular nonlinear process it is necessary to work with a set of equations like (A.16) coupled by the nonlinear polarization P_{NL}, where an equation of this form would appear for each wave in the interaction.

Appendix B

The Effective Nonlinear Coefficient and Phase Matching

B.1 Origin of the Nonlinear Coefficient Tensor

In Appendix A we encountered a vector for the nonlinear polarization of a material, $\mathbf{P_{NL}}$, whose components drive the nonlinear wave equation (A.16). In this appendix, we more closely examine the nonlinear polarization, which couples fields in nonlinear interactions.

For second order nonlinear processes, we may write the vector

$$\begin{aligned} \mathbf{P}_{\mathbf{NL}}^{(2)} &= P_x^{(2)}\hat{\mathbf{x}} + P_y^{(2)}\hat{\mathbf{y}} + P_z^{(2)}\hat{\mathbf{z}} \\ &= \epsilon_o \overline{\overline{\chi}}^{(2)}(\mathbf{E_1} \cdot \mathbf{E_2}) \end{aligned} \tag{B.1}$$

where $\mathbf{E_1}$ and $\mathbf{E_2}$ are vector field quantities and $\overline{\overline{\chi}}^{(2)}$ is a 27 element tensor quantity (3×9 matrix) for the various second order nonlinear susceptibilities. From this relation, it can be seen that *each* component of $\mathbf{P}_{\mathbf{NL}}^{(2)}$ is linearly related to *all* possible component combinations of $\mathbf{E_1}$ and $\mathbf{E_2}$, and in the general case, $\mathbf{E_1}$ and $\mathbf{E_2}$ may have different frequencies. By multiplying these two fields, the sum or the difference of their frequencies can be obtained.

Since working through the math is a bit cumbersome, a standard notation has

been developed to describe each component of the nonliner polarization

$$\mathbf{P_i^{(2)}}(\omega_3) = \epsilon_o \sum_{jk} \chi_{ijk}^{(2)}(\omega_3 : \omega_1, \omega_2) E_j(\omega_1) E_k(\omega_2) e^{-j(\mathbf{k_1}+\mathbf{k_2})\cdot\mathbf{r}} \tag{B.2}$$

where the notation for $\chi_{ijk}^{(2)}(\omega_3 : \omega_1, \omega_2)$ implies a sum frequency generation process ($\omega_3 = \omega_1 + \omega_2$). This is essentially the inverse process of parametric down-conversion.

For historical reasons related to second harmonic generation, which is a sum frequency process given by $\omega_1 = \omega_2 = \omega$; $\omega_3 = 2\omega$, the second order nonlinear susceptibility is expressed in terms of the nonlinear constant d, given by the tensor elements

$$d_{ijk} = \frac{1}{2}\chi_{ijk}^{(2)}. \tag{B.3}$$

One further writes the d_{ijk}'s in reduced notation $d_{ijk} = d_{ikj} = d_{il}$ since jk are permutable for the second harmonic generation interaction. The reduced notation may be described by the correspondence

$$[jk] = \begin{bmatrix} 11 & 12 & 13 \\ 21 & 22 & 23 \\ 31 & 32 & 33 \end{bmatrix} = [l] = \begin{bmatrix} 1 & 6 & 5 \\ 6 & 2 & 4 \\ 5 & 4 & 3 \end{bmatrix}.$$

The polarization components $P_i^{(2)}$ from Eq. (B.2) are then determined in an x-y-z

coordinate frame for the material by

$$\begin{bmatrix} P_x(\omega_3) \\ P_y(\omega_3) \\ P_z(\omega_3) \end{bmatrix} = 2\epsilon_o \begin{bmatrix} d_{11} & d_{12} & d_{13} & d_{14} & d_{15} & d_{16} \\ d_{21} & d_{22} & d_{23} & d_{24} & d_{25} & d_{26} \\ d_{31} & d_{32} & d_{33} & d_{34} & d_{35} & d_{36} \end{bmatrix} \cdot \begin{bmatrix} E_x(\omega_1)E_x(\omega_2) \\ E_y(\omega_1 E_y(\omega_2) \\ E_z(\omega_1)E_z(\omega_2) \\ E_y(\omega_1)E_z(\omega_2) + E_z(\omega_1)E_y(\omega_2) \\ E_x(\omega_1)E_z(\omega_2) + E_z(\omega_1)E_x(\omega_2) \\ E_x(\omega_1)E_y(\omega_2) + E_y(\omega_1)E_x(\omega_2) \end{bmatrix}. \tag{B.4}$$

The nonlinear crystal used in this experiment, potassium titanyl phosphate (KTP) belongs to the $mm2$ orthorhombic symmetry class, and has the following nonlinear coefficient tensor [8]

$$d_{il} = \begin{bmatrix} 0 & 0 & 0 & 0 & d_{15} & 0 \\ 0 & 0 & 0 & d_{24} & 0 & 0 \\ d_{31} & d_{32} & d_{33} & 0 & 0 & 0 \end{bmatrix}.$$

In the reference frame of the crystal, this results in the components of the nonlinear polarization from Eq. (B.4)

$$\begin{aligned} P_x(\omega_3) &= 2\epsilon_o[d_{15}(E_x(\omega_1)E_z(\omega_2) + E_z(\omega_1)E_x(\omega_2))] \\ P_y(\omega_3) &= 2\epsilon_o[d_{24}(E_y(\omega_1)E_z(\omega_2) + E_z(\omega_1)E_y(\omega_2))] \\ P_z(\omega_3) &= 2\epsilon_o[d_{31}E_x(\omega_1)E_x\omega_2) + d_{32}E_y(\omega_1)E_y(\omega_2) + d_{33}E_z(\omega_1)E_z(\omega_2)]. \end{aligned} \tag{B.5}$$

B.2 Phase Matching and the Effective Nonlinear Constant

All nonlinear processes require both energy and momentum conservation. For three wave mixing (second order) processes, momentum conservation is equivalent to

$$\mathbf{k_3} = \mathbf{k_1} + \mathbf{k_2} \tag{B.6}$$

where the $\mathbf{k}$'s are the propagation vectors for the respective waves. The process of insuring this equality is referred to as *phase matching.* Since $k = (\omega/c)n$, phase matching essentially becomes a procedure of manipulating the refractive indices that the individual waves see such that Eq. (B.6) is satisfied.

One may take advantage of crystal birefringence to accomplish phase matching. In anisotropic materials, the ordinary and extraordinary polarizations see different refractive indices, where the extraordinay polarization is defined for the optical axis of the material. By orienting the propagation vector $\mathbf{k}$ of a wave at an angle θ_p with respect to the crystal axis, the index that the field sees can be manipulated.

KTP is well suited for Type-II 90° phase matching, as shown in Fig. 4.3, where we have assigned the crystal axis to the z-direction and the propagation direction arbitrarily to the y-axis ($\theta_p = 90°$). We then define a unitary transformation matrix $\overline{\overline{T}}$ that relates the space of the propagating fields to that of the crystal, as the crystal is rotated in the x-y plane an angle ϕ about its axis (z-direction)

$$\overline{\overline{T}} = \begin{bmatrix} \cos\phi & -\sin\phi & 0 \\ \sin\phi & \cos\phi & 0 \\ 0 & 0 & -1 \end{bmatrix}. \tag{B.7}$$

In Eq. (B.5), all fields are given in terms of the crystal reference frame. To compute the nonlinear polarization components, we must therefore transform the propagating

waves from the field frame to the crystal frame by applying $\overline{\overline{T}}$

$$\begin{bmatrix} E_x \\ E_y \\ E_z \end{bmatrix} = \overline{\overline{T}} \begin{bmatrix} E^o(\omega_1) \\ 0 \\ E^e(\omega_2) \end{bmatrix} \tag{B.8}$$

where $E^o(\omega_1)$ and $E^e(\omega_2)$ are the ordinary and extraordinary waves in the field frame, respectively. We then have for the fields in terms of the crystal frame

$$\begin{aligned} E_x &= \cos\phi E^o(\omega_1) \\ E_y &= \sin\phi E^o(\omega_1) \\ E_z &= -E^e(\omega_2) \end{aligned} \tag{B.9}$$

which, when substituted into Eq. (B.5) result in the crystal frame polarization components

$$\begin{aligned} P_x(\omega_3) &= -2\epsilon_o[d_{15}E^o(\omega_1)E^e(\omega_2)\cos\phi] \\ P_y(\omega_3) &= -2\epsilon_o[d_{24}E^o(\omega_1)E^e(\omega_2)\sin\phi] \\ P_z(\omega_3) &= 0. \end{aligned}$$

We are ultimately interested in the polarization components in the field reference frame, in particular, $P^o(\omega_3)$. These components can be obtained by applying the inverse of the transformation $\overline{\overline{T}}$ given by Eq. (B.7)

$$\begin{bmatrix} P^o(\omega_3) \\ 0 \\ P^e(\omega_3) \end{bmatrix} = \overline{\overline{T}}^{-1} \begin{bmatrix} P_x(\omega_3) \\ P_y(\omega_3) \\ P_z(\omega_3) \end{bmatrix}$$

which yeilds

$$\begin{aligned} P^o(\omega_3) &= P_x(\omega_3)\cos\phi + P_y(\omega_3)\sin\phi \\ &= -2\epsilon_o[d_{15}\cos^2\phi + d_{24}\sin^2\phi]E^o(\omega_1)E^e(\omega_2). \end{aligned}$$

If we then compare this to the general scalar form of the second order nonlinear polarization from Eq. (B.1), using Eq. (B.3)

$$P_{NL}^{(2)} = \epsilon_o\chi^{(2)}E(\omega_1)E(\omega_2) = 2\epsilon_o d_{eff}E(\omega_1)E(\omega_2)$$

we see that the effective nonlinear coefficient for KTP is given by

$$d_{eff} = -(d_{15}\cos^2\phi + d_{24}\sin^2\phi). \tag{B.10}$$

Appendix C

q-Parameter Simulation of OPO Resonator Structure

Sec. 2.5 addressed Gaussian beams in resonators and introduced the concept of q-parameter transformation of Gaussian beams by optical systems. Sec. 4.3 outlined the design of the OPO cavity which in part took into consideration mirror curvature and a target confocal parameter b for the resonator structure. The MATLAB program below was used to simulate the OPO cavity, taking as inputs the mirror curvatures, thickness and refractive index as well as the KTP crystal length and refractive index. It generated confocal parameters and beam waist locations as a function of cavity length. Additionally, the program generated *effective* confocal parameters and apparent waist locations for input and output mode matching, as explained in Appendix D.

```
%opo cavity

%ALL UNIT IN METERS

format short e

lambda_cav=1.064e-6;
lambda_pump=532e-9;

%cavity mirror radii
%input mirror
R1=200e-3;
%output mirror
R2=20e-3;

%average crystal index
n=1.79;
%crystal length
l=1e-2;

%cavity variable length
d=[0.0e-2:.02e-2:3.0e-2];

%mirror parameters for mode matching calculation
%mirror thickness
tm=4e-3;
%mirror index at 1.064um
nmc=1.4497;
%mirror index at 532nm
nmp=1.462;

%initialize variable arrays
cav_length=[zeros(size(d))];
radiusM1=[zeros(size(d))];
b=[zeros(size(d))];
w=[zeros(size(d))];
beff_in=[zeros(size(d))];
teff_in=[zeros(size(d))];
beff_out=[zeros(size(d))];
teff_out=[zeros(size(d))];

%matrix transforms of q parameter for cavity

        %mirror transform as lens M1
        F=[1 0;-2/R1 1];
        %mirror transform as lens M2
        H=[1 0;-2/R2 1];
        %propagation through crystal, n=1.79, l=1cm
        E=[1 l/n;0 1];

        %some additional matrix tranforms for mode matching calculation
        %spherical dielectric interface,input mirror
        J1=[1 0;((1/R1)*(1-(1/nmp))) 1/nmp];
        %spherical dielectric interface, output mirror
        J2=[1 0;((1/R2)*(1-(1/nmc))) 1/nmc];
        %travel through lens
        K=[1 tm;0 1];
        %interface from lens to air, input side
        L1=[1 0;0 nmp];
        %interface from lens to air, output side
```

```
        L2=[1 0;0 nmc];

%scan cavity lengths for stability
k=1;
for i=1:length(d)

        %free space in cavity (equal distance on either side of xtal)
        G=[1 (d(i)/2);0 1];

        %round trip matrix for cavity
        CAV=G*E*G*H*G*E*G*F;

        %matrix for determining pump (input) mode matching q
        %"effective" q just on outside planar surface of input mirror
        MM_in=L1*K*J1;

        %matrix for determining output mode matching
        MM_out=L2*K*J2*G*E*G*F;

        %extract elements of cavity ABCD matrix for transform
        A=CAV(1,1);
        B=CAV(1,2);
        C=CAV(2,1);
        D=CAV(2,2);

        %extract elements of input mode matching matrix
        AA1=MM_in(1,1);
        BB1=MM_in(1,2);
        CC1=MM_in(2,1);
        DD1=MM_in(2,2);

        %extract elements of output mode matching matrix
        AA2=MM_out(1,1);
        BB2=MM_out(1,2);
        CC2=MM_out(2,1);
        DD2=MM_out(2,2);

        %requirement for one round trip, q beginning= q round trip
        q1=((A-D)/(2*C))+(((((A+D)^2)-4)^.5)/(2*C));

        %in regions of stability, q will come in conjugate pairs

        %stability criterion

        if (((A+D)/2)^2)<1
                cav_length(k)=d(i)+.01;
                %add crystal length to total cavity length

                %extract free space confocal parameter in cavity
                b(k)=2*abs(imag(q1));
                %extract beam waist location from input mirror
                w(k)=real(q1);

                %calculate effective q outside cavity at input mirror
                qeff_in=((AA1*q1)+BB1)/((CC1*q1)+DD1);
                %extract effective confocal parameter for mode matching
                beff_in(k)=2*abs(imag(qeff_in));
                %extract effective waist location from outer planar
                %surface of input mirror
                teff_in(k)=real(qeff_in);
```

```
                %calculate effective q outside cavity at output mirror
                qeff_out=((AA2*q1)+BB2)/((CC2*q1)+DD2);
                %extract effective confocal parameter for mode matching
                beff_out(k)=2*abs(imag(qeff_out));
                %extract effective waist location from outer planar
                %surface of input mirror
                teff_out(k)=real(qeff_out);

                qM1=1/qeff_in;
                %extract beam size at outer planar surface of input mirror
                radiusM1(k)=sqrt(1/((abs(imag(qM1)))*pi/lambda_pump));
                qM2=1/qeff_out;
                %extract beam size at outer planar surface of output mirror
                radiusM2(k)=sqrt(1/((abs(imag(qM1)))*pi/lambda_cav));
                k=k+1;
        end

end

v=[0 3 0 4];
axis(v);
plot(cav_length*100,b*100*n)
title('Confocal Parameter b vs. cavity length')
xlabel('total cavity length, cm')
ylabel('b, cm')
grid
text(.15,.41,'M1(input):R=20cm, M2(ouput):R=2.5cm','sc')
text(.15,.4,'KTP xtal, 1cm long centered in cavity')
meta opocav.met

v=[0 3 0 .1];
axis(v);
plot(cav_length*100,w*100)
title('Beam waist location from inside of M1 vs. cavity length')
grid
ylabel('waist location, cm')
xlabel('cavity length, cm')
meta

v=[0 3 0 3];
axis(v);
plot(cav_length*100, beff_in*100)
title('Effective Confocal Parameter for pump mode matching vs. cavity length')
grid
xlabel('cavity length, cm')
ylabel('b effective, cm')
meta

v=[0 3 0 .5];
axis(v);
plot(cav_length*100, teff_in*100)
title('Effective waist location from outer surface of input mirror')
grid
xlabel('cavity length, cm')
ylabel('t effective, cm')
meta

v=[0 3 0 2];
axis(v);
```

```
plot(cav_length*100, beff_out*100)
title('Effective Confocal Parameter for output mode matching vs. cavity length')
grid
xlabel('cavity length, cm')
ylabel('b effective, cm')
meta

v=[0 3 0 3];
axis(v);
plot(cav_length*100, teff_out*100)
title('Effective waist location from outer surface of output mirror')
grid
xlabel('cavity length, cm')
ylabel('t effective, cm')
meta
```

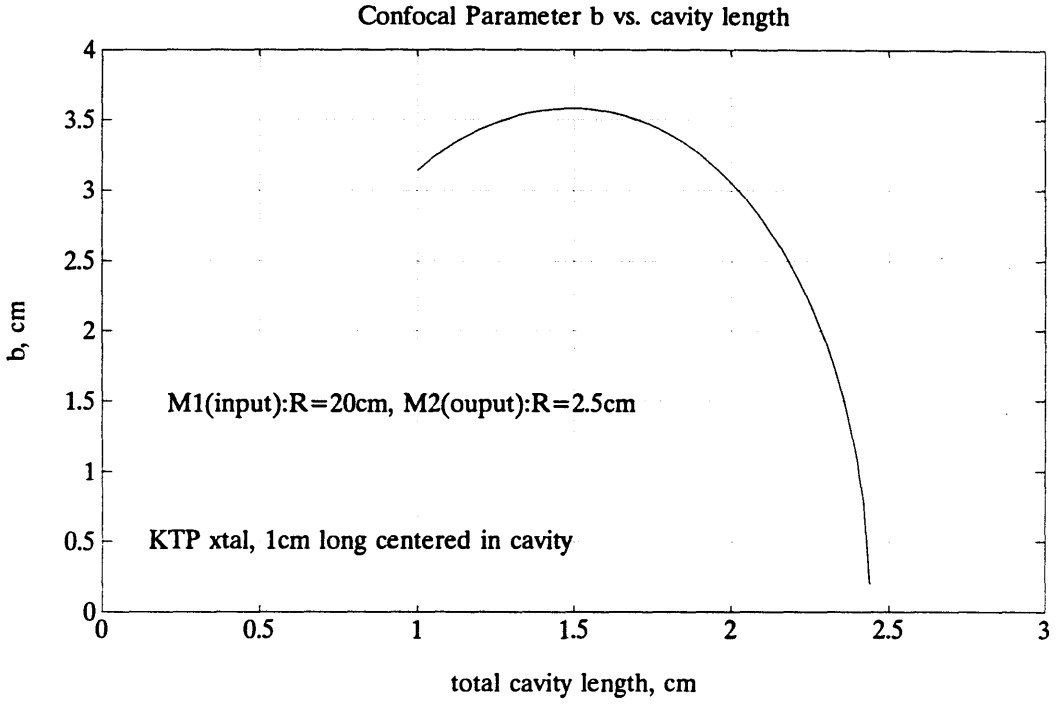
Confocal Parameter b vs. cavity length
b, cm
M1(input):R=20cm, M2(ouput):R=2.5cm
KTP xtal, 1cm long centered in cavity
total cavity length, cm
0
0.5
1
1.5
2
2.5
3
3.5
4

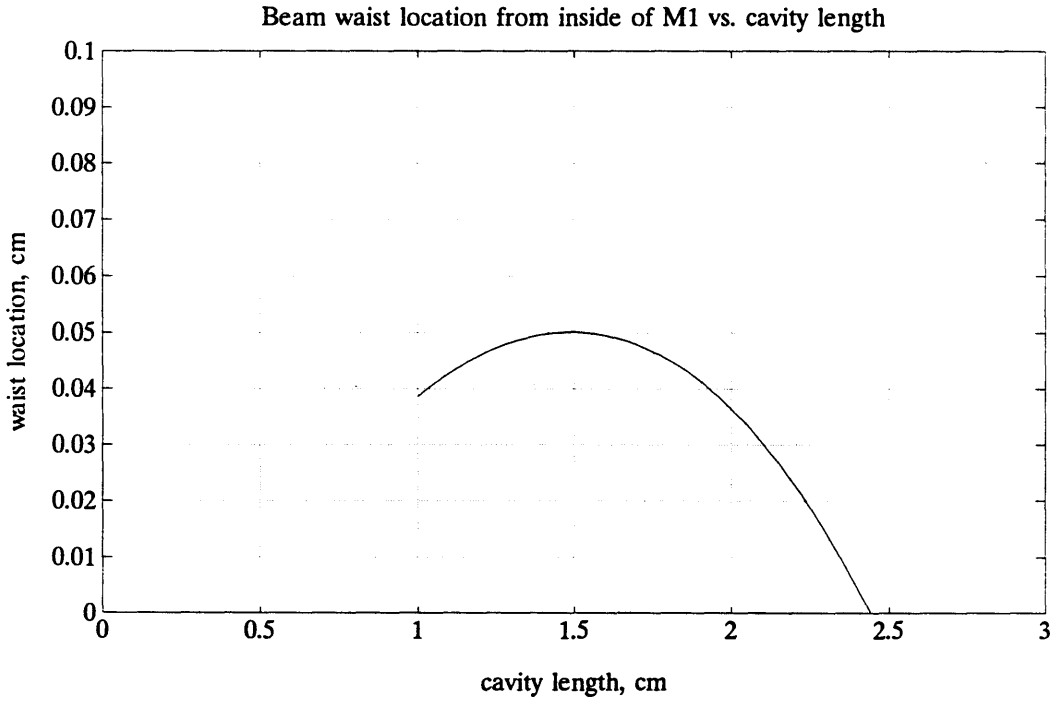
Beam waist location from inside of M1 vs. cavity length
waist location, cm
cavity length, cm
0
0.01
0.02
0.03
0.04
0.05
0.06
0.07
0.08
0.09
0.1
0.5
1
1.5
2
2.5
3

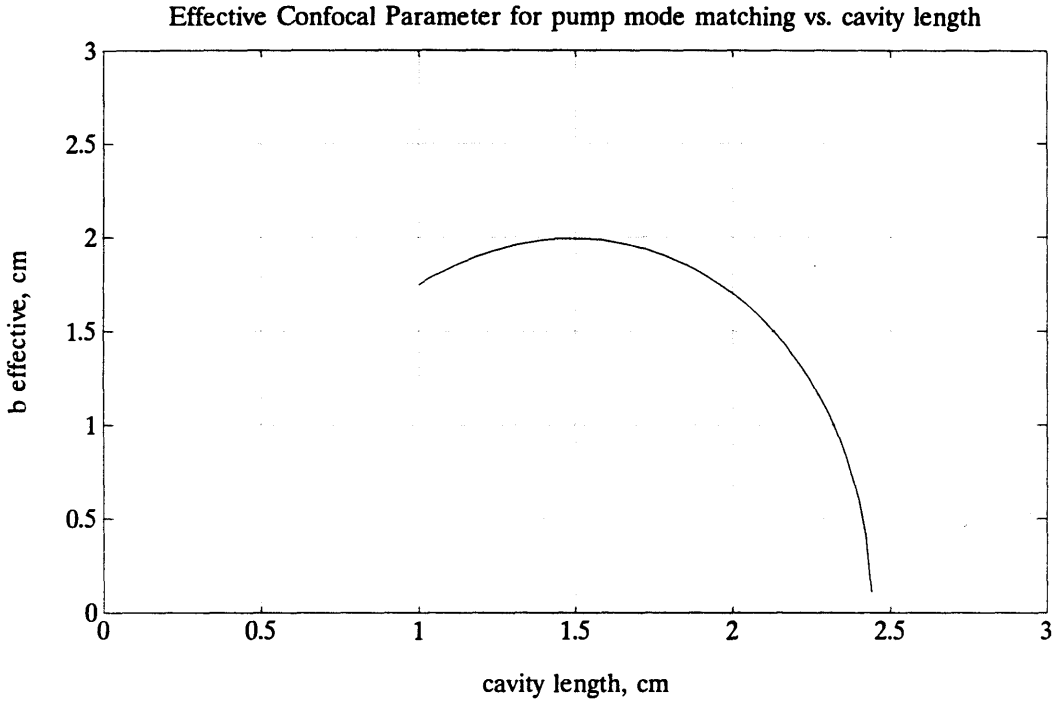
Effective Confocal Parameter for pump mode matching vs. cavity length
b effective, cm
cavity length, cm
0
0.5
1
1.5
2
2.5
3

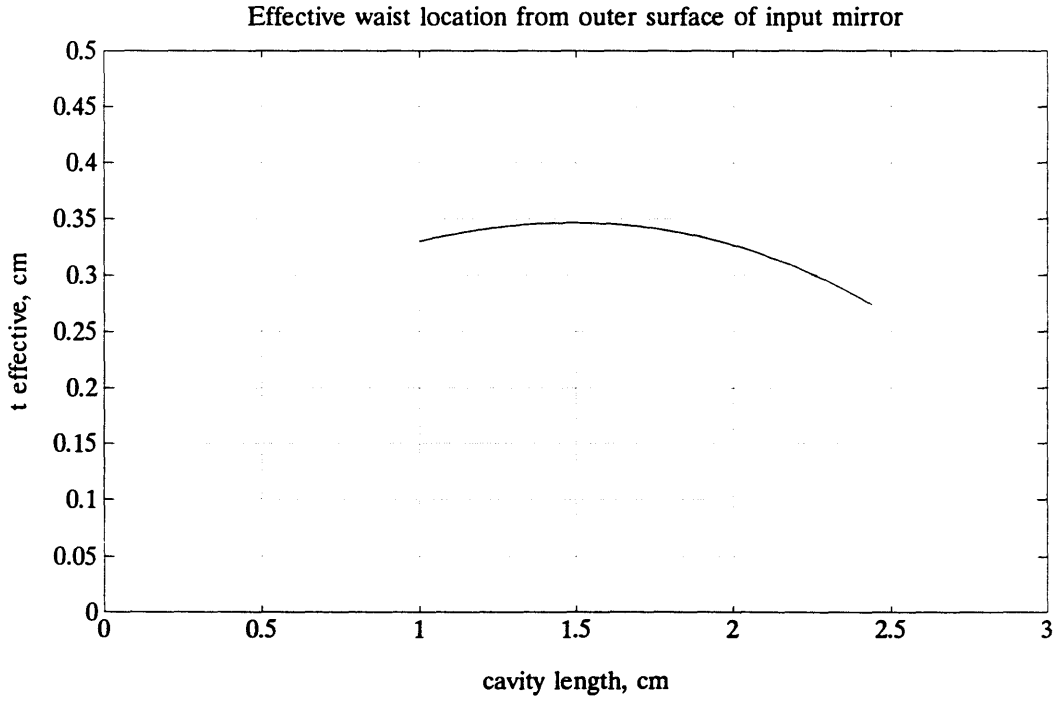
Effective waist location from outer surface of input mirror
t effective, cm
cavity length, cm
0
0.05
0.1
0.15
0.2
0.25
0.3
0.35
0.4
0.45
0.5
0.5
1
1.5
2
2.5
3

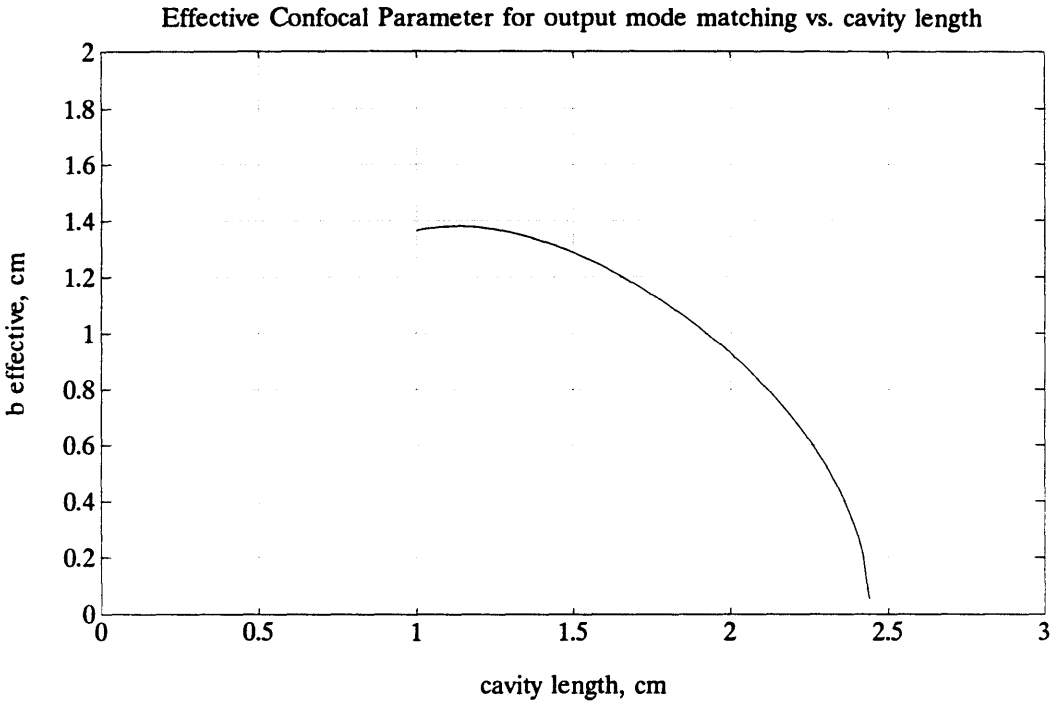
Effective Confocal Parameter for output mode matching vs. cavity length
b effective, cm
cavity length, cm
0
0.2
0.4
0.6
0.8
1
1.2
1.4
1.6
1.8
2
0.5
1.5
2.5
3

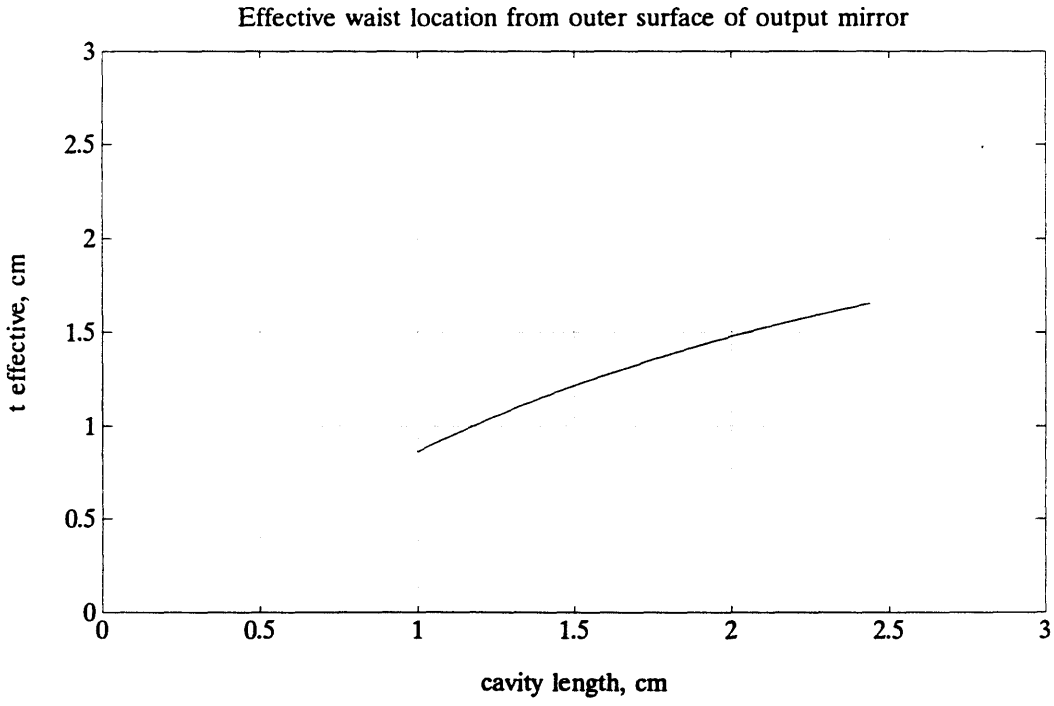
Effective waist location from outer surface of output mirror
t effective, cm
cavity length, cm
0
0.5
1
1.5
2
2.5
3

Appendix D

Mode Matching for Gaussian Beams

It was discussed in Sec. 2.5 that the modes of resonators can be characterized by Gaussian beams with certain properties and parameters which are defined by the resonator geometry. These beams are often injected into other optical structures with different sets of beam parameters. These optical structures can assume various physical forms, such as laser cavities and crystals of nonlinear dielectric material used in parametric optics; for example, in this experiment we had a pump laser source injected into an OPO.

To match the modes of one structure to those of another one must transform a given Gaussian beam into another beam with prescribed properties. This transformation is usually accomplished with a thin lens, but other more complex optical systems can be used. This discussion is devoted to the simple case of mode matching with a thin lens [1].

The location of the waists of the two beams to be transformed into each other and the beam diameters (and hence confocal parameters) at the waist are usually known or can be computed. To match the beams, a lens of a focal length f is chosen that is larger than a characteristic length f_o defined by the two beams. The distances between the lens and the two beam waists is then adjusted according to the formulas below.

[1] The material in this section comes in large part from reference [18].

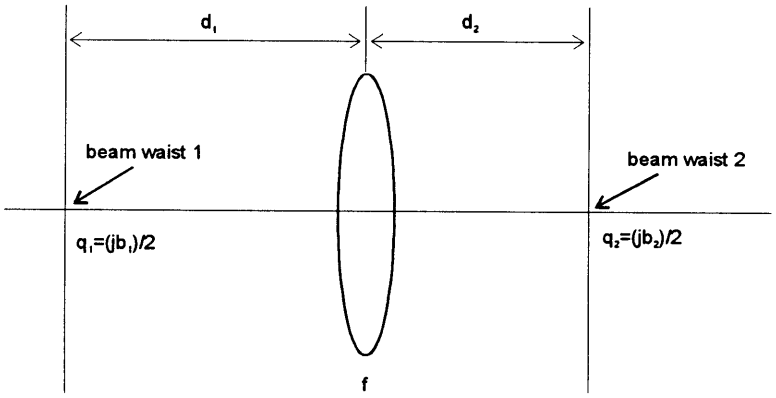

Figure D.1: A Gaussian beam transformed by a thin lens.

In Fig. D.1 the two beam waists are assumed to be located at distances d_1 and d_2 from the lens. The confocal parameters b_1 and b_2 are defined by the waist radii w of the two systems to be matched by

$$\begin{aligned} b_1 &= \frac{2\pi w_1^2}{\lambda} \\ b_2 &= \frac{2\pi w_2^2}{\lambda}. \end{aligned} \tag{D.1}$$

Using these parameters, the characteristic length $f_\circ$ is defined as

$$f_\circ^2 = \frac{1}{4} b_1 b_2. \tag{D.2}$$

Any lens with a focal length $f > f_\circ$ can be used to perform the matching transformation. Once f is chosen, the distances d_1 and d_2 have to be adjusted to satisfy the matching formulas

$$\begin{aligned} d_1 &= f \pm \frac{1}{2} b_1 \sqrt{(f^2/f_\circ^2) - 1} \\ d_2 &= f \pm \frac{1}{2} b_2 \sqrt{(f^2/f_\circ^2) - 1}. \end{aligned} \tag{D.3}$$

In Eq. (D.3), one can choose either both plus signs or both minus signs for matching.

The two important parameters of beams that emerge from various optical structures are the effective confocal parameter b_{eff} and the distance t_{eff} which gives the effective waist location inside the resonator of the emerging beam. These values may be significantly different than the actual confocal parameter and waist location for the resonator as a result of cavity end-mirrors of substantial thickness, which act as negative lenses and change the characteristics of the emerging beam. Reference [18] contains a table of formulas for these effective parameters for various common optical structures. Throughout this thesis, these effective parameters are quoted for all of the resonator structures used in the experiment, and were determined by MATLAB calculations using q-parameter transformations, using the methodology developed in [14, Sec. 5.4].

Appendix E

Effective Area of a Gaussian Beam

The radial variation in the transverse electric field of a Gaussian beam in the near field of the fundamental mode is given by

$$E(r) = E_\circ e^{-r^2/w_\circ^2}. \tag{E.1}$$

Intensity is defined by Eq. (2.14). The power generated by the Gaussian beam can be calculated using Eq. (2.14) by evaluating the integral

$$\begin{aligned} P &= \frac{nc\epsilon_\circ}{2}\int |E(r)|^2 r dr d\phi \\ &= \frac{nc\epsilon_\circ}{2}\int_0^{2\pi}\int_0^{\infty} |E_\circ|^2 r e^{-2r^2/w_\circ^2} dr d\phi \\ &= \frac{nc\epsilon_\circ}{2}|E_\circ|^2 \int_0^{2\pi} \frac{w_\circ^2}{4} d\phi \\ &= I_\circ\left(\frac{\pi w_\circ^2}{2}\right). \end{aligned} \tag{E.2}$$

Therefore, the effective area of the Gaussian beam is

$$A = \frac{\pi\omega_\circ^2}{2}. \tag{E.3}$$

Appendix F

Theoretical Model for Intensity Correlation Spectrum

A Mathcad [1] program is presented which uses the treatment of [39] as presented in Ch. 2 for generating the theoretical correlation spectrum from the system parameters. The program takes as variables the cavity losses for the s and p-polarized OPO output beams (Table 4.2), the cavity loss for the pump (from measured finesse, Table 4.4), the OPO output coupler transmission, the cavity free spectral range (Table 4.3), the oscillation threshold, the pumping power, the detection efficiency (Table 5.2) and the excess pump noise spectrum (Fig. 3.15).

The program generates three correlation spectra. The first averages the losses of the two polarizations to simulate the simplified correlation spectra given by Eq. (4.2) from Heidman, *et. al.* [15]. The second includes the effects of unbalanced losses using a shot noise limited pump source. Finally, the third includes both the effects of unbalanced losses and excess pump noise.

[1] Mathcad is a registered trademark of MathSoft, Inc., Cambridge, MA.

Intensity Difference (Correlation) Spectrum

In the presence of pump noise with unbalanced signal and idler

USER VARIABLES:

$\alpha_1 = .03343$ total cavity loss for extraordinary beam (s)

$\alpha_2 = .03143$ total cavity loss for ordinary beam (p)

$\alpha_p = .114$ total cavity loss for pump

$\gamma = .026857$ output coupler transmission

$FSR = 5.58 \cdot 10^9$ cavity free spectral range in Hz

$P_{th} = .06$ OPO pumping threshold in watts

$P_p = .08$ Pump power in watts

$\eta = .89498$ total detection efficiency, from OPO output to detectors (includes all optical losses in beam path, signal and idler paths averaged)

$i = 1..34$

excess pump noise spectrum: (enter frequency in MHZ)

f_{MHz_i} =	h_i =
.1	7300
.2	26631
.325	61193
.4	61724
.453	3941775
.480	38417
.5	20752
.6	9947
.7	13128
.8	3044
.9	1329
1	837
1.2	525
1.4	478
1.6	360
1.8	210
2	151.4
2.2	96.7
2.4	69.7
2.6	43.8
2.8	33.3
3.0	26
3.2	23
3.4	19.9
3.6	17.3
3.8	12.5
4	12.5
4.2	10.9
4.4	8.7
4.6	5.9
4.8	4.6
5	2.4
5.2	1.1
5.4	1

$f_i = f_{MHz_i} \cdot 10^6$

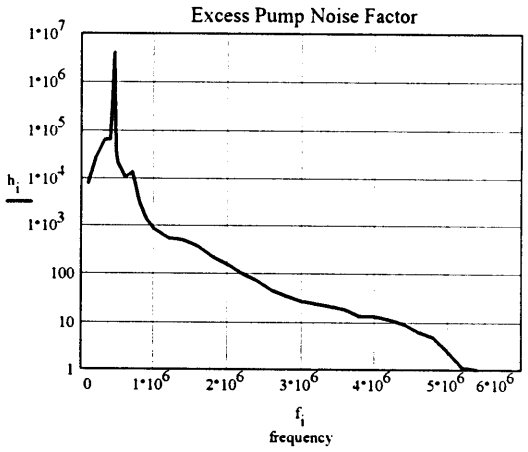

PROGRAM VARIABLES:

$\kappa = \frac{(\alpha_1 + \alpha_2)\cdot FSR}{2\cdot\pi}$ sum of loss rates for extraordinary and ordinary beams (in Hz)

$\delta = \frac{(\alpha_1 - \alpha_2)\cdot FSR}{2\cdot\pi}$ difference of loss rates

$\kappa_p = \frac{\alpha_p \cdot FSR}{2\cdot\pi}$ pump loss rate

$\varepsilon = \sqrt{\frac{P_p}{P_{th}}} - 1$ percent of pump field strength above threshold

$\Gamma = \frac{1}{2}\cdot\left(\frac{\gamma}{\alpha_1} + \frac{\gamma}{\alpha_2}\right)$

$g = \frac{\frac{1}{2}\cdot\left(\frac{\gamma}{\alpha_1} - \frac{\gamma}{\alpha_2}\right)}{\Gamma}$ extraordinary-ordinary beam loss mismatch

$$D_i = (\kappa^2 - \delta^2)\cdot\kappa_p\cdot\varepsilon - (f_i)^2\cdot(\kappa_p + \kappa) - f_i\cdot\left[\kappa\cdot\kappa_p\cdot(\varepsilon + 1) - (f_i)^2\right]\cdot j$$

$$Z1_i = (\kappa - \delta)\cdot\left[\frac{1}{\kappa - f_i\cdot j} - \frac{\kappa - f_i\cdot j - \delta}{D_i}\cdot\left[\frac{\delta\cdot\kappa_p\cdot\varepsilon}{\kappa - f_i\cdot j} - g\cdot(\kappa_p - f_i\cdot j)\right]\right]$$

$$Z2_i = (\kappa - \delta)\cdot\left[\frac{1}{\kappa - f_i\cdot j} + \frac{\kappa - f_i\cdot j + \delta}{D_i}\cdot\left[\frac{\delta\cdot\kappa_p\cdot\varepsilon}{\kappa - f_i\cdot j} - g\cdot(\kappa_p - f_i\cdot j)\right]\right]$$

CORRELATION SPECTRA (Normalized to Shot Noise):

Balanced signal and idler (average losses):

$$S_{bal_i} = \frac{(f_i)^2 + \kappa^2\cdot\left(1 - \frac{2\cdot\gamma}{\alpha_1 + \alpha_2}\right)}{(\kappa)^2 + (f_i)^2}$$

Unbalanced signal and idler, shot noise limited pump:

$$S_{ub_i} = \left[1 + \frac{1}{2}\cdot\Gamma\cdot\left[(|Z1_i|)^2 + (|Z2_i|)^2\right] - \left(\frac{\gamma}{\alpha_1}\cdot Re(Z1_i) + \frac{\gamma}{\alpha_2}\cdot Re(Z2_i)\right)\right] + \frac{2\cdot\Gamma\cdot\kappa_p^{\,2}\cdot\varepsilon}{(|D|)^2}\cdot\left[g^2\cdot(\kappa^2 - \delta^2)^2 + (f_i)^2\cdot(g\cdot\kappa + \delta)^2\right]$$

Unbalanced signal and idler, excess pump noise:

$$S_{pn_i} = \left[1 + \frac{1}{2}\cdot\Gamma\cdot\left[(|Z1_i|)^2 + (|Z2_i|)^2\right] - \left(\frac{\gamma}{\alpha_1}\cdot Re(Z1_i) + \frac{\gamma}{\alpha_2}\cdot Re(Z2_i)\right)\right] + \frac{2\cdot\Gamma\cdot\kappa_p^{\,2}\cdot\varepsilon}{(|D|)^2}\cdot\left[g^2\cdot(\kappa^2 - \delta^2)^2 + (f_i)^2\cdot(g\cdot\kappa + \delta)^2\right]\cdot h_i$$

CORRELATION SPECTRA, (cont.)

Considering external detection efficiency, power spectra in dBm:

$SD_{bal_i} = 10 \cdot \log\left[\eta \cdot S_{bal_i} + (1 - \eta)\right]$ Balanced signal and idler (average losses)

$SD_{ub_i} = 10 \cdot \log\left[\eta \cdot S_{ub_i} + (1 - \eta)\right]$ Unbalanced signal and idler, shot noise limited pump

$SD_{pn_i} = 10 \cdot \log\left[\eta \cdot S_{pn_i} + (1 - \eta)\right]$ Unbalanced signal and idler, excess pump noise

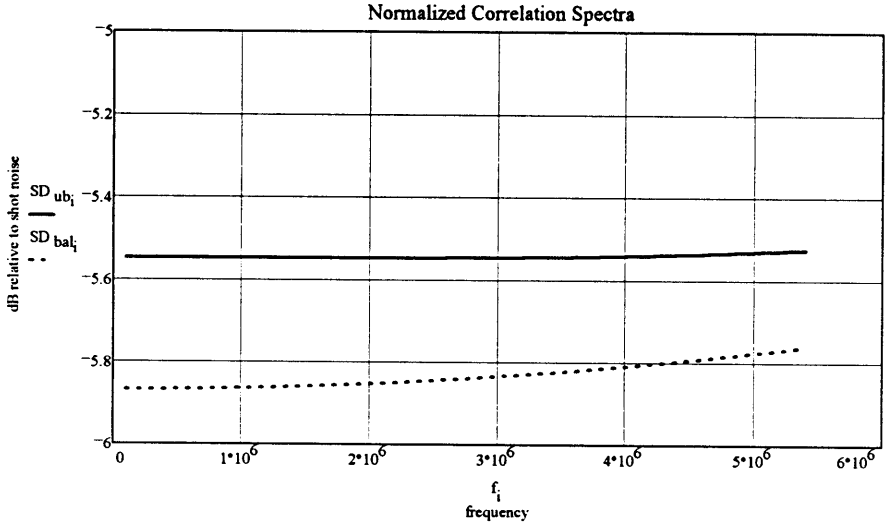

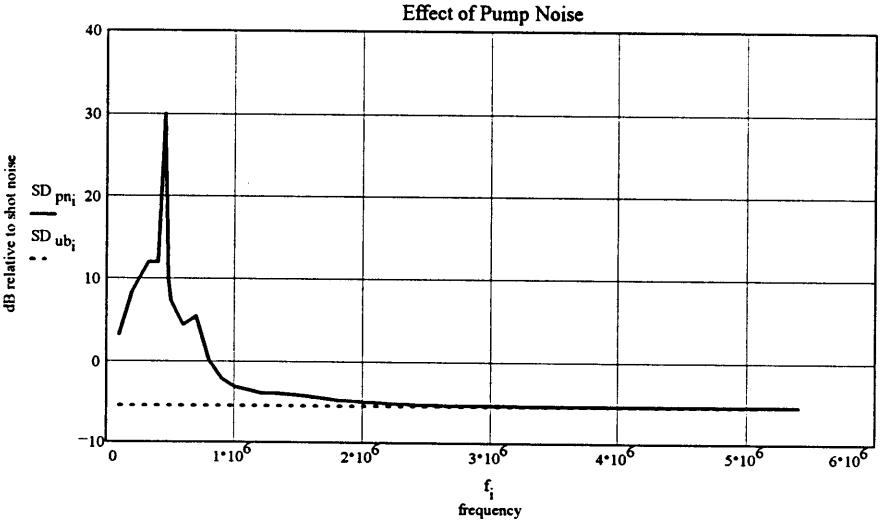

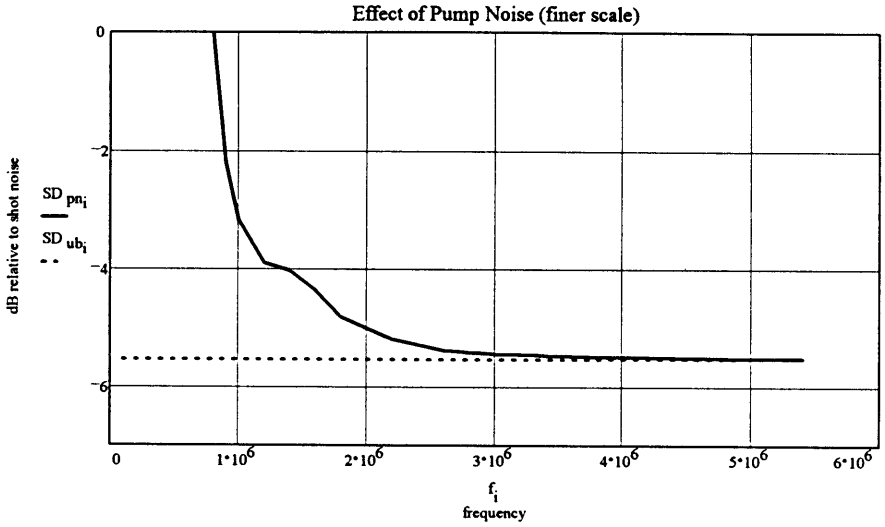
Effect of Pump Noise (finer scale)
0
−2
−4
−6
dB relative to shot noise
SD pn_i
SD ub_i
0
1·10^6
2·10^6
3·10^6
4·10^6
5·10^6
6·10^6
f_i
frequency

Intensity Difference (Correlation) Spectrum

In the presence of pump noise with unbalanced signal and idler

USER VARIABLES:

Simulation with lower cavity losses, higher pump power and higher detection efficiency

$\alpha_1 = .03$ total cavity loss for extraordinary beam (s)

$\alpha_2 = .029$ total cavity loss for ordinary beam (p)

$\alpha_p = .114$ total cavity loss for pump

$\gamma = .026857$ output coupler transmission

$FSR = 5.58 \cdot 10^9$ cavity free spectral range in Hz

$P_{th} = .06$ OPO pumping threshold in watts

$P_p = .12$ Pump power in watts

$\eta = .95$ total detection efficiency, from OPO output to detectors (includes all optical losses in beam path, signal and idler paths averaged)

$i = 1..34$

excess pump noise spectrum:
(enter frequency in MHZ)

f_{MHz_i} =	h_i =
.1	7300
.2	26631
.325	61193
.4	61724
.453	3941775
.480	38417
.5	20752
.6	9947
.7	13128
.8	3044
.9	1329
1	837
1.2	525
1.4	478
1.6	360
1.8	210
2	151.4
2.2	96.7
2.4	69.7
2.6	43.8
2.8	33.3
3.0	26
3.2	23
3.4	19.9
3.6	17.3
3.8	12.5
4	12.5
4.2	10.9
4.4	8.7
4.6	5.9
4.8	4.6
5	2.4
5.2	1.1
5.4	1

$f_i = f_{MHz_i} \cdot 10^6$

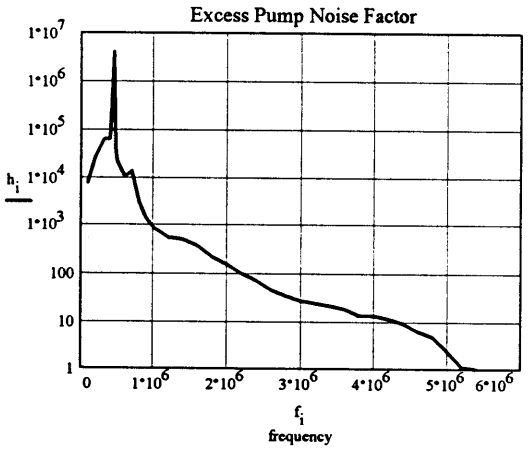

CORRELATION SPECTRA, (cont.)

Considering external detection efficiency, power spectra in dBm:

$SD_{bal_i} = 10 \cdot \log\left[\eta \cdot S_{bal_i} + (1 - \eta)\right]$ Balanced signal and idler (average losses)

$SD_{ub_i} = 10 \cdot \log\left[\eta \cdot S_{ub_i} + (1 - \eta)\right]$ Unbalanced signal and idler, shot noise limited pump

$SD_{pn_i} = 10 \cdot \log\left[\eta \cdot S_{pn_i} + (1 - \eta)\right]$ Unbalanced signal and idler, excess pump noise

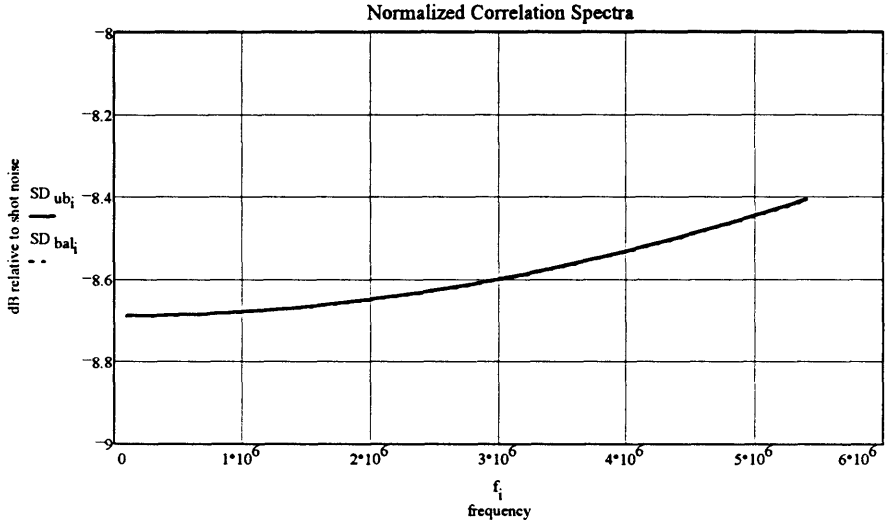

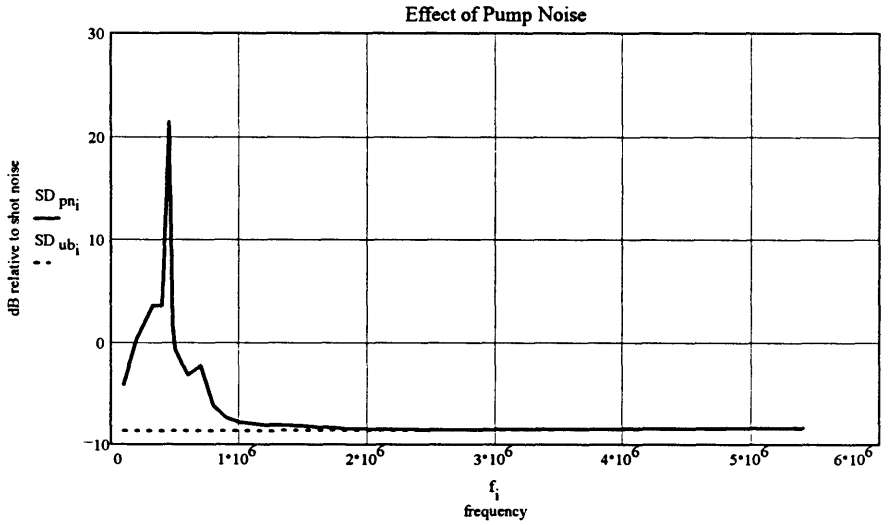

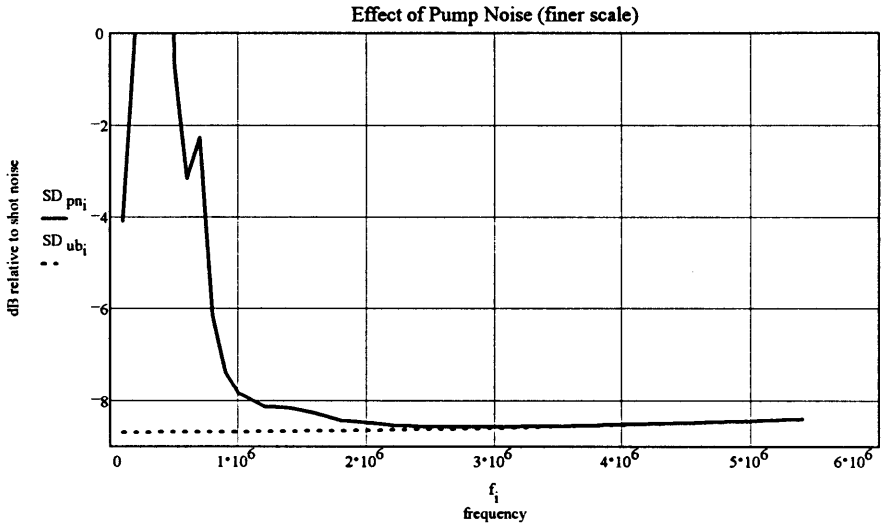
Effect of Pump Noise (finer scale)
0
-2
-4
-6
-8
dB relative to shot noise
SD pn_i
SD ub_i
0
1·10^6
2·10^6
3·10^6
4·10^6
5·10^6
6·10^6
f_i
frequency

References

[1] *Litton-Airtron, verbal communication with Tom Irady.*

[2] *Journal of the Optical Society of America B*, 4(10), October 1987. Special issue on Squeezed States of the Electromagnetic Field.

[3] I. Abram, R.K. Raj, J.L. Oudar, and G. Dolique. Direct observation of the second-order coherence of parametrically generated light. *Physical Review Letters*, 57(20):2516, November 1986.

[4] J.E. Bjorkholm. *IEEE Journal of Quantum Electronics*, 5:293, 1969.

[5] J.E. Bjorkholm, A. Ashkin, and R.G. Smith. Improvement of optical parametric oscillators by nonresonant pump reflection. *IEEE Journal of Quantum Electronics*, QE-6:797, December 1970.

[6] G.D. Boyd and D.A. Kleinmann. Parametric interaction of focussed gaussian beams. *Journal of Applied Physics*, 39:3597, 1968.

[7] D. Burnham and D. Weinberg. Observation of simultaneity in parametric production of optical photon pairs. *Physical Review Letters*, 25(2):84, 1970.

[8] P.N. Butcher and D. Cotter. *The Elements of Nonlinear Optics.* Cambridge University Press, first edition, 1991.

[9] R.W.P. Drever, J.L. Hall, F.V. Kowalski, J. Hough, G.M. Ford, A.J. Munley, and H. Ward. Laser phase and frequency stabilization using an optical resonator. *Applied Physics B*, 31:97, 1983.

[10] C. Fabre, E. Giacobino, A. Heidman, and S. Reynaud. Noise characteristics of a non-degenerate optical parametric oscillator-application to quantum noise reduction. *Journal of Physics, France*, 50:1209, 1989.

[11] G.F. Franklin, J.D. Powell, and A. Emami-Naeini. *Feedback Contol of Dynamic Systems.* Addison-Wesley, third edition, 1994.

[12] R. Graham. The quantum fluctuations of the optical parametric oscillator II. *Z. Physik*, 210:319, 1968.

[13] J.L. Hall. Stabilizing lasers for applications in quantum optics. In J. Harvey and D.F. Walls, editors, *Internation Conference on Quantum Optics.* Springer-Verlag, Heidelberg, feb 1986.

[14] Hermann A. Haus. *Waves and Fields in Optoelectronics.* Prentice-Hall, 1984.

[15] A. Heidman, R.J. Horowicz, S. Reynaud, E. Giacobino, and C. Fabre. Observation of quantum noise reduction on twin laser beams. *Physical Review Letters*, 59(22):2555, November 1987.

[16] P. Horowitz and W. Hill. *The Art of Electronics.* Cambridge University Press, second edition, 1989.

[17] E. Ippen. Nonlinear optics. Lecture notes for Massachusetts Institute of Technology course 6.634, 1996.

[18] H. Kogelnik and T. Li. Laser beams and resonators. *Applied Optics*, 5(10):1550, October 1966.

[19] Bobby Yoke Fung Lai. A tunable light source at 1.6μm by difference-frequency mixing in cesium titanyl arsenate. Master's thesis, Massachusetts Institute of Technology, Department of Electrical Engineering and Computer Science, January 1995.

[20] A.S. Lane, M.D. Reid, and D.F. Walls. *Physical Review Letters*, 60:1940, 1988.

[21] Dicky Lee. *Optical Parametric Oscillators and Precision Optical Frequency Measurements.* PhD dissertation, Massachusetts Institute of Technology, Department of Physics, February 1996.

[22] Alberto Leon-Garcia. *Probability and Random Processes for Electrical Engineering.* Addison-Wesley, first edition, 1989.

[23] K.W. Leong. *Intensity Quantum Noise Reduction with an Above-Threshold Optical Parametric Oscillator.* PhD dissertation, Massachusetts Institute of Technology, Department of Electrical Engineering and Computer Science, February 1991.

[24] K.W. Leong, N.C. Wong, and J.H. Shapiro. Nonclassical intensity correlation from a type-I phase-matched optical parametric oscillator. *Optics Letters*, 15(19):1058, October 1990.

[25] Rodney Loudon. *The Quantum Theory of Light.* Clarendon Press, Oxford, second edition, 1985.

[26] J. Mertz, T. Debuisschert, A. Heidman, C. Fabre, and E. Giacobino. Improvements in the observed intensity correlation of optical parametric oscillator twin beams. *Optics Letters*, 16(16):1234, August 1991.

[27] Steven G. Patterson. Quantum intensity noise correlation in a type-II phase matched optical parametric oscillator. Master's thesis, Massachusetts Institute of Technology, Department of Electrical Engineering and Computer Science, June 1995.

[28] J.G. Rarity, P.R. Tapster, J.A. Levenson, J.C. Garreau, I. Abram, J. Mertz, T. Debuisschert, A. Heidman, C. Fabre, and E. Giacobino. Quantum correlated twin beams. *Applied Physics*, B55:250, 1992.

[29] B. Saleh and M. Teich. Can the channel capacity of a light wave communication system be increased by the use of photon-number squeezed light. *Physical Review Letters*, 58(25):2656, June 1987.

[30] R.M. Shelby, M.D. Levenson, S.H. Perlmutter, R.G. DeVoe, and D.F. Walls. Broadband parametric deamplification of quantum noise in an optical fiber. *Physical Review Letters*, 57:691, 1986.

[31] R.E. Slusher, L.W. Holberg, B. Yurke, J.C. Mertz, and J.E. Valley. Observation of squeezed states generated by four-wave mixing in an optical cavity. *Physical Review Letters*, 55(22):2409, November 1985.

[32] Richart E. Slusher and Bernard Yurke. Squeezed light. *Scientific American*, page 50, May 1988.

[33] J. Snyder, E. Giacobino, C. Fabre, A. Heidman, and M. Ducloy. Sub-shot-noise measurements using the beat note between quantum correlated photon beams. *Journal of the Optical Society of America, B*, 7(10):2132, October 1990.

[34] Ferrel G. Stremler. *Introduction to Communication Systems.* Addison-Wesley, third edition, 1992.

[35] Malvin C. Teich and Bahaa E.A. Saleh. Squeezed and anti-bunched light. *Physics Today*, page 20, June 1990.

[36] J. Wilson and J.F.B. Hawkes. *Optoelectronics, An Introduction.* Prentice Hall, second edition, 1989.

[37] N.C. Wong. Squeezed amplification in a nondegenerate parametric amplifier. *Optics Letters*, 16(21):1698, November 1991.

[38] N.C. Wong, K.W. Leong, and J.H. Shapiro. Quantum correlation and absorption spectroscopy in an optical parametric oscillator in the presence of pump noise. *Optics Letters*, 15(16):891, August 1990.

[39] L.A. Wu, H.J. Kimble, J.L. Hall, and H. Wu. Generation of squeezed states by parametric down conversion. *Physical Review Letters*, 57(20):2520, November 1986.

[40] A. Yariv. *Optical Electronics.* Holt, Rinehart and Winston, fourth edition, 1991.

[41] Amnon Yariv. *Quantum Electronics.* John Wiley and Sons, third edition, 1989.